Kicking at the Darkness: Detecting Deeply Embedded Protostars at 1–10 μm

by

Aaron J. Maxwell
B.Sc., York University, 2007

A Thesis Submitted in Partial Fulfillment of the
Requirements for the Degree of

MASTER OF SCIENCE

in the Department of Physics & Astronomy

Kicking at the Darkness: Detecting Deeply Embedded Protostars at 1–10 μm

by

Aaron J. Maxwell
B.Sc., York University, 2007

Supervisory Committee

Dr. D. Johnstone, Supervisor
(National Research Council Herzberg Institute of Astrophysics)

Dr. J. Willis, Departmental Member
(Department of Physics & Astronomy, University of Victoria)

Supervisory Committee

Dr. D. Johnstone, Supervisor
(National Research Council Herzberg Institute of Astrophysics)

Dr. J. Willis, Departmental Member
(Department of Physics & Astronomy, University of Victoria)

ABSTRACT

We present an analysis of observations using the Spitzer Space Telescope and the James Clerk Maxwell Telescope of deeply embedded protostars in the Perseus Giant Molecular Cloud. Building on the results of Jørgensen et al. (2007), we attempt to characterize the physical properties of these deeply embedded protostars, discovered due to their extremely red near infrared colours and their proximity to protostellar cores detected at 850 μm. Using a grid of radiative transfer models by Robitaille et al. (2006), we fit the observed fluxes of each source, and build statistical descriptions of the best fits. We also use simple one dimensional analytic approximations to the protostars in order to determine the physical size and mass of the protostellar envelope, and use these 1D models to provide a goodness-of-fit criterion when considering the model grid fits to the Perseus sources. We find that it is possible to create red [3.6]-[4.5] and [8.0]-[24] colours by inflating the inner envelope radius, as well as by observing embedded protostars through the bipolar outflows. The majority of the deeply embedded protostars, however, are well fit by models seen at intermediate inclinations, with outflow cavity opening angles $\lesssim 30^{\circ}$, and scattering of photons off of the cavity walls produces the red colours. We also discuss other results of the SED fitting.

Contents

List of Tables

List of Figures

ACKNOWLEDGEMENTS

First of all, I would like to thank my supervisor, Dr. Doug Johnstone, for being a pillar of support during this thesis. He always was open to new ideas, and was quite understanding every time I fell flat on my face from an idea that would not work. I doubt many would have been as keen as he was in supporting a student to pursue a change in fields, and for that I am grateful. He made every new code, every new discovery, as fun and interesting as the one before it. Without him, I doubt this project would be what it is today.

I would also like to thank Jes Jørgensen and Thomas Robitaille. When I needed the c2d data for Perseus, Jes answered my questions and was kind enough to give me the Perseus c2d data, when he could have easily e-mailed me the *man* pages for searching the VIZIER catalog. Thomas was willing to let a shy MSc student come down to Boston to bug him about his radiative transfer grid, and ran the c2d and SCUBA data through his automatic fitting routine numerous times. The conversations we had resulted in significant improvements to portions of this thesis.

I can't forget all the new friends and family I made out here, who made life in Victoria these past two years all that it could be, and more. Whether we were laughing, crying, or playing Mario Kart till four in the morning, you kept me sane. Andy, thanks for being my friend, confidante, and homework partner. It was nice to meet someone who was as nerdy as me. Sarah, thanks for being a good friend and reminding me of home. Lisa and Rob, thank you for everything, especially for getting me accustomed to dogs bigger than my foot. To my family and friends in Toronto, thank you for being who you are. You were the strength that kept me going in the darkest times, so that I could make it back home.

Rachel, you believed in me when I did not believe in myself. You inspired me to take the chance to fulfill a childhood dream, even if it meant we had to put distance between us. You never tried to keep me from doing the thing that I love most, and gave me the will to succeed. I promise to spend the rest of my life thanking you for that gift, and to make your day every day. Oh, and to give you a life of ice cream.

Nothing worth having comes without some kind of fight;
you gotta kick at the darkness till it bleeds daylight.
Bruce Cockburn

I am, and always shall be, your friend.
Spock

DEDICATION

To my parents.
I think it's safe to say I know more than you now ...

Chapter 1

Introduction

The problem of forming stars is more complicated than one might naively believe. Far from the idyllic view of a cloud of dust and gas collapsing under gravity, it is instead complicated by magnetic fields (e.g. Mouschovias and Spitzer 1976), turbulence (e.g. Larson 1981), and outflows (e.g. Dopita et al. 1982). Although simple models can be applied to relatively small and low mass dark clouds where single stars may form (e.g. Alves et al. 2001), the models must increase in complexity in order to describe the birth sites of the vast majority of stars, as they form in clusters (e.g. Lada and Lada 2003). Complicating the matter is the fact that the significant amount of dust surrounding the stars absorbs much of the emission from the stellar embryos, essentially plunging the cloud into darkness. Only longer wavelength observations in the infrared, millimetre, and radio can penetrate the darkness and reveal the light of these burgeoning precursors to stars.

Most stars are born within massive (10^3–10^5 $M_\odot$), large (10–100 pc), cold (10–20 K) conglomerates of dust and gas. Within the ambient cloud, condensations of dust and gas are observed to contain the protostellar embryos. These condensations, or 'cores', are extremely dense ($\sim 10^4$ particles cm^{-3}) and large (~ 0.1 pc), and so act as a shield against radiation from the formation of the star and the intra-cloud and interstellar radiation field (e.g. Krumholz et al. 2008). Due to the shielding nature of these cores, they are generally cold and have temperatures of 10–20 K (e.g. Johnstone et al. 2006; Rosolowsky et al. 2008), similar to the ambient cloud. Although H_2 is the most abundant molecule within these cores, it is especially hard observe in such cold environs due to its high excitation temperatures (e.g. Di Francesco et al. 2007). Fortunately, the densities and sizes can be traced in the sub-mm using either continuum emission from dust (e.g. Hatchell et al. 2005; Kirk et al. 2006; Schnee et al. 2010),

or excited line emission from the molecules that are abundant in the relatively cold medium. A variety of nitrogen, carbon, and oxygen species can be used at various temperatures and densities; N_2H^+, N_2D^+, DCO^+, HCO^+, CS, NH_3, ^{13}CO, and $C^{18}O$ (e.g. Zhou 1995; Kirk et al. 2007; Friesen et al. 2009; Pon et al. 2009; Friesen et al. 2010).

Embedded within the core is the protostellar system, which can be described as three separate yet integral parts: the central source, the circumstellar disk, and the enshrouding envelope. The central source, or protostar, is what will eventually become a main sequence star, once it has emerged from the dark core that surrounds it. The protostar emits radiation through various processes from its formation. Protostars will have achieved a high enough temperature and pressure at their core to induce deuterium fusion. Energy will also be released as the protostar contracts under gravity. As matter is accreted onto the protostellar surface, shocks are created which heat the surface and emit radiation (e.g. Calvet and Gullbring 1998; Shu et al. 1994). It is possible for these accretion shocks to dominate over the intrinsic stellar luminosity (e.g. Kenyon and Hartmann 1995; Dunham et al. 2010).

Surrounding the protostar is a disk at least 10–100 times less massive than the protostar. Protoplanets may eventually form inside the disk, and disk evolution itself is another field of study. The disk is also a source of radiation since as material in the disk flows slowly inwards through viscous dissipation, it releases gravitational energy (e.g. Shakura and Sunyaev 1973; Lynden-Bell and Pringle 1974; Pringle 1981). Angular momentum is conserved in this process, so the outer disk extends to larger radii. The disk is also heated by the protostar, and as the disk cools to establish a thermodynamic equilibrium the energy is re-radiated. The inner regions of the disk are extremely warm, and so radiate primarily in the near- and mid-infrared. The outer regions of the disk are much cooler, and so radiate primarily at longer wavelengths.

Surrounding the protostar and the disk is the protostellar envelope, and both the star and the disk accrete material from the envelope as it slowly collapses under gravity (e.g. Shu 1977). The envelope is heated from within by the formation of the protostar, and from without by the intra-cloud and interstellar radiation fields and cosmic rays; the energy will eventually be re-radiated at longer wavelengths. This envelope will not necessarily be spherically symmetric, and this structure can have important consequences for the formation of the protostar and the disk. Outflows and jets launched due to the formation of the protostar will carve cavities into the dense envelope as material is swept up. Rotation in the envelope can flatten the density

distribution of the envelope at small radii as material falls into the midplane (disk) at further distances from the protostar (e.g. Terebey et al. 1984). It is important to account for this geometry when studying the continuum emission from protostars deeply embedded within their natal envelopes.

Since the vast amount of dust within the envelope acts as a blanket, emission at short wavelengths is absorbed by the dust, which is heated to higher temperatures. In order to establish a thermal equilibrium, the dust then emits radiation at longer wavelengths. Since the emissive properties of dust are influenced by its chemical makeup, structure and size, this re-radiated long wavelength emission is able to escape the protostellar envelope. This necessitates the use of near- (0.7–2 μm, NIR), mid- (2–20 μm, MIR), and far- (20–350 μm, FIR) infrared observations, along with sub-millimetre (350–1000 μm) and millimetre (1–3 mm) observations, to study the protostellar environment. Most of the energy radiated away through the formation of the protostar will be observed at these wavelengths, and so by observing as much of the spectrum of a protostellar source as possible one can estimate the energy released. Although the radiation that is observed is reprocessed by the dust envelope, the amount of energy at each wavelength (called the spectral energy distribution, or SED), can have subtle differences depending on the internal characteristics of the protostar. In order to understand what is occurring within the protostellar envelope, it is necessary to model how the radiation is emitted and absorbed throughout the envelope (e.g. Adams et al. 1987; Whitney et al. 2003b; Robitaille et al. 2006).

It is believed that this theoretical description of a protostar embedded within its infalling envelope has an observational analog, given by the the spectral index α, defined as the logarithmic slope of the emergent flux ($\frac{dlog\lambda S_\lambda}{dlog\lambda}$) between 2–20 μm (Lada and Wilking 1984); in this scheme, the evolution of the protostar is divided up into classes (Lada 1987). Class I ($\alpha \gtrsim 0$) sources are those surrounded by significant amounts of dust and gas, and represent the early stages of protostellar evolution. Class II ($0 \lesssim \alpha \lesssim$ -2) sources are those surrounded by only tenuous dusty envelopes but a sizeable disk. Class III ($\alpha \lesssim$ -2) sources are not surrounded by significant amounts of dust and gas; their SED is basically that of a pre-main sequence star. Other indicators of evolutionary stage also exist, for example by detecting the existence of powerful collimated outflows originating from a protostar (e.g. Bontemps et al. 1996; Curtis et al. 2010). In instances where a source is believed to be young and in the process of evolving onto the main sequence, but its exact state is unknown, the generic term young stellar object (YSO) is used as a descriptor.

There are a number of well studied clouds within a few hundred parsecs of the sun, such as Perseus (e.g. Hatchell et al. 2005; Kirk et al. 2006; Ridge et al. 2006; Jørgensen et al. 2006; Rebull et al. 2007), Taurus (e.g. Ungerechts and Thaddeus 1987; Kenyon et al. 1990; Luhman et al. 2006; Nutter et al. 2008), Ophiuchus (e.g. Johnstone et al. 2000; Padgett et al. 2008; Ridge et al. 2006), and Orion (e.g. Johnstone et al. 2001, 2006; Bally et al. 2009). In particular, the Perseus Molecular Cloud has been observed from the optical to the millimetre using a variety of techniques (e.g. Kirk et al. 2006; Jørgensen et al. 2006; Rebull et al. 2007; Hatchell et al. 2005; Ridge et al. 2006; Greissl et al. 2007; Najita et al. 2000; Evans et al. 2003; Ward-Thompson et al. 2007), and its relatively close distance makes it an ideal testbed for star formation theories (e.g. Kirk et al. 2007, 2009; Evans et al. 2009; Jørgensen et al. 2007; Arce et al. 2010; Pineda et al. 2010; Hatchell et al. 2007; Hatchell and Fuller 2008). There is some disagreement over the exact distance to Perseus (e.g. Herbig and Jones 1983; Černis 1990; Ungerechts and Thaddeus 1987; Sun et al. 2006; Ridge et al. 2006; Černis and Straižys 2003), however in the following we adopt a distance to Perseus of 250 $\pm$ 50 pc; several authors have also adopted this distance (e.g Kirk et al. 2006; Jørgensen et al. 2006; Rebull et al. 2007; Evans et al. 2009; Jørgensen et al. 2007; Arce et al. 2010).

A number of previous studies based on the SED of YSOs have been conducted both in Perseus and in other star forming regions. Some (e.g. Jørgensen et al. 2006; Rebull et al. 2007; Forbrich et al. 2010) compiled observations of a number of different sources across a significant wavelength range, in order to build a comprehensive SED. These SEDs can then be fit to radiative transfer models of star formation (e.g. Adams and Shu 1986; Adams et al. 1987; Dullemond et al. 2001; Whitney et al. 2003b; Robitaille et al. 2007; Hatchell et al. 2007) or their positions in observed colour space can be analysed (e.g. Kenyon and Hartmann 1995; Allen et al. 2004; Gutermuth et al. 2004; Megeath et al. 2004; Muzerolle et al. 2004; Jørgensen et al. 2007, 2008). The SEDs have also been studied in the sub-mm (e.g. Hatchell et al. 2005; Kirk et al. 2006), by focusing on the large scale structure of the envelopes and the ambient cloud surrounding the YSOs.

In terms of observations, large scale surveys are useful as they provide a census of the protostellar population within the solar neighbourhood (the region of space within 500 pc), and can be combined for complementary datasets. In particular, this work has used the observations of two such surveys: the 'From Molecular Cores to Planet-forming Disks' (c2d) survey using the Spitzer Space Telescope (Evans et al.

2003) and the 'The COordinated Molecular Probe Line Extinction Thermal Emission' (COMPLETE) Survey of Star Forming Regions (Ridge et al. 2006). The c2d and COMPLETE surveys are very much complementary, and combining the two surveys can, for example, characterize the spectra of protostars from the mid-infrared to the submillimetre. Their surveys also utilized the Two-Micron All Sky Survey (2MASS) point source catalogue (Skrutskie et al. 2006) to not only extend the SED coverage into the near-infrared, but also to provide a measurement of the dust extinction (Lombardi and Alves 2001). The data utilized in this work comes from the c2d observations using IRAC, the InfraRed Array Camera (Jørgensen et al. 2006), the c2d observations using MIPS, the Multiband Infrared Photometer for SIRTF (Rebull et al. 2007), and the COMPLETE observations using SCUBA, the James Clerk Maxwell Telescope Submillimetre Common User Bolometer Array (Kirk et al. 2006).

As significant improvements to the theory and observations of star forming regions have been made, it is now becoming possible to do more than just determine the evolutionary stage of a YSO. Strenuous tests of evolutionary indicators (e.g. Robitaille et al. 2006; Hatchell et al. 2007; Enoch et al. 2009) significantly improve understanding and caution against incorrect classification. Building large grids of pre-computed models (e.g. Robitaille et al. 2006) is especially beneficial for large data sets, as the time required to find acceptable physical descriptions of each source is shortened considerably (e.g. Robitaille et al. 2007). Interesting YSO SED behaviour can be studied to learn more about the star formation process (e.g. Jørgensen et al. 2007, 2008; Riaz et al. 2009). By combining the large observational data set (Kirk et al. 2006; Jørgensen et al. 2006; Rebull et al. 2007) with a large grid of pre-computed SED models (Robitaille et al. 2006), this thesis hopes to study the physical characteristics of a sample of deeply embedded protostars (Jørgensen et al. 2007).

In the embedded stage of star formation, when the radiation emitted from the protostar is absorbed by the dust in the surrounding envelope, there should be very little observable flux between 1–10 μm (Hartmann 1998). Observing flux at these wavelengths from deeply embedded protostars (e.g. Jørgensen et al. 2006, 2007, 2008) presents an interesting theoretical problem which should be tackled. The most pressing question to answer is what exactly is allowing this short wavelength flux to escape the envelope? One plausible explanation is that the outflows driven by protostellar formation carve low density cavities through the envelope, which provide a means for short wavelength photons to escape the dense envelope. Certainly, this is evident in radiative transfer models that incorporate outflow cavities (e.g. Whitney et al.

2003b). The formation of planets or multiple stellar systems within the core will also accrete the innermost portions of the envelope, essentially carving large holes in the envelope through which photons can also escape (e.g. Jørgensen et al. 2005). As these explanations have significant implications regarding the earliest stages of star formation and how they are studied, it is important to address this question.

Given that a sample of deeply embedded protostars within Perseus now exists (Jørgensen et al. 2007) it is now possible to study what physical parameters describe these sources, such as the size of the outflow cavity and the inner envelope radius. Utilizing a suite of radiative transfer models (Robitaille et al. 2006) these embedded protostars can be studied, not on an individual source-by-source basic, but as an ensemble of deeply embedded objects. It will then be possible to probe, in a statistically significant way, the earliest stages of star formation. This thesis proposes that, by fitting radiative transfer models to a set of deeply embedded protostars in Perseus, much can be learned about the internal structure of protostellar systems in the earliest stages formation.

The thesis is organized as follows. Chapter 2 will discuss how parameters of the radiative transfer code affect the observed model YSO SED. Chapter 3 will discuss the differences between the observational and theoretical description of the cores in Perseus, and demonstrate how these differences can be overcome with a simple toy model. Chapter 4 contains the results of fitting a pre-computed grid of radiative transfer models (Robitaille et al. 2006) to each source in Perseus, and Chapter 5 provides a discussion of these results.

Chapter 2

Radiative Transfer Modeling of the Perseus Protostars

2.1 Introduction

In radiative transfer modeling, radiation is followed along its path through the protostellar system as it is absorbed and scattered by the surrounding dust and gas. There are many numerical and analytical methods to solve the radiative transfer equation, which describes how the change in emission at any one point is the difference between the amount of radiation absorbed and emitted at that point. As the complexity of the geometry of the medium is increased and as more energy transport processes are included, the radiative transfer equation becomes tougher to solve. For example, including a bi-polar cavity within the envelope presents the simulated photons with a scattering surface. Once the radiation has escaped the protostellar system, its wavelength is determined, and after following many photons an SED can be built.

The radiative transfer code used in the Robitaille et al. (2006) model grid averages the flux along the polar angle θ into ten bins evenly spaced in $\cos(\theta)$. There are a number of features evident in the spectra: a deep silicate absorption feature at 10 μm, a steep drop through 2–8 μm, and the dusty blackbody curve long-ward of 15 μm. In Figure 2.1, the SED of a 2 $M_\odot$ protostar with a surface temperature of 4100 K is shown; the total luminosity of this model is 154 $L_\odot$. As the inclination changes from 18° (pole-on) to 87° (edge-on), the flux in the NIR and MIR (0.7–20 μm) increases, especially between 18° and 32°. This is due to the fact that a small bi-polar cavity ($\sim$ 2°) has been placed in the envelope of this model; as the density in the cavity

is lower than in the envelope, more short-wavelength photons can escape along the polar directions. In contrast, the SED in the FIR and sub-mm does not exhibit much change with inclination, since most of the photons at these wavelengths were emitted from the warm dust within the envelope and disk. Although the disk emission is dependent on the inclination (see §2.2.3), the envelope emission is not, and so in the case where the envelope emission dominates the disk emission there should be little change in the SED with inclination. The emission in the FIR resembles a blackbody, with a emission peak around 45 μm, albeit with a steeper drop in the sub-mm due to the dust grain sizes being on the order of a few hundred μm and the envelope becoming optically thin.

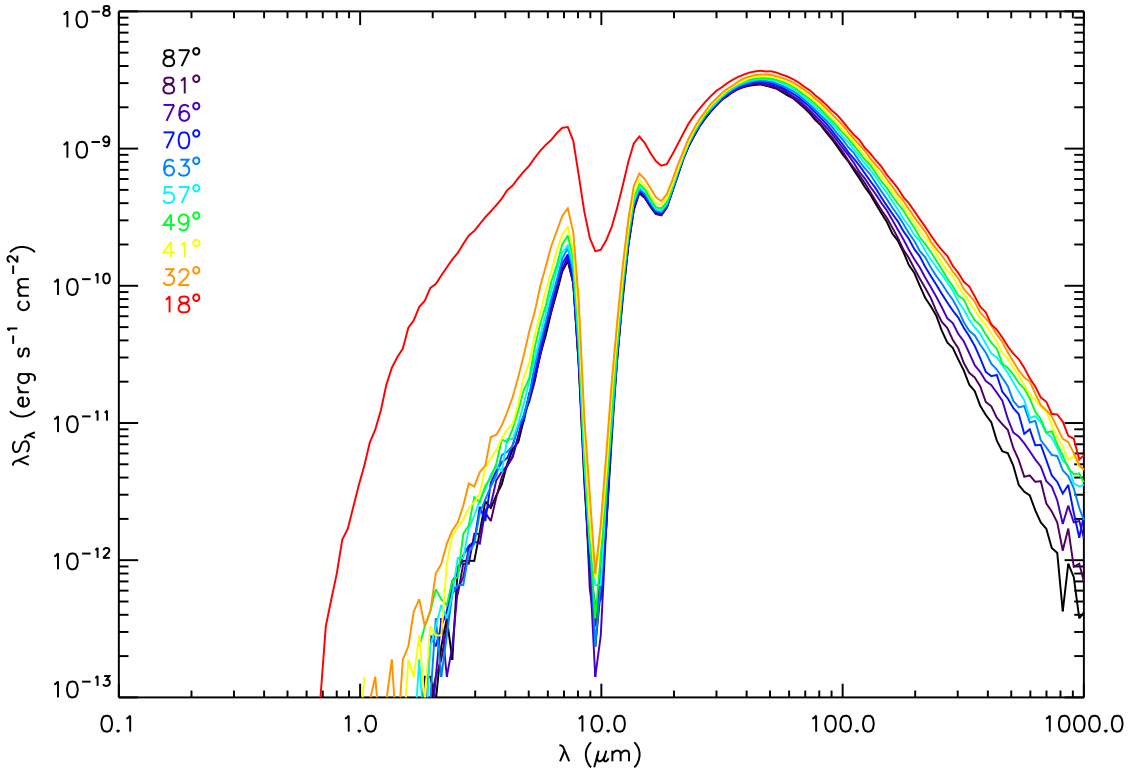

Figure 2.1: The spectra for model 3002265 from Robitaille et al. (2006) along 10 different inclinations. Numerical resolution effects are evident at the short and long wavelengths as noise in the spectra.

2.2 The Radiative Transfer Models

The radiative transfer model, as well as the grid, used to model the Perseus data will be briefly described here. For a more indepth description of the code, see Whitney et al. (2003b,a, 2004); for the radiative transfer grid, see Robitaille et al. (2006); and for the fitting algorithm, see Robitaille et al. (2007). Most of the following discussion on how different parameters of the YSO models affect the SED can be found in Whitney et al. (2003b,a, 2004) and Robitaille et al. (2006).

The Robitaille et al. (2006) model grid is based on a two-dimensional monte-carlo code, symmetric in the midplane and about the azimuthal axis. The code accounts for scattering, absorption, and emission of model photons, in order to more accurately reproduce the observed properties of YSO SEDs. Since scattering is included, the code can produce polarization spectra at all of the output wavelengths, as well as images of the YSO. Each model photon also remembers where and how it was emitted, so the total SED can be split up into the various contributions from scattering, thermal emission from the envelope and disk, as well as from the protostellar surface. The emission from the YSO is averaged along ten polar angles, equally spaced in $\cos\theta$, in order to take full advantage of how the YSO system geometry affects the observed SED. Finally, the code allows for the SED to be observed at various physical radii, to mimic the observable aperture limitations. This is important when considering how the emitted flux from the YSO changes with radius; for example, in an edge-on model with bipolar cavities, the amount of scattered light into the observed line-of-sight will increase with increasing radius. As more of the scattering surface is observed, this edge-on model will show increasing flux at short wavelengths where scattering is important, and so the same model will have different colours (ratios of fluxes in two different wavebands) when observed on different scales.

The 14 model parameters that were varied in order to build the Robitaille et al. (2006) model grid are shown in table A.1. The parameters can be grouped by whether they describe the protostar, the protostellar envelope, or the protostellar disk. In the discussion that follows, emphasis will be on how each parameter affects the YSO SED, rather than on how each parameter was varied to create the grid (Robitaille et al. 2006).

2.2.1 Stellar Parameters

The mass (M_*) and age (t_*) of the protostar define the overall characteristics of the YSO system. Once M_* and t_* are known, the stellar radius (R_*) and temperature (T_*) are found via fitting to the Pre-Main Sequence stellar evolution grids of Siess et al. (2000) and Bernasconi and Maeder (1996). M_*, R_* and T_* set the emergent protostellar spectrum, and combined with t_*, set the rough evolutionary class of the YSO (Lada 1987). 'Younger' YSO models, most likely similar to observed Class 0/I objects, will still be embedded in their protostellar envelopes, as well as the molecular core within which it was born (Jørgensen et al. 2007). This will significantly affect the YSO SED (§2.2.2) at all wavelengths between 0.1 μm and 1000 μm. Older YSO models, most likely similar to observed Class II objects, will have dispersed most of their envelopes, although the disk encircling the protostar will still influence the SED (e.g. McCabe et al. 2003; Millan-Gabet et al. 2007; Najita 2004; Wyatt 2008). Despite these connections, it is still extremely difficult to deduce the temperature, mass, and radius for deeply embedded protostars (White et al. 2007).

2.2.2 Envelope Parameters

The envelope parameters with the greatest influence on the YSO SED are the envelope accretion rate ($\dot{M}_{env}$), the envelope outer radius (R_{env}^{max}), and the cavity opening angle (θ_{cav}).

Envelope Accretion Rate

The envelope parameter with the biggest influence on the YSO SED is the envelope accretion rate, because it influences the infalling envelope density structure, and because it sets the timeline for accumulation of mass onto the protostar (Hartmann 1998). In order to model the dense dust and gas envelope for the radiative transfer code, Whitney et al. (2003b) and subsequently Robitaille et al. (2006) used the rotationally flattened infall profile (Ulrich 1976; Terebey et al. 1984):

$$\rho(r,\theta) = \frac{\dot{M}_{env}}{4\pi\sqrt{GM_*}} r^{-3/2} \left(1 + \frac{\mu}{\mu_o}\right)^{-1/2} \left(\frac{\mu}{\mu_o} + \frac{2\mu_o^2 R_c}{r}\right)^{-1} \tag{2.1}$$

where R_c is the centrifugal radius of the disk, μ is the cosine of the polar angle θ, and μ_o is the cosine of the angle of the streamline of infalling particles. The centrifugal radius

influences the density structure when the envelope has some rotation, since collapse requires the redistribution of angular momentum (Hartmann 1998). Dust and gas close to the axis of rotation will have low angular momentum, and so these particles can undergo almost radial freefall onto the disk and the protostar. Dust and gas that is further out will have more angular momentum, and will not be able to collapse radially; instead, they will flow along streamlines into the midplane of the envelope (Hartmann (1998), Terebey et al. (1984)), accreting onto the disk approximately at R_c. This rotational collapse causes a flattening of the infall density profile for small radii ($r \lesssim R_c$) to $\rho \propto r^{-1/2}$, whereas at large distances the infall density profile remains $r^{-3/2}$.

The influence of the accretion rate on the density influences the shape of the YSO SED, especially in the FIR and sub-mm. Higher accretion rates (Equation 2.1) increase the column density of the envelope, and therefore reduce the amount of UV, Optical, and NIR light that can escape. This light is absorbed by the envelope and re-processed into longer wavelength light. As such, the SED will resemble Figure 2.2, whose envelope accretion rate is three times higher than the model shown in Figure 2.1. Whereas in Figure 2.1 the SED in the MIR changed with inclination, the SED shown in Figure 2.2 looks exactly the same at all inclinations. There is almost no flux at wavelengths less than 20 μm at a limit of 10^{-14} erg s^{-1} cm^{-2}. The SED overall looks like that of a warm dusty blackbody, with a peak flux occurring at a wavelength of about 90 μm, much longer than the peak emission wavelength in Figure 2.1. In fact, by the observational definitions of Andre et al. (1993) and Chen et al. (1995), this SED would be defined as a typical Class 0 since its sub-mm luminosity is approximately 1% of the bolometric luminosity, and it has a bolometric temperature of ≈ 42 K.

This SED can be simply understood by looking at the definition of the optical depth, τ_λ:

$$\tau_\lambda = -\int \kappa_\lambda \rho(r) dr \tag{2.2}$$

Here κ_λ is the opacity, the absorbing cross section (area) per unit mass at the wavelength λ, and $\rho(r)$ is the density at a radius r. Typically the envelope is not spherically symmetric, and so the integral will need to be performed over polar angle as well, but we ignore this for simplicity. The term *optically thick* describes when τ_λ is large (typically $\tau_\lambda \gg 1$), and *optically thin* describes when τ_λ is small ($\tau_\lambda \ll 1$). One way to think of the optical depth is as a measure of the radius within the envelope where the

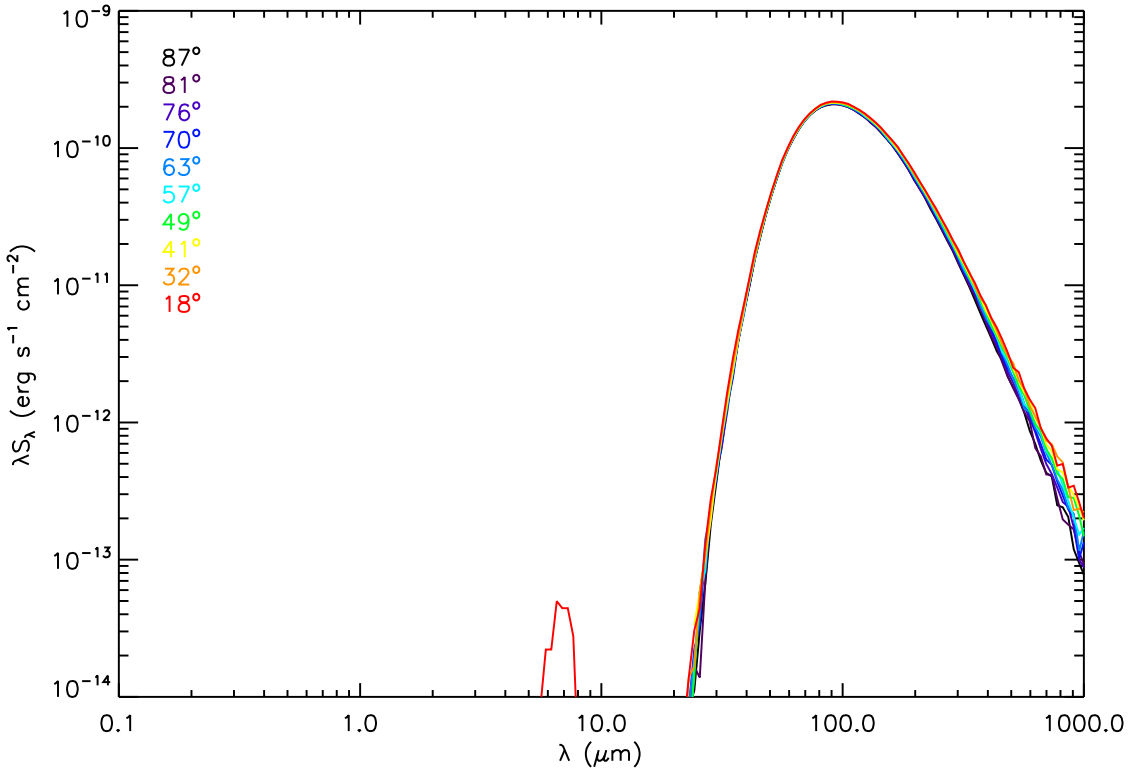

Figure 2.2: The spectra for model 3001181 along 10 different inclinations. Despite the changing inclinations, almost no flux is emitted short of 20 μm. The small peak at 7 μm is actually emission from the envelope, rather than emission from the disk or protostar, and is almost 4 orders of magnitude below the peak flux.

column density is low enough so that a photon of a given wavelength can escape. As the optical depth at all wavelengths increases with density, the envelope only becomes optically thin at larger radii.

If a photon is absorbed by a dust grain, the temperature of that dust grain will increase, until an equilibrium is reached where as much energy absorbed by the dust grain is emitted as radiation. Since the dust grains will emit like a grey body ($F_\lambda = \kappa_\lambda B_\lambda$), the equilibrium temperature of the dust grain defines the location of the emission peak and the intensity of the emission. There is a caveat, though, as the dust grains are less than a millimetre in size, and so the long wavelength emission must fall off faster than a normal blackbody. At larger envelope radii, or conversely lower optical depth, more photons will be able to escape, and the equilibrium temperature will be lower. As the optical depth is proportional to the density, the characteristic temperature of the envelope will be cooler for lower density envelopes than for higher

density envelopes at the same physical radius from a protostar. This characteristic temperature is inversely related to the wavelength at which the SED peaks in the FIR, and so a denser protostellar envelope will have its flux peak at a longer wavelength.

Envelope Outer Radius

The outer envelope radius helps determine the amount of mass within the envelope, which in turn influences the amount of sub-mm flux emitted from the envelope. In the Robitaille et al. (2006) model grid, the outer envelope radius was defined as the approximate radius at which the optically thin dust and gas temperature decreases to 30 K:

$$R_{env}^{max} \sim \frac{R_*}{2}(\frac{T_*}{30\ \mathrm{K}})^{5/2} \tag{2.3}$$

Since R_{env}^{max} depends only on R_* and T_*, larger and hotter protostars will have larger, and thus more massive, envelopes. The envelope radius will affect the amount of MIR flux as well, due to scattering events of the envelope cavity walls. Also, larger envelope radii implies more mass ($M_r \propto r^{3/2}$ from Equation 2.1) at lower temperatures (§2.2.2), affecting the amount of sub-mm flux. When the envelope becomes optically thin to radiation at a particular wavelength, the emission becomes directly related to the emitting mass in the envelope.

This is can be easily explained through the most basic equation of radiative transfer:

$$\frac{dI_\lambda}{d\tau_\lambda} = I_\lambda - S_\lambda \tag{2.4}$$

Where S_λ describes the radiation emitted at a point described by the optical depth τ_λ, and I_λ represents the emission that has been absorbed up to that point. The solution to radiative transfer equation is given by integrating over the optical depth:

$$I_\lambda(\tau_\lambda = 0) = I_{\lambda_o} e^{-\tau_\lambda} + S_\lambda(1 - e^{-\tau_\lambda}) \tag{2.5}$$

This equation re-iterates the points that have been made previously; in a small region of an absorbing medium at high optical depth, most of the radiation passing into the region will be absorbed, and so the radiation from that region is due to emission from the medium.

Since this equation is valid at any point and at any scale (in other words, so long as Equation 2.4 is satisfied, Equation 2.5 is satisified), it is reasonable to assume that the solution holds when the entire envelope is considered (in other words, the integration

limits are from core-edge to core-edge). This means the I_λ term in Equation 2.5 describes the background radiation field exterior to the envelope, and the S_λ term comprises all the emission from within the envelope itself. Furthermore, the average envelope density will be low, and so the optically thin limit approximation ($e^{-\tau_\lambda} \approx 1 - \tau_\lambda$ for $\tau_\lambda \ll 1$) can be made:

$$I_\lambda = I_{\lambda_o}(1 - \tau_\lambda) + S_\lambda \tau_\lambda$$

Where I_λ is the total emission from the surface of the envelope and $I_{o\lambda}$ is the background radiation field. Assuming the background emission can be subtracted off (a technique utilized in SCUBA observations) and is very low, the total emission from the envelope becomes $S_\lambda \tau_\lambda$. From the definition of τ_λ (Equation 2.2), if the opacity κ_λ is constant throughout the core then Equation 2.2 becomes:

$$\tau_\lambda = \kappa_\lambda \Sigma \tag{2.6}$$

Where Σ is the column density of the envelope integrated along a sightline. Thus, I_λ is directly proportional to the column density of the emitting medium so long as the optically thin limit applies.

As the Robitaille et al. (2006) models define their envelope radius using 30 K, warmer than what is generally found through observations (Johnstone et al. 2006; Rosolowsky et al. 2008), the radiative transfer model envelope radii are a few times smaller than the radii of the observed cores (Kirk et al. 2006). In order to avoid confusion, the use of the term *envelope* will describe characteristics of the models, whereas use of the term *core* will describe characteristics of the what was observed using SCUBA.

Envelope Cavity Opening Angle

Bipolar outflows originating from protostars are ubiquitous in star forming regions (e.g. Curtis et al. 2010; Davis et al. 2010) due to their inherent connection with the star formation process (Ray et al. 2007). They are believed to be launched from the protostellar disk via some sort of magnetohydrodynamic (MHD) mechanism (Hartmann 1998), but at present it is unclear what this mechanism is and whether it is launched from the inner disk regions (e.g. Shu et al. 1994; Shang et al. 2007) or throughout the disk (Pudritz et al. 2007). These high velocity outflows are highly

collimated, sweeping up dust and gas and carving cavities into the envelope as the ejecta travels into the surrounding molecular cloud (Hartmann 1998; Ray et al. 2007). The energy of the outflowing material is eventually dissipated as it shocks against the ambient cloud (Bally et al. 2007) and against the walls of the cavity in the envelope. Although the topic of outflows and their connection to the formation of protostars is a topic of much research, what concerns the discussion here is the angular size of the outflow cavity, θ_{cav}.

The presence of a cavity in the envelope can provide a means for short wavelength ($\lambda \lesssim 10$ μm) flux to escape and be observed along all inclinations, which can be described through Figure 2.3. In Figure 2.3a, the total SED built from the star, disk, and envelope is shown. In Figure 2.3b, the SED comprising all photons that were scattered before being 'observed' is shown. In Figure 2.3c, the SED of all photons not absorbed or scattered by dust is shown. In Figure 2.3d, the SED of all photons emitted as thermal radiation from the dust in the disk and envelope is shown.

As the outflow sweeps material out of the envelope, the resulting cavity will have a lower density (Smith et al. 2010; Moriarty-Schieven et al. 1995) and thus a lower optical depth. Short wavelength photons emitted along lines of sight through the cavity can then escape the dense envelope, and allow young protostars to be observed in the MIR (e.g. Jørgensen et al. 2006; Evans et al. 2009; Dunham et al. 2008). An example of this effect is shown in Figure 2.3c; in this model, the cavity opening angle is almost 17° wide. The most pole-on inclination is at 18°, which has an almost clear view through the cavity to the very centre of the envelope. The SED shown here comprises photons that traveled directly to the 'observer' from the surface of the protostar without encountering a dust particle. The pole-on inclination (red line) shows a significant contribution of these direct photons at short wavelengths, to about 0.3 μm (UV wavelengths). When compared to the full SED in Figure 2.3a, it is evident that these direct photons are the dominant influence at the short wavelengths when viewed pole-on. In contrast, as the inclination angle increases (the orange line corresponds to an inclination of 32°), the number of photons able to be directly observed from the protostellar surface decreases dramatically (about three orders of magnitude in flux at 1 μm). The higher inclinations have lines of sight through more and more of the dense envelope.

It is evident in Figure 2.3a that although the flux at $\lambda \approx 2$ μm is almost as large as the peak flux at $\lambda \approx 50$ μm, the decrease in flux in the full SED as the inclination angle increases is not as drastic as in the SED comprised only of directly observed

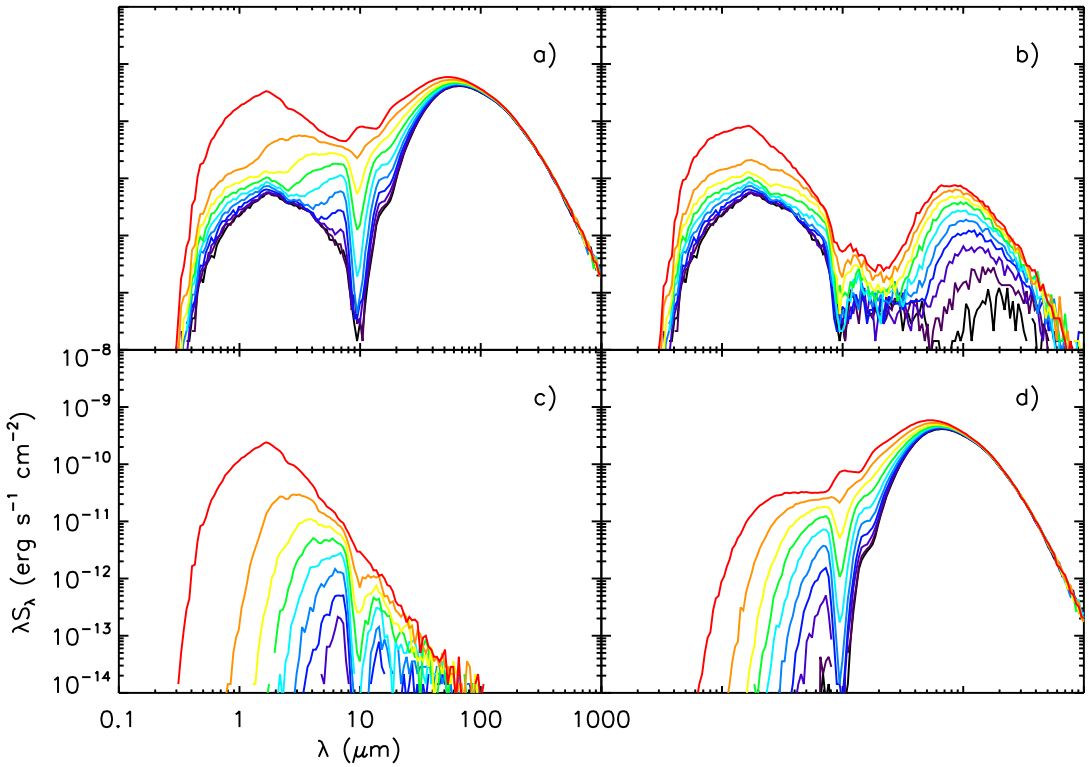

Figure 2.3: The spectra for model 3004252 along 10 different inclinations. The coloured lines represent the same inclinations as in Figure 2.1. The scale on all the plots are the same. The protostar in this model has a mass of 1.14 $M_\odot$ and a temperature of 4100 K. a) The full SED of the model at all inclinations. b) The scattered SED, comprising all model photons whose last point of origin was a scattering event. c) The direct SED, comprising all model photons emitted from the stellar surface and not absorbed by dust. d) The thermal SED, comprising all photons whose last point of origin was thermal emission from warm dust.

photons. Furthermore, the full SED shows relatively the same amount of flux at all wavelengths less than 2 μm as the inclination is varied, which is not the case for the direct SED. Thermal emission from the disk and envelope (the disk dominates the thermal flux for $\lambda \lesssim 10$ μm) contributes at long wards of $\lambda \sim 5$ μm, as shown in Figure 2.3d by the bump at 8 μm, but the thermal SED follows a similar trend as the direct SED down to 1 μm and beyond.

What accounts for the short wavelength flux at oblique inclinations is the scattering of short wavelength photons off of the cavity walls into the line of sight of the observer. The SED shown in Figure 2.3b is built from all model photons that

were scattered before being observed.. Even at inclinations much larger than the cavity opening angle in the model depicted, scattering can account for a significant contribution to the flux for $\lambda \lesssim 10$ μm. Furthermore, the amount of scattered flux that is observed as the inclination increases does not suffer the same attenuation as the direct flux SED in Figure 2.3a. The reason that scattered photons can traverse through the envelope and still be observed is due to the fact that the envelope is densest (optically thick) in the innermost regions. If a photon, initially emitted along a line of sight through the cavity, scatters off the cavity walls at an oblique angle, it can pass through regions of the envelope that are less dense and travel relatively unimpeded to the observer.

The amount of scattered flux visible at large inclinations depends on the density of the envelope and the size of the cavity opening angle. Dense envelopes or small cavity opening angles require scattering events to happen at larger radii, significantly reducing the amount of observed flux at the most edge-on inclinations. Assuming the protostar radiates isotropically, photons whose emission direction intersects the cavity wall at small radii and scatter at oblique angles will still pass through a significantly dense envelope. Conversely, tenuous envelopes or large cavity opening angles increase the amount of scattered flux at all inclinations. A simple schematic of this behaviour is shown in Figure 2.4.

The presence of the cavity wall can also provide a working surface for the outflow to shock against, producing emission. Outflow shocks are an important source of feedback in star formation (Bally et al. 2007), and large scale molecular outflows can be traced via molecular line emission in a number of star forming regions (e.g. Ray et al. 2007; Moriarty-Schieven et al. 1995; Smith et al. 2010). Since the Robitaille et al. (2006) models did not include shock heating as an emission source, they may be unable to reproduce the observed emission at 4.5 μm(§3.2.1).

2.2.3 Disk Parameters

The disk parameters with significant influence on the YSO SED are the accretion rate ($\dot{M}_{disk}$), mass (M_{disk}), and the inner (R_{disk}^{min}) and outer (R_{disk}^{max}) radii.

Disk Mass

The mass of the disk can influence the observed SED both in the MIR, through the disk accretion rate, and in the FIR and sub-mm. In the absence of a significantly

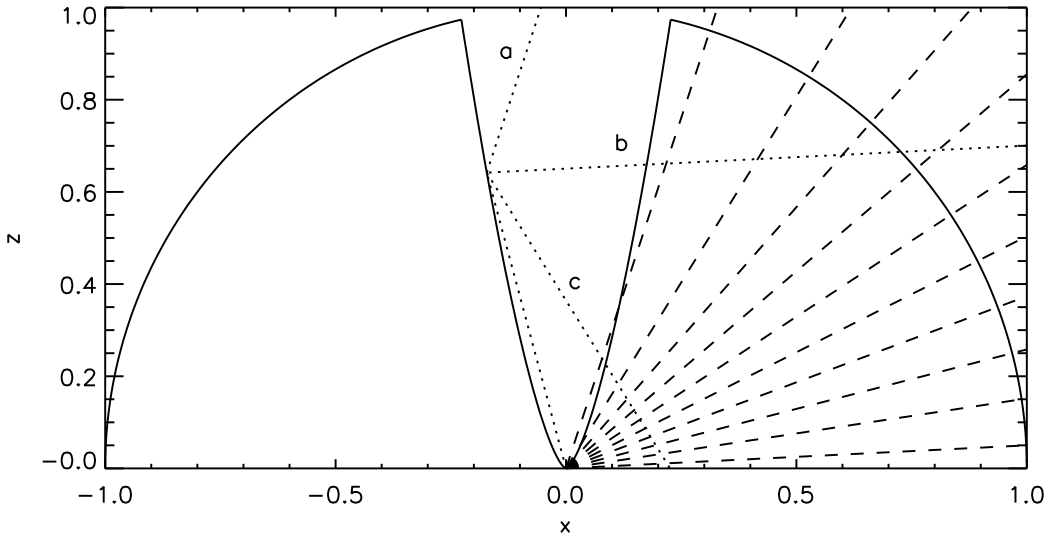

Figure 2.4: A schematic of a scattering event in the model in the x-z plane. The solid lines represent the outline of the envelope and the cavity, with the protostar at the centre. The dashed lines represent the 10 inclinations within which the models bin the observed flux. A photon, represented by the dotted line, is emitted from the protostar and scatters off the cavity wall some distance away. If the photon scatters along path *a*, inclined to 18°, it will still pass through the cavity and easily escape. If the it scatters along path *b*, inclined to 87°, the density in the envelope has decreased to a point that the photon has a relatively high chance of passing through unimpeded. If it scatters along path *c*, inclined to 122°, the photon will still pass through dense portions of the envelope and be absorbed.

dense envelope surrounding the protostar, the disk can provide most (or all) of the flux in the FIR and sub-mm. The protostellar disks are irradiated in a similar fashion as the protostellar envelope, so they will produce an SED similar to the envelope. In Figure 2.5, the similarities between the SED of the disk and envelope are highlighted. Figure 2.5a shows the SED of a 0.1 $M_\odot$ protostar surrounded by a 0.011 $M_\odot$ disk and a 0.024 $M_\odot$ envelope. Figure 2.5b shows the output stellar spectrum (photons emitted from the protostellar surface and not *absorbed* by dust), Figure 2.5c shows the disk thermal spectrum, and Figure 2.5d is the envelope thermal spectrum.

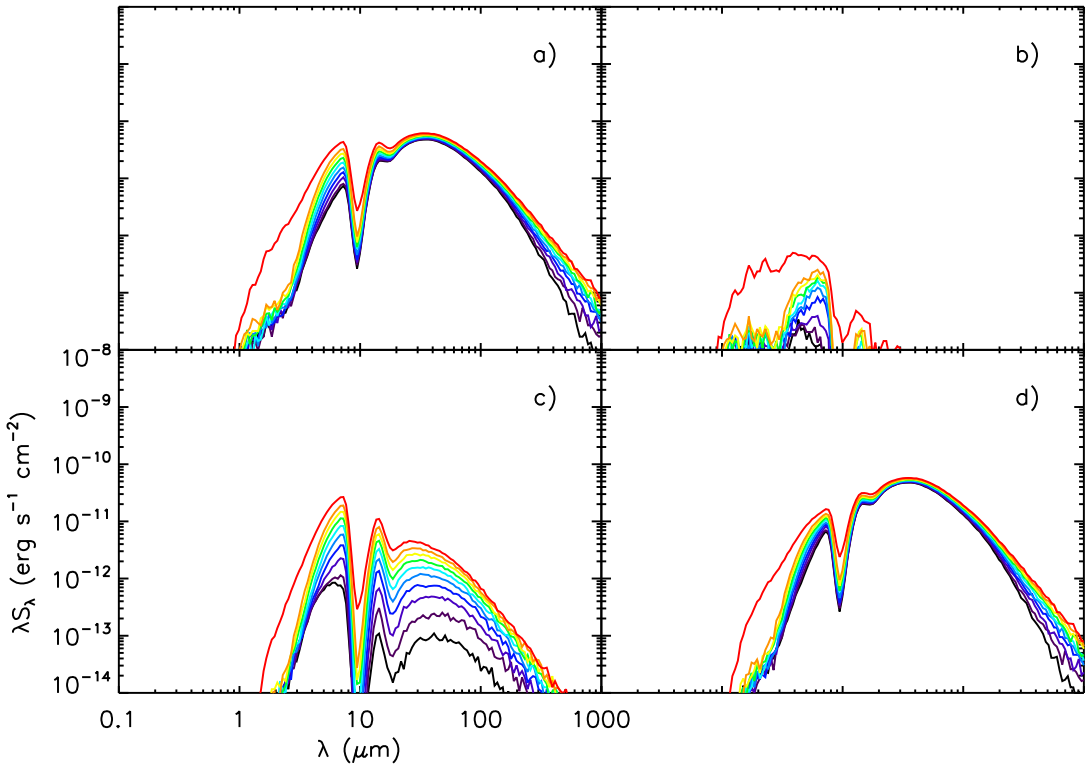

Figure 2.5: The spectra for model 3012582 along 10 different inclinations. The scale and colours are the same as Figure 2.1. a) The total SED given by the stellar, disk, and envelope emission. b) The stellar SED; the protostar mass in this model is 0.1 $M_\odot$ and a temperature of 2500 K. c) The disk SED; significant MIR flux stems from the warm inner regions of the disk, and the FIR and sub-mm flux shows the same slope as in the envelope. d) The envelope SED.

The warm inner regions of the disk will produce significant flux in the MIR, which is evident in 2.5c, especially in the wavelength range 2–10 μm, which contain the IRAC wavebands. Comparing the SED in this wavelength range to the model envelope SED, Figure 2.5d, the mid-latidude and pole-on inclinations produce roughly the same amount of flux as the envelope. The shape of the SEDs for both the disk and envelope in this wavelength range are also similar, with the relatively steep increase from ~ 1 μm to a peak at ~ 7 μm, and then the deep 10 μm silicate feature. The outer regions of the disk, which are much cooler, will emit primarily in the FIR and sub-mm, and have the same slope ($\frac{\mathrm{d}\log \lambda S_\lambda}{\mathrm{d}\log \lambda}$) in the long wavelength regime as the envelope SED.

Despite this, there are a few differences between the disk and envelope SEDs in

Figure 2.5. The disk SED decreases at all wavelengths as the inclination goes from pole-on (18°) to edge-on (87°), due to the density profile of the disk. The Robitaille et al. (2006) model grid used a flared accretion disk (Lynden-Bell and Pringle 1974; Pringle 1981; Bjorkman 1997) using the viscosity parameterization α_{disk} of Shakura and Sunyaev (1973) in cylindrical polar coordinates:

$$\varrho(\varpi, z) = \varrho_o(1 - \sqrt{\frac{R_*}{\varpi}})(\frac{R_*}{\varpi})^{\beta+1} \exp\left[-\frac{1}{2}(\frac{z}{h})^2\right] \tag{2.7}$$

where ϱ is the disk density, ϖ and z are the radial and vertical coordinates (the disk is azimuthally symmetric), h is the disk scale height, and β is the disk flaring power ($h \propto \varpi^{\beta}$). In Figure 2.5, the inner disk radius is approximately equal to the dust sublimation radius, which is about 5 R_* (20 $R_\odot$ or 0.094 AU), and the outer radius is approximately 1.79 AU, so the disk must be extremely dense to have a mass of 0.011 $M_\odot$. In other words, it is extremely optically thick. Any MIR emission from the warm inner regions of the disk, emitted along the edge-on inclinations, will be absorbed by the disk at larger radii, which will cause the decrease in flux along those sight-lines. This is exacerbated by the flaring of the disk, since emission from the warm inner regions will irradiate the cool outer regions where the disk is thicker.

The disk flux is more than an order of magnitude lower than the envelope flux at the long wavelengths because it is optically thick. This means that the flux is not directly related to the density (and hence mass) of the disk, only on the temperature, radius, and inclination. For example, an estimate (Hartmann 1998) of the flux at 850 μm from a disk similar to the one in the model shown in Figure 2.5 can be made given some straightforward approximations. Assuming the disk is seen face on, the flux would be approximately 1.1×10^{-14} $(\frac{d}{250\text{ pc}})^{-2}$ erg s^{-1} cm^{-2}. The flux at 850 μm from an envelope similar to the one shown in Figure 2.5 is about 2.8×10^{-13} $(\frac{d}{250\text{ pc}})^{-2}$ erg s^{-1} cm^{-2}.

Disk Accretion Rate

The disk accretion rate influences the YSO SED since it is a source of luminosity. As material falls in from the disk onto the stellar surface, it produces shocks at the stellar surface (e.g. Calvet and Gullbring 1998). Radiation from the formation of the protostar will be absorbed and re-radiated by the dusty disk, in a similar fashion as the envelope (e.g. Hartmann 1998). Furthermore, as material accretes through

the disk, it will dissipate its gravitational energy, some of which is converted to hermal radiation(e.g. Shakura and Sunyaev 1973). Since the Robitaille et al. (2006) model grid used the α_{disk} model (Shakura and Sunyaev 1973), the accretion rate is determined by (Pringle 1981; Bjorkman 1997):

$$\dot{M}_{disk} = \alpha_{disk}\rho_o h_o^3 \sqrt{\frac{18\pi^3 G M_*}{R_*^3}} \tag{2.8}$$

Where the disk viscosity is given by the sound speed c_s parameterized by α_{disk}.

Once the infalling mass reaches the inner disk radius, it will fall onto the surface of the protostar, producing an energetic shock. In models of this infall (e.g. Shu et al. 1994; Calvet and Gullbring 1998), the interaction between the magnetic field of the protostar and the rotating disk truncates the disk further out than the co-rotation radius (the radius at which the rotational velocity of the disk is equivalent to the surface rotation velocity of the protostar). As mass falls past the disk truncation radius, it streams along the magnetic field lines of the prototstar at near freefall velocities. The Robitaille et al. (2006) model grid modeled the emission spectrum of the accretion shock using the method of Calvet and Gullbring (1998), who calculate the accretion luminosity L_{acc} to be:

$$L_{acc} = (1 - \frac{R_*}{R_{disk}^{min}})\frac{G M_* \dot{M}_{disk}}{R_*} \tag{2.9}$$

As the Robitaille et al. (2006) model grid releases the accretion spectrum with the protostellar emission, $L_{tot} = L_{acc} + L_*$, where L_* is given by the Stefan-Boltzmann law:

$$L_* \equiv 4\pi R_*^2 \sigma T_*^4 \tag{2.10}$$

Depending on R_*, M_*, R_{disk}^{min}, and $\dot{M}_{disk}$, the accretion luminosity can dominate the total luminosity of the protostellar system, and thus the 'stellar' emission spectrum.

In the Robitaille et al. (2006) model grid, there was no effort to connect the disk accretion rate with the envelope accretion rate, since the authors wanted to be able to fit as wide a range of sources as possible. This allows for models in which $\dot{M}_{env}$ or $\dot{M}_{disk}$ can be two or three orders of magnitude larger than the other, presenting a substantial problem for the lifetimes of disks. In the canonical progression of protostellar formation (e.g. Adams et al. 1987; Lada 1987; Shu 1977; Hartmann 1998), the disk is formed from the collapse of the envelope, and remains behind after

the envelope has been dispersed. Estimates of the lifetime of the protostellar (Class I) stage are typically 2–5$\times10^5$ yr (e.g. Kenyon and Hartmann 1995; Hatchell et al. 2007; Evans et al. 2009). Especially in the Class I phase, disks with accretion rates orders of magnitude lower than the envelope infall rate will become unstable.

For example, a typical predicted envelope infall accretion rate for the formation of low-mass protostars is 2×10^{-6} $M_\odot$ yr^{-1} (Shu 1977). Assuming an envelope of 1 solar mass, it would take 5×10^5 yr for the envelope to completely collapse assuming 100% efficiency (envelope mass not lost due to outflows or other mechanisms). Suppose a disk forms around the protostar, with M_{disk} = 0.5% M_* , and $\dot{M}_{disk} = 10^{-3}\dot{M}_{env}$, and the accretion rates stay constant with time. Since most of the infalling mass will accrete onto the disk (§2.2.2), after only 5×10^4 yr the disk mass could be as much as 70% of the protostar mass. A disk with such a high mass ratio would be extremely unstable to fragmentation, self-gravitation, or a complete collapse onto the protostar (e.g. Shu et al. 1990; Vorobyov and Basu 2006; Durisen et al. 2007), and would be more massive than most observed disks in nearby star forming regions (e.g. Andrews and Williams 2005, 2007).

Clearly, such large discrepancies between the disk and envelope accretion rates cannot be sustained throughout the formation of the protostar. Since the Robitaille et al. (2006) grid were not interested in describing the evolution of the system, it did not matter if the accretion rates could not be sustained. It only mattered that a given source could be fit well by a set of physical parameters, regardless of the implications. When dealing with the envelope and disk accretion rates, it should be remembered then that these parameters do not necessarily describe how the system progressed from pre-stellar dense core to protostellar system.

Since most theoretical investigations of the collapse of a pre-stellar core into a protostellar system assume constant accretion rates (e.g. Shu 1977; Terebey et al. 1984; Whitney et al. 2003b; Dunham et al. 2010) so long as a mass reservoir exists (e.g. Vorobyov and Basu 2005a), clearly the disk accretion rate itself must vary with time in order to satisfy the observations of disks around young stars. A number of authors (e.g. Vorobyov and Basu 2005b, 2006; Enoch et al. 2009; Dunham et al. 2010) have suggested that the idea of a variable disk accretion rate is a solution to the so-called 'Luminosity Problem' (e.g. Hartmann 1998). The luminosity problem is that the accretion luminosity (c.f. Equation 2.9) predicted using, for example, an infall rate of 2×10^{-6} $M_\odot$ yr^{-1}, is much higher than what is observed in the majority of low mass star forming regions (e.g. Kenyon and Hartmann 1995; Evans et al. 2009). If

the disk accretion rate is allowed to fall to a few orders of magnitude smaller than the envelope infall rate, this would match the observed luminosity distribution. As the disk builds enough mass to become unstable, it rapidly accretes onto the protostar (in other words, $\dot{M}_{disk}$ would increase), producing an energetic outburst. Such energetic outbursts are seen in the FU Orionis stars (e.g. Aspin and Sandell 2001; Reipurth et al. 2002; Peneva et al. 2010), and smaller scale variability is observed for a number of T Tauri stars (e.g. Flaccomio et al. 2010).

Disk (and Envelope) Inner Radius

The disk inner radius, R_{disk}^{min}, has a substantial impact on the SED in the MIR; in the Robitaille et al. (2006) model grid, the inner disk and inner envelope radii were set to be the same. The explanation also follows from optical depth arguments (Equation 2.2); following Hartmann (1998) to illustrate this concept envision a spherically symmetric envelope with no rotation. The density of the infalling envelope can then be described by:

$$\rho(r) \sim \frac{\dot{M}_{env}}{4\pi r^2 v_{esc}} = \frac{\dot{M}_{env}}{4\pi\sqrt{2GM_*}} r^{-3/2} \tag{2.11}$$

This equation is similar to Equation 2.1, but is missing the μ terms which are required when modeling the rotation of the envelope. Assuming that the opacity is the same everywhere in the envelope, integrating over the optical depth (Equation 2.2) and assuming $R^{max} \gg R^{min}$ yields:

$$\tau_\lambda \approx \kappa_\lambda \frac{\dot{M}_{env}}{2\pi\sqrt{2GM_* R^{min}}} \tag{2.12}$$

Taking the Robitaille et al. (2006) model grid 1 μm opacity of 91.7 cm^2 g^{-1}, the optical depth to the inner radius of an envelope surrounding a 0.5 M$_\odot$ protostar with a mass infall rate of 2×10^{-6} M$_\odot$ yr^{-1}, the above equation simplifies to:

$$\tau_\lambda \approx 13.2 \left(\frac{\kappa_\lambda}{91.7 \text{ cm}^2 \text{ g}^{-1}}\right)\left(\frac{\dot{M}_{env}}{2\times10^{-6} \text{ M}_\odot \text{ yr}^{-1}}\right)\left(\frac{M_*}{0.5 \text{ M}_\odot}\right)^{-1/2}\left(\frac{R^{min}}{10 \text{ AU}}\right)^{-1/2} \tag{2.13}$$

The behaviour of τ_λ as a function of R^{min} is shown in Figure 2.6, for these fiducial parameters, at three different wavelengths.

At 1 μm, the envelope is optically thick out to an inner envelope radius of 120 AU ($\tau_{1\ \mu\text{m}} \approx 3.8$); it is clear that NIR photons emitted from the surface of the protostar

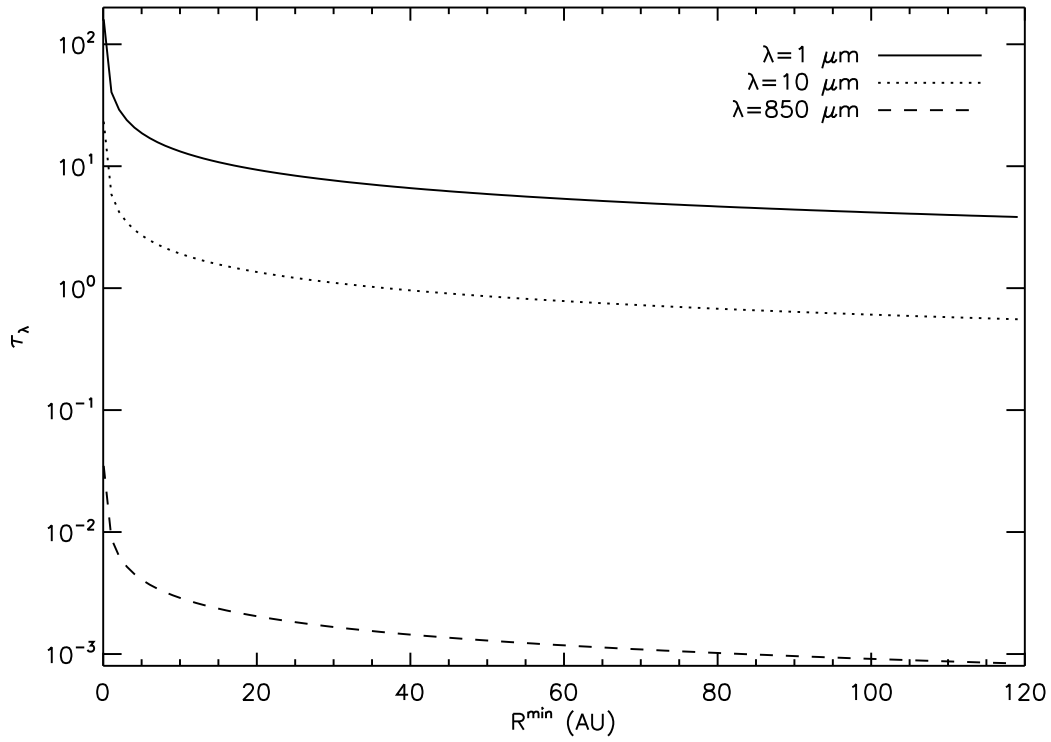

Figure 2.6: The optical depth through an envelope described by Equation 2.11 as a function of the inner envelope radius (Equation 2.13) for the three wavelengths shown. At 850 μm, the envelope is always optically thin, whereas at 1 μm, the envelope is always optically thick.

will be absorbed by the envelope. At a longer wavelength of 10 μm ($\kappa_{10\ \mu\mathrm{m}} \approx 13.3$ cm^2 g^{-1}), the opacity has decreased by a factor of 7, so the optical depth has shifted down accordingly. The optical depth transitions from optically thick ($\tau_\lambda \gg 1$) to optically thin at an inner envelope radius of ≈ 37 AU; photons at 10 μm should have a reasonable chance of escaping through the envelope since the highest regions of optical depth (high density) have been removed. Thus, large inner envelope radii will increase the amount of observable MIR flux. Since the density goes as $r^{-3/2}$, so long as $R^{max} \gg R^{min}$ the mass in the envelope will depend on R^{max}, but the optical depth through the envelope will depend on R^{min}.

It is also worthwhile to show a third curve in Figure 2.6, as an example of the optical depth in the envelope for FIR and sub-mm wavelengths. At 850 μm, the wavelength at which Kirk et al. (2006) made their observations of warm dust in the Perseus molecular cloud, the optical depth stays well below 10^{-2} to a radius of

3.7×10^{-3} AU, less than one solar radius. Considering a 0.5 $M_\odot$ Main Sequence star has a typical radius of 0.63 $R_\odot$ (2.9×10^{-3}), whereas a 0.5 $M_\odot$ Pre-Main-Sequence star could have a radius of 3 $R_\odot$ (0.014 AU), it is safe to assume that at long wavelengths the entire envelope is *optically thin*. This further supports the arguments presented in §2.2.2 regarding the optical depth of the envelope.

In the Robitaille et al. (2006) model grid, the inner disk and envelope radius were set to be the same, unless there was no envelope present surrounding the model. In order to determine the inner disk radius, the Robitaille et al. (2006) model grid first determined the dust sublimation (dust destruction) radius, R_{sub}; the radius at which the temperature is warm enough to vapourize the dust grains. The model grid used a dust sublimation temperature of 1600 K, and calculated R_{sub} using:

$$R_{sub} = R_*(\frac{T_*}{T_{sub}})^{2.1} \tag{2.14}$$

In one-third of the models, the inner disk radius was set to be the dust sublimation radius. The presence of other accreting objects, such as multiple stellar systems or protoplanets, will carve holes into the disk and envelope, inflating the inner disk radius (e.g. Jørgensen et al. 2005, 2008; Artymowicz and Lubow 1994; Mayama et al. 2010). In order to model these larger inner 'holes', the Robitaille et al. (2006) model grid randomly sampled values up to 100 AU for the other two-thirds of the models.

An example of a model with an inner disk and envelope radius larger than R_{sub} is given in Figure 2.7. The cavity opening angle in this model is only 3.2°, yet there is still a significant contribution of scattered emission from 0.3–10 μm (optical to MIR), as shown in Figure 2.7b. It is the emission observed directly from the stellar surface that dominates in the total SED in this wavelength range (Figure 2.7c), however, since the inner envelope and disk radius is 164 R_{sub} ($\approx$ 19.2 AU, almost equivalent to Uranus' orbital radius.) in this model. It is only when the model inclination is 81° that the scattered emission begins to dominate from 0.6–2 μm (while the emission from 2–8 μm is dominated by the direct photons), and by 87° scattering is the only means of escape for photons from 0.6–8 μm. If this model were only observed from 1–10 μm (for example, using the 2MASS JHK$_s$ and the IRAC bands) it would be difficult to differentiate this model from a dust extincted cool stellar photosphere or an RGB star (the protostellar temperature and radius are 3385 K and 4.85 $R_\odot$); only emission in the FIR and sub-mm would be able to determine that this model was a protostar with a significant dust and gas envelope.

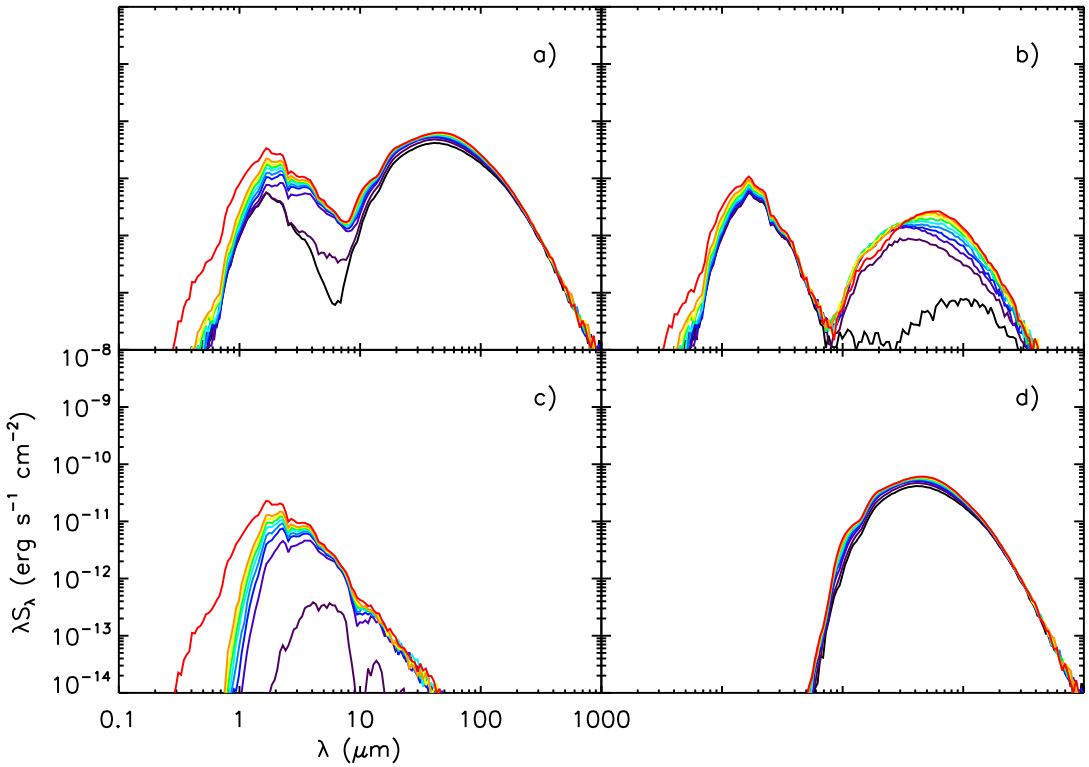

Figure 2.7: The spectra for model 3012074 along 10 different inclinations. The scale and colours are the same as figure 2.1. a) The total SED given by the stellar, disk, and envelope emission; the protostar mass in this model is ≈ 0.31 $M_\odot$. b) The scattered SED. c) The direct SED. d) The thermal SED.

Disk Outer Radius

The outer radius determines the mass and mean density of the disk, whose effect on the SED has been discussed previously. Since the disk volume density, in cylindrical coordinates, goes as $\varpi^{-\beta-1}$ (c.f. Equation 2.7), large disks will be more massive. Larger disks may also have lower densities, and hence lower optical depth, as compared to smaller disks with the same mass, which will also affect the SED. Finally, as the flaring (scale height) of the disk goes as ϖ^{β}, larger disks will experience greater flaring, and hence a greater change in the MIR flux with changing inclination.

Chapter 3

Fitting Models to the Protostars Observed in Perseus

3.1 Observations of Perseus

In the following sections, short descriptions of the data set will be given; for an in-depth discussion the reader is referred to the citations.

IRAC Observations of Perseus

The IRAC instrument on the Spitzer Space Telescope can provide simultaneous observations at four different wavelengths in the MIR, namely at 3.6 μm, 4.5 μm, 5.8 μm, and 8.0 μm, with the 3.6 and 4.5 μm imaging one field and the 5.8 and 8.0 μm imaging a field offset. The IRAC observations of Perseus (Jørgensen et al. 2006) were conducted in two separate epochs in order to eliminate transient objects, and split into a number field tiles in order to incorporate concurrent guaranteed time observations. The total coverage of Perseus was 4.29 deg^2, although only 3.86 deg^2 was overlapped in all four bands, allowing for complete MIR coverage. Data reduction of the IRAC data used the Spitzer pipeline, and then was further augmented by the c2d team to create the final source catalogue.

MIPS Observations of Perseus

The MIPS instrument on the Spitzer Space Telescope can provide observations at 24 μm, 70 μm, and 160 μm. In order to maximize the sky coverage at 70 and 160 μm each field had only one epoch of observations, but two epochs of observation at

24 μm allowed for the removal of transients. Due to instrument limitations, the total MIPS sky coverage of Perseus (Rebull et al. 2007) was about 10.5 deg^2, including the 4.29 deg^2 observed by IRAC. As with IRAC, the standard Spitzer pipeline was applied to the raw images, but the image mosaics at each wavelength was processed differently by c2d in order to produce the source catalogue. Not all of the source detections at 160 μm have corresponding detections at 70 and 24 μm, usually due to saturation in the images.

SCUBA Observations of Perseus

JCMT SCUBA provided observations in the sub-mm at 850 μm, and the resulting dust continuum maps used here are an amalgam of observations taken for Kirk et al. (2006) and JCMT archival data. The archival data set was reduced using the same techniques as the data acquired for Kirk et al. (2006), however different observing configurations were used in each data set. Although the data reduction technique utilized by Kirk et al. (2006) has the advantage of being able to incorporate both the archival data and the new observations, combining both still results in non-uniform noise in the final map. The total coverage of Perseus is approximately 3.5 deg^2, with almost 1.3 deg^2 from observations of Kirk et al. (2006). In order to identify cores within the dataset, the automated algorithm CLUMPFIND 2D (Williams et al. 1994) was used.

3.1.1 Combining the Survey Data

Combining different data sets at different observed wavelengths can be a powerful analytical tool, especially in dense molecular clouds. By utilizing the combined IRAC, MIPS, and SCUBA data provided by the c2d and COMPLETE surveys, Jørgensen et al. (2007) were able to identify 49 deeply embedded protostars within Perseus (A.2). A few of these deeply embedded protostars within Perseus were originally identified by Jørgensen et al. (2006) as having extremely red [3.6]-[4.5] colours and driving strong outflows, an indicator that the sources are young (e.g. Bontemps et al. 1996; Curtis et al. 2010). Interestingly, these objects did not show similarly red [5.8]-[8.0] colours, for which Jørgensen et al. (2006) offered a few possible explanations: deep silicate absorption at 10 μm, large angular momentum cores, larger inner envelope radii, and shocked H_2 emission.

As discussed in §2.2.2, an increase in the envelope density will cause an increase in

optical depth. As the optical depth increases, the silicate absorption feature becomes deeper (Figures 2.1 and 2.5), so the flux at 8 μm decreases. This was the explanation of Allen et al. (2004) for their models with red [3.6]-[4.5] colours but not so red [5.8]-[8.0] colours. Alternatively, if the collapsing protostellar envelope has high angular momentum (or equivalently a high angular rotation rate), then the centrifugal radius of the envelope and disk will be larger. Since the centrifugal radius is roughly where the envelope profile becomes shallow (§2.2.2), the optical depth will decrease, and so more flux at 3.6 and 4.5 μm will escape the envelope; this possibility for red [3.6]-[4.5] colours was also discussed by Allen et al. (2004). A similar effect is produced in low angular momentum envelopes if the inner radius is increased (§2.2.3), and as discussed in Jørgensen et al. (2005) who found that modeling the SED of the Class 0 binary system IRAS 16293-2422 required an extremely large envelope inner radius, which was almost the same size as the centrifugal radius of the system inferred from modeling of CS emission by Zhou (1995). Finally, since these red sources were all associated with outflows, shocked line emission from H_2, which is prominent in the 4.5 μm IRAC band, could produce red [3.6]-[4.5] colours.

In order to follow the analysis of these red sources, Jørgensen et al. (2007) utilized the c2d MIPS data (Rebull et al. 2007) and the COMPLETE SCUBA data (Kirk et al. 2006) to discover additional properties of these deeply embedded protostars. Sources detected at 24 μm with MIPS were associated with significant dust continuum emission at 850 μm, identified within 15″ of the centre of a dust core in the SCUBA map (see figure 2 from Jørgensen et al. 2007). A trend in colour was identified, with most of these sources within 15″ of the centre of a core having [3.6]-[4.5] $\gtrsim$ 1.0 and [8.0]-[24] $\gtrsim$ 4.5, but not necessarily exhibiting red [5.8]-[8.0] colours. Also, most of the cores with associated YSOs at 24 μm had concentrations $\gtrsim$ 0.6:

$$C = 1 - \frac{1.13B^2}{\pi R_{obs}} \frac{S_{850}}{f_o}$$

where B is the beam size, R_{obs} is the observed core radius (Kirk et al. 2006), S_{850} is the total flux from the core at 850 μm, and f_o is the peak flux of the core. In essence, the concentration is a measure of how centrally peaked the protostellar core is (high concentrations may indicate the presence of an embedded protostar warming the inner envelope regions). Since a red [8.0]-[24] colour implies a significant dust envelope and the 850 μm emission showed that the dust envelope extended to large radii, Jørgensen et al. (2007) concluded that these red sources were deeply embedded

within their natal envelopes. The presence of dusty envelopes surrounding these red sources precludes the argument that they could be evolved star+disk (Class II) systems seen edge on (e.g. Robitaille et al. 2006; Jørgensen et al. 2006; Whitney et al. 2003b,a).

Unfortunately, due to source confusion, diffuse emission, saturation, or poor sensitivity in the IRAC, MIPS, and SCUBA maps, Jørgensen et al. (2007) could not use one specific criterion to identify all of the deeply embedded protostars within Perseus. Instead, Jørgensen et al. (2007) developed three criteria that would classify all the deeply embedded protostars in Perseus in a complete and unbiased way, applied it to the protostellar population in Perseus:

- A YSO detected at 24 μm using MIPS with [3.6]-[4.5] > 1 and [8.0]-[24] > 4.5
- *or* A YSO detected at 24 μm within 15$''$ of the nearest core
- *or* A core with a concentration > 0.6

Applying only the first criterion would miss all deeply embedded protostars that may have diffuse emission in the IRAC bands due to shocks or significant extinction from the envelope. Applying only the second criterion would miss all deeply embedded protostars with cores that were too diffuse to be identified by CLUMPFIND, or those whose emission is too weak to be detected by SCUBA. Furthermore, both of the criteria will miss those sources with diffuse emission at 24 μm. Applying only the third criterion will miss protostellar cores with low concentrations or sources with weak dust continuum emission. Thus it is necessary to apply all three criteria in order to ensure that a full and unbiased census of the deeply embedded protostellar population.

The final list of the 49 deeply embedded protostars in Perseus identified by Jørgensen et al. (2007) is given in table 7 of that paper; the source designation, coordinates, and [3.6]-[4.5] and [8.0]-[24] colours are also presented here in table A.2. The list of deeply embedded protostars identified by Jørgensen et al. (2007) in Perseus using their embedded criteria is much larger than the list compiled by Jørgensen et al. (2006) based purely on colour alone, due to the completeness of the above criteria. Furthermore, the sample is now large enough for a statistically significant analysis. Only two sources, L1448-C(S) and L1448-N(B), are not included in the list of deeply embedded protostars since MIPS at 24 μm could not break up the individual sources,

and so the observed flux was attributed to their companions, L1448-C(N) and L1448-N(A).

These criteria could potentially be applied to other star forming regions surveyed by both IRAC and MIPS on Spitzer and SCUBA on the JCMT. This has already been done in the Ophiuchus star forming region (Jørgensen et al. 2008), allowing for comparisons between the deeply embedded stellar formation stage in both Ophiuchus and Perseus. Jørgensen et al. (2008) also modified the embedded YSO criteria discussed above, by re-evaluating the ability of the concentration to discern pre- and proto-stellar cores. By including sources detected by MIPS in either the 24 μm or 70 μm band when applying the first two criteria, Jørgensen et al. (2008) removed the need to use the core concentration as an embedded source identifier. For example, the four sources in the list of embedded protostars in Perseus identified using only the core concentration, IRAS 03255+3103, NGC 1333-IRAS 2A, NGC 1333-SVS 12, and NGC 1333-SVS 13, are detected at 70 μm (table A.5) and are within 15$''$ of the nearest core identified at 850 μm.

3.2 What is Kicking at the Darkness?: The Role of Cavities in Protostellar Formation

Now that a population of deeply embedded protostars has been identified in Perseus, they can be used to answer a number of questions related to the process of star formation. A number of such questions were dealt with in Jørgensen et al. (2007) and Jørgensen et al. (2008), but the more fundamental question that this thesis hopes to answer is: How are these deeply embedded protostars exhibiting detectable emission in the MIR? Specifically, what physical mechanism at work in the deeply embedded stage of formation of a star is allowing the short wavelength photons to escape? Although part of the answer can easily be prescribed to the incredible sensitivity of Spitzer over the previous space and ground based infrared telescopes, it still requires a theoretical approach to complete the puzzle, combined with a statistically significant number of observations on which the theory can be tested.

Despite the exhaustive theoretical background given in §2, the solution can be approximated as an optical depth problem. Given that both theory and observations point to a radial density distribution in the protostellar envelope and core on large scales, clearly the inner regions of the envelope, where the density is high, must be

at least partially removed in order for the MIR photons to escape. One possibility, discussed in §2.2.2, is that the jets and outflows launched due to the formation of the protostar and disk clear bipolar cavities through which the short wavelength (namely λ = 1–10 μm) emission can escape if the outflow is inclined to the line of sight with the observer (Whitney et al. 2003b,a, 2004). At inclinations where the outflow is not inclined to the line of sight of the observer, scattering of photons off of the cavity walls can still provide a significant amount of flux at between 1–10 μm (§2.2.2). The other possibility, discussed in §2.2.3 is that spherical cavities are formed within the inner envelope due to the formation of stellar multiples or planetary systems (Artymowicz and Lubow 1994; Zhou 1995; Guilloteau et al. 1999; Mayama et al. 2010), removing the highest density regions of the envelope and allowing the photons to escape through the reduced optical depth (Jørgensen et al. 2005, 2008). Combining the large sample of embedded protostars with the wide range of parameter space explored by the Robitaille et al. (2006) model grid, a clearer picture of the role of cavities in stellar formation may be found.

If the sample of deeply embedded protostars in Perseus were smaller, it would be beneficial to model each source individually rather than fit to a grid. Since each parameter in the radiative transfer code of Whitney et al. (2003b) affects the resulting SED in various ways, different combinations of parameters can produce similar SEDs, leading to a degeneracy in parameter space. Given enough observations using various methods across different wavelengths, these degeneracies could be broken [for example, when modeling IRAS 16293-2422 Jørgensen et al. (2005) found that they could differentiate between the two cavity scenarios based on mm interferometry]. Given that there is a complete and unbiased list of 49 embedded protostars in Perseus, acquiring and compiling all the required data, and then modeling each source individually, would take an extreme amount of time. Instead, such a large population can be studied faster and more efficiently by analysing the distribution of best fits to each source *as an ensemble*, in other words, how do the best fits to each source describe the sample of embedded protostars as a whole? Even though degeneracies may arise, building a statistical description will sufficiently narrow the parameter space enough to make robust statements regarding the embedded phase of protostellar formation. To that end, the first step is to describe how a source is fit to the model grid.

3.2.1 Fitting to the Radiative Transfer Grid

The radiative transfer model grid of Robitaille et al. (2006) utilizes a custom built fitting tool described in Robitaille et al. (2007), who hosted it online[1]. Given a set of observed fluxes at various wavelengths using various telescopes, the fitting tool first convolves the model fluxes with the appropriate spectral response function (loosely, the sensitivity of a telescope to radiation of a given wavelength) of the detector used to obtain the photometry. Since the radiative transfer grid allowed for the model fluxes to be integrated through various physical radii, when given a distance range and aperture radius from the observations the fitting tool can match the model to the appropriate physical scale and distance. This is important since the same source may exhibit varying fluxes at the same wavelength when observed on different scales; for example, models with cavities will exhibit more scattered flux on large scales because of the larger scattering surface and decreasing envelope density with radius.

The fitting tool also allows for varying A_V, the amount of dust extinction *apart from the extinction due to the protostellar core*, within a user specified range, using an extinction law fit to the Galactic ISM. The goodness-of-fit between the model and the observations is given by the reduced χ^2; the fitting tool can either use uncertainties derived from the photometry, or a user specified percentage value. The fitting tool can also incorporate upper limits, in conjunction with a confidence level on the upper limit; a 100% confidence limit excludes all models with convolved and extincted fluxes greater than the upper limit, whereas a 90% applies a χ^2 penalty. The result is a list of the 10000 best fit models to each source, ranked by χ^2, out of the 200000 models available (the fitting tool differentiates between the 10 inclinations of each model), along with the best fit A_V and distance to the source, log(d).

For each source, all available fluxes regardless of their signal-to-noise value (as measured by the c2d team) were used for fitting to the Robitaille et al. (2006) model grid. This was done in order to ensure that each source had the widest spectral coverage possible, an essential condition for getting accurate model fits. The exception to this was in instances where the IRAC or MIPS fluxes were bandfilled (c2d Delivery Document); if a source was identified in some but not all of the Spitzer bands, then apertures were drawn at the position of the source and integrated in those other bands. These fluxes can be untrustworthy, especially in crowded regions where contamination of the bandfilled flux can occur. Also, the 4.5 μm and 850 μm fluxes were not used

[1] http://caravan.astro.wisc.edu/protostars/

when fitting to the Robitaille et al. (2006) model grid (see below). The fluxes used as inputs for the Robitaille et al. (2007) SED fitting tool are given in Tables A.3, A.4, and A.5. In each of those tables, a column called *flag* designates whether the flux should be ignored (0), fit (1), or treated as an upper limit (3); if a flux is flagged 0 but a value is nonetheless given, then that signifies a bandfilled flux measurement. Only one Perseus source, associated with HH 211-FIR, was not fit to the Robitaille et al. (2006) model grid as only two fluxes were available from the combined 2MASS, c2d, and COMPLETE catalogs.

As input for the SED fitting tool, the distance range was taken to be 200–300 pc, in order to incorporate the uncertainty in the distance to Perseus. Although throughout this thesis it is assumed Perseus is at a set distance of 250 ± 50 pc, adopting such a large range of values will not significantly affect the results as it can only introduce a factor $(\frac{300}{200})^2 = 2.25$ of uncertainty into the distance scaling for each model. This uncertainty might influence the resulting fit, but it will affect all the resulting parameters equally, so no model inconsistencies should arise. Furthermore, this uncertainty is applied equally to all fits to a given source.

The extinction was allowed to range between 0–10 mag, in accordance with the extinction maps for Perseus (Ridge et al. 2006; Kirk et al. 2006). Apertures of 5″ were used for 2MASS JHK$_s$, 3″ for the IRAC bands, 6″ for the MIPS bands, and 15″ for the SCUBA fluxes. Though the model fluxes do change with physical aperture scale, this is only evident when comparing between two very different size scales. Furthermore, if the observed apertures correspond to physical scales larger than the radius of a model envelope, the fluxes should be the same regardless, as the ambient cloud density used in the Robitaille et al. (2006) grid is very low.

It should be noted that when fitting the sample of 48 deeply embedded protostars in Perseus using the Robitaille et al. (2007) tool, the best fit model to a given source was taken to be the one which possessed the lowest χ^2 value compared to the other models fit to that source:

$$\chi'^2_{best} = \mathrm{MIN}[\chi^2_n] \tag{3.1}$$

where the subscript n represents the nth radiative transfer model fit from the Robitaille et al. (2006) grid. The 48 best fit models exhibited a spread in χ'^2_{best} over four orders of magnitude; the best fit model to B1-c had the highest χ'^2_{best} at 152 whereas the best fit model to IC 348-MMS had the lowest χ'^2_{best} at 0.006. This is not surprising, since there is no consistent set of fluxes available for all of the sources: IC 348-MMS

has measurements at 5.8 μm, 24 μm, 70 μm, and 850 μm, while B1-c has detections in all of the IRAC and MIPS bands plus SCUBA. This introduces bias into the reduced χ^2 when comparing between different sources; for B1-c the best fit model simultaneously overestimates the MIPS fluxes and underestimates the IRAC fluxes while still providing an acceptable fit. A better fit with much lower χ'^2_{best} (≈ 0.01) to B1-c can be found using the online version of the Robitaille et al. (2007) SED fitting tool, using the same ranges in A_V and distance but omitting the 3.6 μm, 4.5 μm, 8.0 μm, and 850 μm fluxes. Although this bias makes it extremely difficult to judge which source was better fit to the model grid, the χ^2 values can still be used to differentiate between models *fit to each source*. This provides the motivation for the χ^2 criterion that will be developed at the end of this chapter: rather than applying a universal χ^2 value to reject Robitaille et al. (2006) models fit to each source, the model with the best fit χ^2 for a given source is used to judge all other fits to that source.

An example of the best fifteen fits to the source NGC 1333-IRAS 4B is shown in Figure 3.1. The model with the best fit χ^2 is shown by the solid black line and the next fourteen 'runner-up' fits are shown by the grey dotted lines. The values for the best fit χ^2, A_V, distance, model, and inclination are given in the box. The luminosity of 0.16 $L_\odot$ is computed from a simple numerical integral over the observed fluxes and assuming a distance of 250 pc to Perseus. The uncertainties on the flux measurements are represented by error bars, but are rather small compared to the scale on the plot. For NGC 1333-IRAS 4B, only the four IRAC bands, MIPS 24 μm, and SCUBA 850 μm fluxes are available. It should be noted that while the fitting tool interpolates the fluxes between the physical aperture radii, the SEDs reproduced below are for one set aperture radius (2763 AU or 11$''$ at a distance of 250 pc).

For the 15 best fit models shown here in Figure 3.1, it is obvious that a tight is fit is found between 3.6–24 μm, suggesting a similar type of model geometry, but not necessarily a complete symmetry in model parameters. Without a second flux measurement in the FIR, such as MIPS 70, it is difficult for the fitting tool to narrow down the envelope accretion rate and the total luminosity of the system. A quick check of the distributions for the 10000 best model fits shows an order of magnitude range in L_{tot} and a few orders of magnitude range in $\dot{M}_{env}$. There is also a significant variation in the model fluxes near 1 μm, due to the lack of 2MASS observations for this source. The 2MASS observations are sensitive to parameters such as the cavity opening angle, so without those observations it is also hard for the Robitaille et al.

(2007) SED fitting tool to sufficiently narrow the parameter space.

The IRAC 4.5 μm and SCUBA 850 μm flux measurements are both plotted as

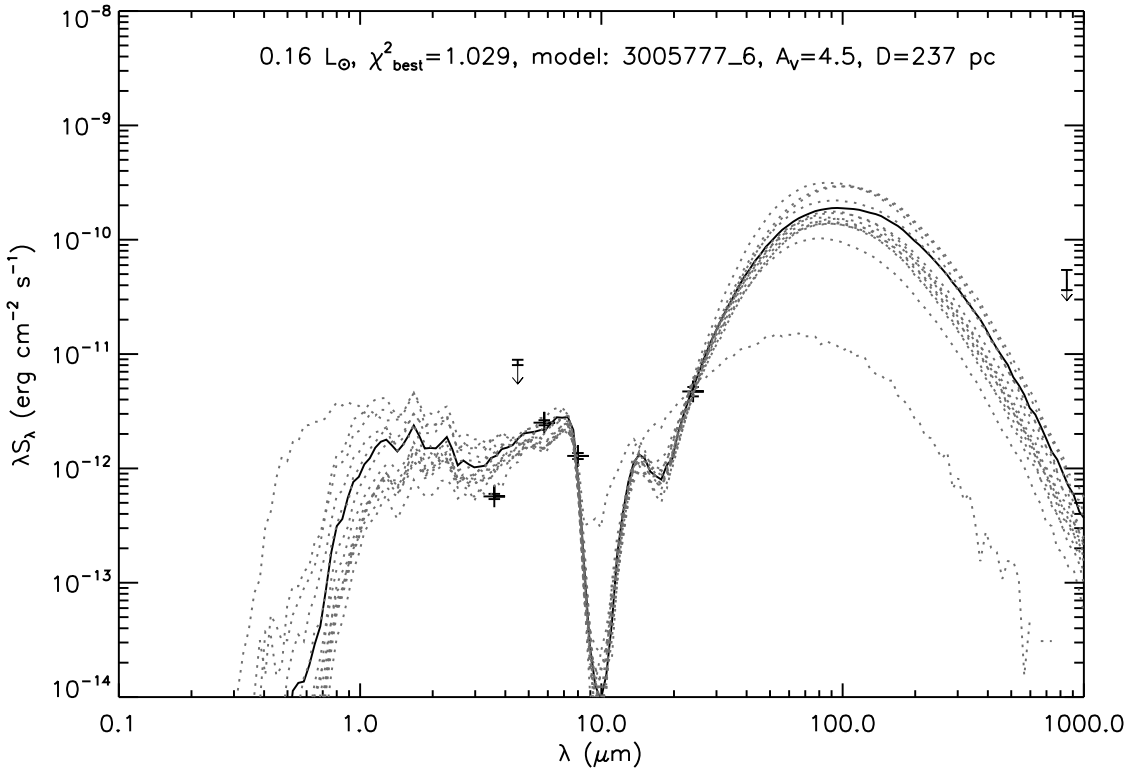

Figure 3.1: The fifteen best fit models in χ^2 to the source NGC 1333-IRAS 4B. The best fit model in χ^2 is shown as the solid black line, and the value of χ^2, A_V, distance, and the model are given in the box. The dotted gray lines are the 14 best 'runner-up' fits to the source. The nomenclature for the models is 30*****_*, where the value after the underscore gives the model inclination (1=87°, 2=81°, 3=...).

upper limits. Clearly, the 4.5 μm flux is not well fit by any of the models, which might be due to shocked H_2 line emission contaminating the IRAC measurement. As shock emission was not included in the radiative transfer models, the 4.5 μm fluxes were not included in the model fitting in order to remove any bias. Since for most sources a detection in at 4.5 μm was accompanied by a detection at either 3.6 μm or 5.8 μm, the Robitaille et al. (2007) fitting tool was still able to narrow the best fit model fluxes between 1–10 μm. This was not always the case, as for some sources the models fit by the Robitaille et al. (2007) SED fitting tool over-predicted the observed 4.5 μm flux, which is why the 4.5 μm observations were not used as strict upper limits.

The discrepancy between the 850 μm flux predicted by the models and observed by SCUBA is especially pronounced, and is caused by a difference in model opacity values and the definition of the envelope outer radius. As noted in §2.2.2, the model envelope radii were determined approximately by the radius at which the radiative equilibrium temperature dropped to 30 K. This temperature is a factor of 2–3 times higher than the mean temperatures observed for cores in Perseus (Johnstone et al. 2006; Rosolowsky et al. 2008), so the model envelope radii is 6–12 times smaller than the observed core radii. Indeed, the average core radius found by Kirk et al. (2006) was approximately 31″, or 7750 AU at a distance of 250 pc, whereas the model envelope radii were almost always near the lower limit of 1000 AU taken by the Robitaille et al. (2006) grid.

Furthermore, the sub-mm opacity values used in the models are based on ISM dust rather than coagulating dust in dense clouds. In the models of Ossenkopf and Henning (1994), this results in upward of a factor of 4 difference between opacity values at 850 μm. For example, Kirk et al. (2006) used a value of 0.02 cm^2 g^{-1} for the opacity at 850 μm, and many other authors have adopted a value between 0.01 cm^2 g^{-1} and 0.02 cm^2 g^{-1} (e.g. Johnstone et al. 2000; Andrews and Williams 2005; Johnstone et al. 2006; Simpson et al. 2008; Curtis et al. 2010; Sadavoy et al. 2010). The Robitaille et al. (2006) model grid adopted the opacity law given by the solid line in Figure 3.2, which yields a factor of 0.0037 cm^2 g^{-1} at 850 μm. For reference, the Ossenkopf and Henning (1994) coagulation results are plotted in Figure 3.2, for dust grains at a density of 10^5 cm^{-3} with varying ice mantle thickness, as well a simple power law fit from (Hartmann 1998).

If the envelope dust opacity in the FIR and sub-mm can be modeled by a power law of the form (Hartmann 1998):

$$\kappa_{\lambda_o}(\frac{\lambda}{\lambda_o})^{-\beta}$$

what varies is the characteristics of the dust grains themselves, and hence the normalization value of κ_{λ_o}. The size, shape, chemical composition, and ice mantle thickness all affect the opacity of the particular dust grain (e.g. Ossenkopf and Henning 1994). In the optically thin limit of dust continuum emission (§2.2.2), Equation 2.6 related the opacity at a given wavelength to the mass of the emitting dust and gas, so in the models, which have a fixed density profile and radius (and hence a fixed envelope mass), the observed flux will be lower than what is observed. The problem is that

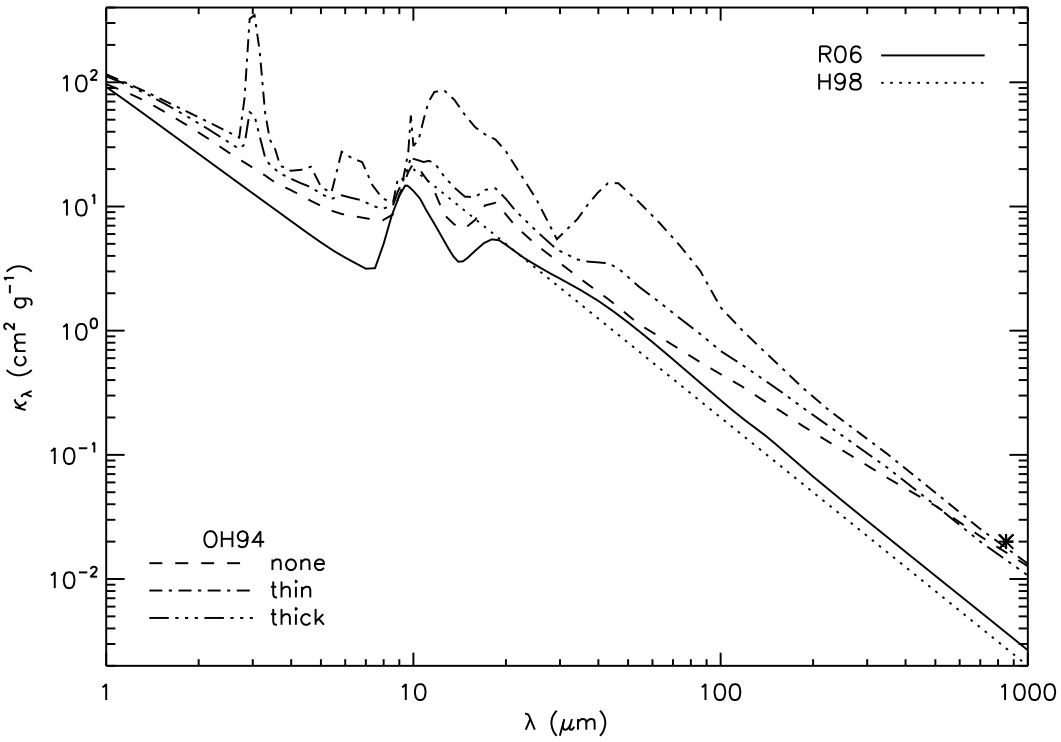

Figure 3.2: The opacity profile assumed for the dust in the envelope and disk (except for the cold disk midplane) as a solid line. A power law fit to the extinction, assuming κ_{λ_o} = 0.2 cm^2 g^{-1}, λ_o = 100 μm, and β = -2 (Hartmann 1998), is shown as the dotted line. The opacity laws from Ossenkopf and Henning (1994) at a density of 10^5 particles cm^{-3} and assuming no (dashed), thin (dot-dash), and thick (triple-dot-dash) ice mantles are also shown. The star is the value of 0.02 cm^2 g^{-1} adopted by Kirk et al. (2006).

the FIR and sub-mm fluxes in the model cannot simply be scaled up (or conversely, the observed fluxes scaled down) to produce a good fit. A change in the opacity profile would require the radiative transfer models to be re-run, as the temperature distribution in the envelope would change considerably. This is evident in Figure 3.1, since simply scaling the SED cannot fit both the sub-mm flux and the IRAC and MIPS fluxes; the envelope emission would need to increase substantially, and the peak would have to shift to longer wavelengths, in order to fit the 850 μm datapoint.

This presents a problem, in that the sub-mm flux was used to not only identify deeply embedded protostars, but is a measure of the total envelope mass and size, which help determine the envelope infall rate. It also prevents the SED fitter from

producing best fit disk-only models with heavy extinction to get red colours, especially in the absence of a detection at 24 μm. In order to incorporate the SCUBA 850 μm flux with the 2MASS, IRAC, and MIPS fluxes in a physically motivated way, a simple 1-dimensional analytic model of the dust continuum flux must be applied to the observed SED.

3.3 Simple Analytic Models of the Dust Continuum

Given a well sampled SED and some analytic models for the density and temperature of the envelope, a simple 1D model of the dust continuum flux as a function of the outer envelope radius can be constructed. Granted, the 2MASS, IRAC, MIPS, and SCUBA data only sparsely samples the SED, nevertheless they still provide enough spectral coverage for these simple models to work. In the following sections, the simple model will be constructed, and demonstrated that it works on both the Robitaille et al. (2006) model grid and on the observed cores in Perseus. Finally, it will be used to provide a goodness-of-fit measurement that allows spurious models fit by the grid to the Perseus sources to be removed based on their ability to 'match' the sub-mm flux.

3.3.1 Constructing the Model

Following Hartmann (1998), assume we are given an SED of a protostar in λF_λ, complete enough that the peak in the FIR due to the envelope emission is well established. The wavelength at which the dusty envelope emission peaks is denoted λ_m. If radiative equilibrium is achieved at all points in the envelope, then we can approximate the envelope SED as that of a dusty blackbody, in other words the blackbody flux is modulated by the opacity of the emitting medium (a popular term used in astronomy is a greybody). We can then relate the wavelength at which the flux from the dusty envelope peaks to a 'photospheric' temperature of the envelope via Wien's law (Hartmann 1998). In order to simplify the determination of the peak wavelength, we can to first order assume that the greybody acts like a true blackbody, which yields the following solution:

$$T_{phot} \approx \frac{3700\ \mu\text{m K}}{\lambda_m} \tag{3.2}$$

where the numerical factor comes from solving for the peak of λB_λ, rather than B_λ. Note that Equation 3.2 is fully consistent with the more oft used form of Wien's Law, and is accurate to within a few percent of the more formal solution for the peak in the greybody function.

In using Wien's law, we are saying that the envelope can be thought of as a stellar photosphere, with the emission coming from an optical depth $\tau_{\lambda_m} \sim 2/3$. If λ_m can be reliably determined from examination of the observed SED, Equation 3.2 can be used to estimate the envelope photosphere temperature. Since the envelope can be approximated as a blackbody, the Stefan-Boltzmann law also holds:

$$R_{phot} = \sqrt{\frac{L_{tot}}{4\pi\sigma T_{phot}^4}} \tag{3.3}$$

The total luminosity of the protostar is calculated by numerically integrating over the set of fluxes and assuming a distance to Perseus of 250 pc:

$$L_{tot} = 4\pi d^2 \int F_\lambda d\lambda = 4\pi d^2 \int \lambda F_\lambda d\ln(\lambda) \tag{3.4}$$

On large scales, the envelope density is given by the free-fall solution with no rotation, Equation 2.11. Since this profile should hold everywhere, the density profile can be simplified even further:

$$\rho(r) \approx \rho_o (\frac{r}{R_{phot}})^{-3/2} \tag{3.5}$$

where ρ_o is the density of the envelope at the radius R_{phot}. Unfortunately, ρ_o is unknown, but it can be solved for using the optical depth equation (2.2):

$$\begin{aligned} \tau_{\lambda_p} &= -\int_{R_{max}}^{R_{phot}} \kappa_{\lambda_p} \rho(r) dr \approx 2/3 \\ \rho_o &= [3\kappa_{\lambda_p} R_{phot}(1 - \sqrt{\frac{R_{phot}}{R_{max}}})]^{-1/2} \end{aligned} \tag{3.6}$$

This gives us ρ_o as a function of outer envelope radius. We can then estimate the total envelope mass by integrating over the density in Equation 3.5:

$$\begin{aligned} M_{env} &\approx \int_{R_{phot}}^{R_{max}} \rho(r) 4\pi r^2 dr \\ &\approx \frac{8\pi}{3} \rho_o R_{phot}^3 [(\frac{R_{max}}{R_{phot}})^{3/2} - 1] \end{aligned} \tag{3.7}$$

In the optically thin regime, the envelope mass can be determined from the dust continuum emission at 850 μm via (Hildebrand 1983; Johnstone et al. 2000; Kirk et al. 2006):

$$\begin{aligned} M_{env} &= 0.23 S_{850} (e^{17\ \mathrm{K}/\langle T \rangle} - 1)(\frac{\kappa_{850}}{0.02\ \mathrm{cm^2\ g^{-1}}})^{-1}(\frac{d}{250\ \mathrm{pc^2}})^2 \\ S_{850} &= 4.35 M_{env} (e^{17\ \mathrm{K}/\langle T \rangle} - 1)^{-1}(\frac{\kappa_{850}}{0.02\ \mathrm{cm^2\ g^{-1}}})(\frac{d}{250\ \mathrm{pc^2}})^{-2} \end{aligned} \tag{3.8}$$

where S_{850} is the flux in Jy at 850 μm.

We can calculate the mass-weighted mean temperature, $\langle T \rangle$, by assuming a power law form for the temperature as a function of radius (i.e. $T \propto r^{\gamma}$). Since a power law dependence is an acceptable proxy for the full calculation (see Figure 3.3), we can use Equation 2.3 since it should apply for an optically thin medium in radiative equilibrium. We must make one slight change, however, to ensure that this simple 1D model fits well. From Equation 2.3, it is clear that the radiative equilibrium temperature would decrease exponentially to zero, but this is not the case for cores in Perseus. Rosolowsky et al. (2008) derived a mean kinetic gas temperature of T_{kin} = 11 K in Perseus, establishing a firm lower limit to the core temperature assuming the gas and dust are thermodynamically coupled. This minimum temperature can be thought of as the heating of the core by the interstellar radiation field (certainly, the temperature cannot fall lower than the cosmic microwave background temperature of 3 K), which is not included in the Robitaille et al. (2006) model grid. Thus, the temperature profile can be modeled as:

$$\begin{aligned} T(r) = T_{phot}(\frac{2r}{R_{phot}})^{-2/5} \quad &, \quad r < R_{kin} \\ T(r) = T_{kin} \quad &, \quad r \geq R_{kin} \end{aligned} \tag{3.9}$$

Where R_{kin} is the radius at which the heating of the envelope from the formation protostar is balanced by the heating from the interstellar radiation field. The radial temperature profile used here is in good agreement with the temperature profile derived from the radiative transfer grid, an example of which is shown in Figure 3.3. This temperature profile has been averaged in the polar direction (inclination), and power laws of the form $T \propto r^{\gamma}$, broken at R_{phot} (vertical dot-dash line), have been fitted to the profile. Whereas a temperature profile with γ = -1/2 is too steep for $r > R_{phot}$, a profile of γ= -2/5 is a much better fit. We now find $\langle T \rangle$ for $r<R_{kin}$:

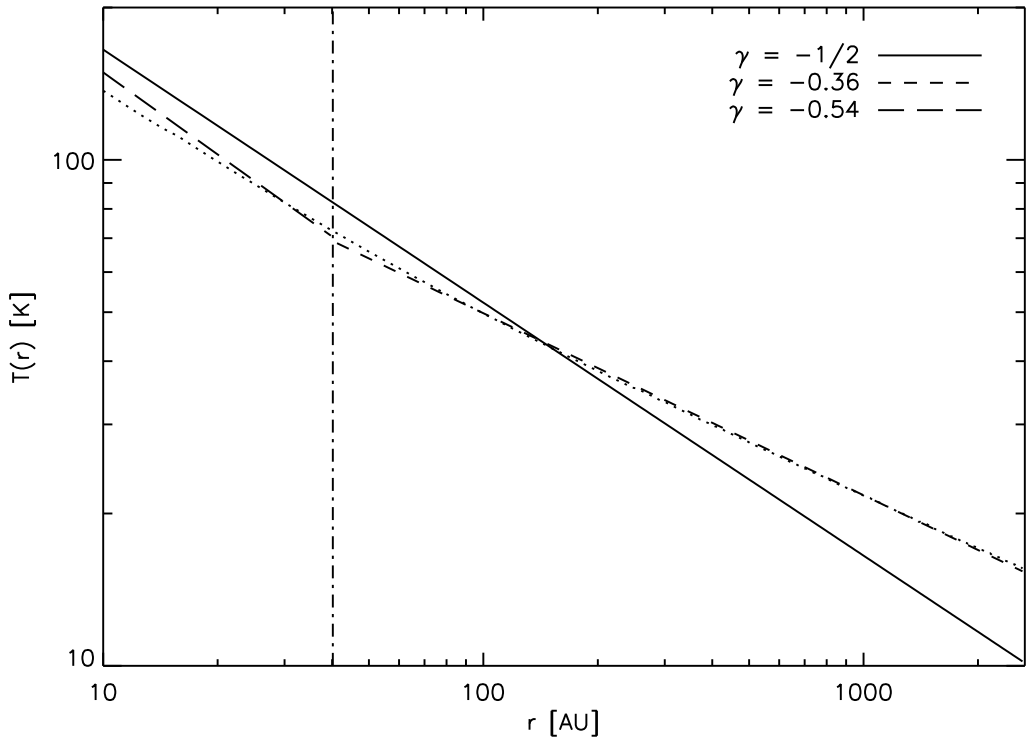

Figure 3.3: The polar averaged temperature profile for model 3000340 (T. Robitaille, private communication). The dotted line corresponds to the temperature profile calculated from the radiative transfer models, while the long dash and short dash lines are single exponent power law fits to the temperature profile for r $<$ R_{phot} and r $\geq$ R_{phot}, respectively. Using a radial exponent of -1/2 (solid line) in would produce a temperature profile that falls off too quickly. The radial exponent calculated for r $\geq$ R_{phot} is quite close to the exponent used in Equation 3.9.

$$\begin{aligned} \langle T \rangle &= \frac{\int T(m) dm}{\int dm} \\ &\approx \frac{\int_{R_{phot}}^{R_{max}} T(r) \rho(r) 4\pi r^2 dr}{\int_{R_{phot}}^{R_{max}} \rho(r) 4\pi r^2 dr} \\ &\approx \frac{30}{22}(2)^{-2/5} T_{phot} \frac{[(R_{max}/R_{phot})^{11/10} - 1]}{[(R_{max}/R_{phot})^{3/2} - 1]} \end{aligned} \tag{3.10}$$

and for r≥R_{kin}:

$$\begin{aligned}
\langle T \rangle &= \frac{\int T(m)dm}{\int dm} \\
&\approx \frac{\int_{R_{phot}}^{R_{kin}} T(r)\rho(r)4\pi r^2 dr + \int_{R_{kin}}^{R_{max}} T(r)\rho(r)4\pi r^2 dr}{\int_{R_{phot}}^{R_{max}} \rho(r)4\pi r^2 dr} \\
&\approx \frac{\langle T \rangle_{in} + T_{kin}(R_{max}^{3/2} - R_{kin}^{3/2})}{R_{max}^{3/2} - R_{phot}^{3/2}}, \\
\langle T \rangle_{in} &= \frac{30}{22}(2)^{-2/5} T_{phot} R_{phot}^{3/2} [(R_{kin}/R_{phot})^{11/10} - 1]
\end{aligned} \tag{3.11}$$

There is no discontinuity between (3.10) and (3.11) at the boundary R_{kin}; for r≥R_{kin}, the temperature profile asymptotes to a constant value. It should be noted that using 15 K instead of 11 K as the background core temperature (Kirk et al. 2006) changes the result by only a factor of 1.75; in other words, given an observed 850 μm flux, Equation 3.8 would predict an envelope mass 1.75× lower if a temperature of 15 K was used.

In order to fit this analytic model to the observations, we only need the observed flux at 850 μm and effective radius of the core; agreement between the predicted flux at 850 μm with the observed value yields the envelope maximum radius R^{max}, and subsequently the envelope mass and temperature.

3.3.2 Demonstration of the 1D Models: Modeling Models and Observations

In the following the applicability of this simple 1D model is demonstrated by fitting first to the fully numerical radiative transfer grid of Robitaille et al. (2006), and then to the sample of deeply embedded protostars in Perseus. Once verified, these 1D models can be used as a quality cut for the SED fitting tool (Robitaille et al. 2007), to cull those models in the grid that would not reproduce the observed 850 μm flux for each source.

1D Modeling of 2D Models

The 1D model described above should make a reasonable fit to the full 2D radiative transfer models, as long as the approximations that went into the 1D model are still

a realistic simplified description of the envelope SED. To that end, a subset of models from the grid were chosen using the following requirements:

- outflow cavity opening angles between 1° and 2°, the smallest allowed in the model grid
- protostellar masses less than 5 $M_\odot$ (spectral type B7), similar to most massive protostars in Perseus

There are 65 models in the grid that fit the above criteria. The 1D model fit to each 2D model for each of the 10 inclinations; since only those with the smallest cavity opening angles were chosen (the smallest opening angle was 1°), the requirement of the 1D model that the envelopes are spherically symmetric still holds. In order to keep the 1D model as close to the 2D model as possible, the assumed model flux distance of 1 kpc (Robitaille et al. 2006) and the model opacity at 850 μm of 0.0037 cm^2 g^{-1} were used in Equation 3.8.

The resulting 1D model fit to the 2D model 3000340 at a 70° inclination is shown in Figure 3.4. Here the density at R_{phot} (ρ_o), total integrated envelope mass (M_{env}), mass-weighted mean temperature ($\langle T \rangle$), and predicted 850 μm dust continuum flux (S_{850}) are all plotted as a function of the outer envelope radius. At an inclination of 70°, the 2D model predicts 6.49 mJy at a distance of 1 kpc, which is represented by the horizontal dashed line in the S_{850} plot in Figure 3.4. It intersects the 1D model predicted flux (solid line) at a radius of 2705.19 AU, quite close to the 'true' 2D model envelope radius shown as the vertical dotted line, R_{env}^{max} = 2655.90 AU (difference of 49.29 AU, or 2%).

Given the predicted envelope radius of 2705.19 AU, the 1D model would predict a mass-weighted mean temperature in the envelope of 15.7 K; in this model, the radius at which the envelope temperature profile would fall to 11 K is 3082.97 AU. The 1D model would predict an envelope mass of 0.25 $M_\odot$, only a factor of 1.8 larger than the 2D model value of 0.16 $M_\odot$(the toy model neglects rotation and the mass removed in the cavities, so it always slightly over predicts the mass). Finally, the 1D model would predict a density of 3.01×10^8 particles cm^{-3} at the photometric radius of the 2D model envelope (R_{phot} = 40.19 AU), whereas the 2D solution (evaluating Equation 3.5 at R_{phot}) yields a density of approximately 2.72×10^8 particles cm^{-3}.

Similar results were found for all of the 65 models, indicating that the 1D model is a good proxy for more thorough 2D radiative transfer modeling if the approximations used to develop the toy model are realistic and applicable to observed cores.

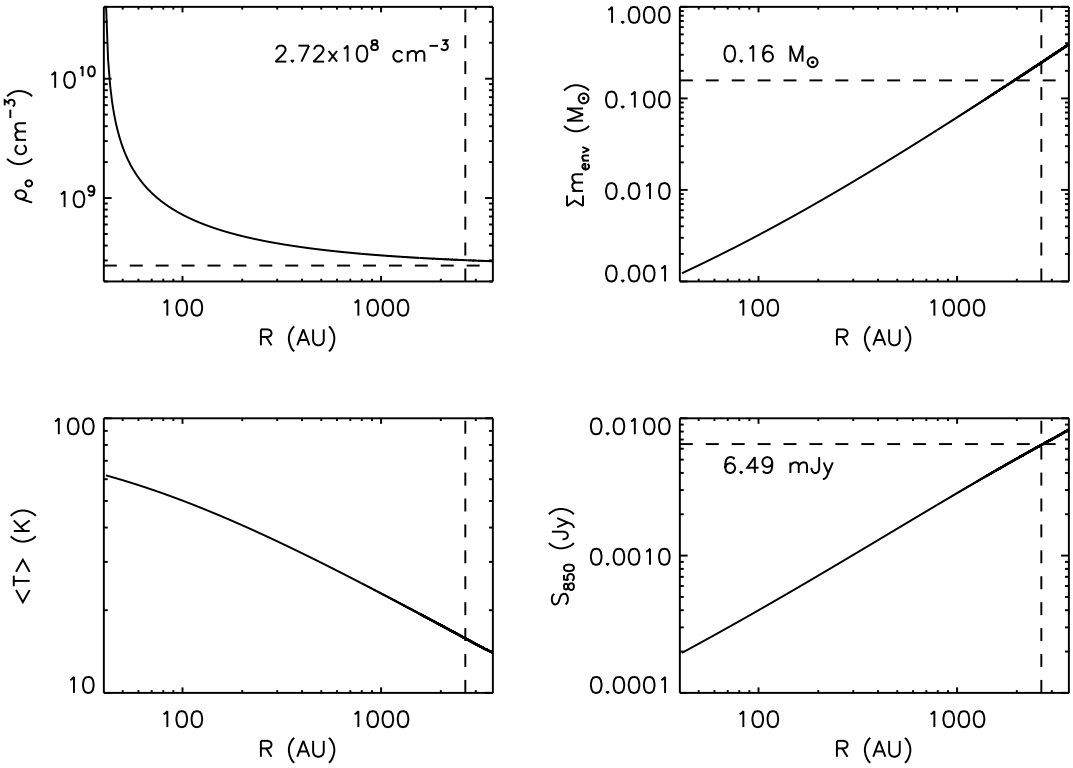

Figure 3.4: The resulting 1D model to the 2D model 3000340 at 70° inclination. Clockwise from top left: the density at R_{phot} in particles cm^{-3} as a function of outer envelope radius; the total envelope mass as a function of outer envelope radius; the predicted flux at 850 μm as a function of outer envelope radius; the mass-weighted mean envelope temperature as a function of outer envelope radius. The vertical dashed line is the 2D model envelope radius, and the horizontal dashed lines correspond to the 2D model values (see text) given in each plot.

Despite this conclusion, it should be noted that had the 850 μm opacity been taken as 0.02 cm^2 g^{-1} instead of the value the Robitaille et al. (2006) model grid used, the 1D model would not have agreed well with the observed core mass and radius. The implication is that fitting to FIR and sub-mm fluxes is influenced by the opacity in that wavelength range. For example, Zavagno et al. (2010) found excellent fits to their sources using the Robitaille et al. (2007) SED fitter, but Elia et al. (2010) found that one of their sources was better fit by a greybody ($F_\lambda \propto \kappa_\lambda B_\lambda$, which is Equation 3.8 at 850 μm). The greybody fit required a temperature of approximately 10.5 K, similar to the temperature derived from Rosolowsky et al. (2008). Since the Robitaille et al. (2006) model grid only extended their envelopes to a temperature

of $\sim$ 30 K and neglected external heating, the Robitaille et al. (2007) SED fitting tool cannot reliably fit to such cold dust cores. Similarly, Forbrich et al. (2010) used the Robitaille et al. (2007) fitting tool to YSO sources in IC 348 and NGC 2264, and also found that the best fit SEDs in some cases could not properly reproduce the FIR and sub-mm emission (see their figure 10, 11, 12, and 13). Sewiło et al. (2010) also used the Robitaille et al. (2007) SED fitting tool on combined Herschel, Spitzer, and 2MASS data, and found that including external heating, emission from polycyclic aromatic hydrocarbons, and larger envelope radii produced a model that fit the observed data extremely well. They also found that these additions to the model did not affect the values for parameters such as the mass infall rate.

Note also that the significant variance of sub-mm fluxes with inclination in the Robitaille et al. (2006) model grid also presents a challenge, since the derived parameters in the 1D model are independent of inclination. An example has been given in Figure 2.1, where about an order of magnitude difference in sub-mm flux with inclination is seen in the SED. This is due to the way the radiative transfer code of Whitney et al. (2003b) treats the model photons when producing the SED (T. Robitaille, private communication) If observed sub-mm fluxes with very small uncertainties are available, the tendency for the model sub-mm flux to vary with inclination may ignore the same model at different inclinations, thereby biasing the resultant distribution of inclination angle for a source. Since the sub-mm fluxes are primarily due to thermal radiation from warm, optically thin dust, there should be no variation with inclination so long as the density profile remains the same. For these reasons, the 850 μm flux was not used in the Robitaille et al. (2007) SED fitting tool.

1D Modeling of The Perseus Protostars

The applicability of the 1D collapsed model to the embedded protostars in Perseus will now be demonstrated, using two sources. Note that when fitting to the models, κ_{850} was taken to be 0.02 cm^2 g^{-1}, and the distance to the Perseus was assumed to be 250 pc, for Equation 3.8. The first is L1448-IRS 2, whose SED is shown in Figure 3.5; the resulting 1D model fit is shown in Figure 3.6, with only a few cosmetic differences between it and Figure 3.4. Instead of plotting the density at R_{phot} as a function of outer envelope radius, it is instead plotted at a radius of 100 AU from the protostar, in order to facilitate comparisons between solutions to the embedded protostars. The total integrated luminosity of L1448-IRS 2 is 2.88 $L_\odot$, shown above the M_{env} plot,

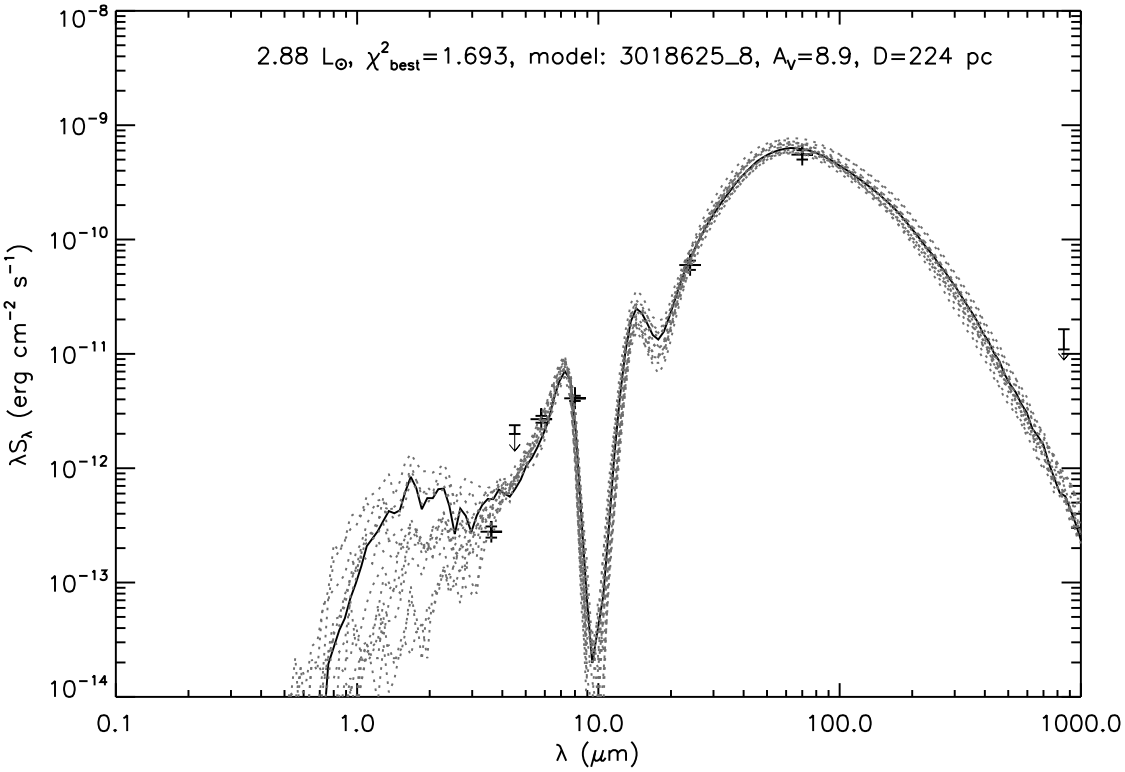

Figure 3.5: The fifteen best fit models in χ^2 to the source L1448-IRS 2.

and the solution to the 1D collapsed model radius is approximately 6479.4 AU, shown above the plot of S_{850}, and represented in the four plots by the vertical dashed blue lines. Kirk et al. (2006) measured a total flux of 3.88 Jy for this core, represented by the horizontal dotted blue line in the S_{850} plot, which they converted to a mass of 2.2 $M_\odot$, represented by the horizontal dotted green line in the plot of M_{env}. Given the effective core radius, as measured by Kirk et al. (2006), to be 33″ (8250 AU at a distance of 250 pc), the 1D model for the size and mass of the core differs from the observed values by factors of 1.27 and 1.29, and combined are well within the uncertainty introduced by assuming a temperature floor of 11 K as opposed to 15 K.

In contrast, the 1D model does an extremely poor job of fitting to the source NGC 1333-IRAS 4B, shown in Figure 3.7. Neither the predicted envelope radius nor the envelope mass are well constrained by the model, and require an envelope size much larger than the upper limit of 40000 AU, approximately four times the largest observed core radius. The reason for the huge discrepancy is the fact that the total integrated luminosity of NGC 1333-IRAS 4B is very low (see Figure 3.1), and so the

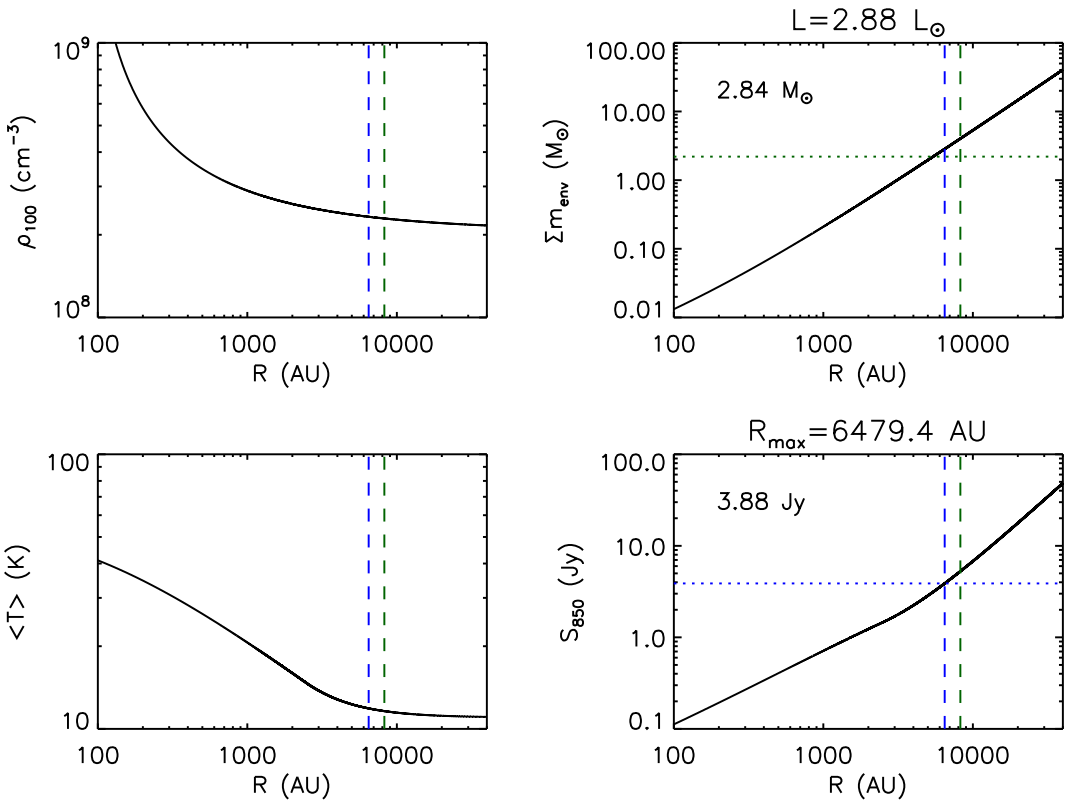

Figure 3.6: The result of fitting the 1D collapsed model to the embedded protostar L1448-IRS 2. The set of plots are the same as in Figure 3.4, with a couple of minor changes. First, the density plot is of ρ_{100}, the density at 100 AU from the protostar. The vertical dashed blue line corresponds to the solution of the 1D collapsed model, whose value is given above the S_{850} plot, whereas the vertical green dashed line is the effective radius of the core from Kirk et al. (2006) assuming a distance of 250 pc. The horizontal dotted blue line in the S_{850} plot is the core flux at 850 μm from Kirk et al. (2006), and the horizontal dotted green line in the plot of M_{env} is the corresponding core mass from Kirk et al. (2006). The value shown in the M_{env} plot is the predicted envelope mass from the solution to the 1D collapsed model, and the value above the plot is the integrated luminosity of the source assuming a distance of 250 pc.

temperature profile is always too cool to produce the amount of flux needed to better match the observations. The low integrated luminosity is due to the lack of a flux measurement at 70 μm (Figure 3.1); since most of the flux from an embedded YSO is emitted in the FIR and sub-mm, without the MIPS measurement at 70 μm the integrated luminosity is only a lower limit. Thus, the photospheric radius of the 1D model for NGC 1333-IRAS 4B is only 2.26 AU, the temperature profile falls to 11 K at a radius of 981 AU, and so the value of ρ_o, and consequently the predicted

envelope mass, are also very low. The observed mass and radius for the core of NGC 1333-IRAS 4B was 7.1 $M_{\odot}$ and 46″ (11500 AU at 250 pc).

Clearly, the weakest link in the chain of approximations in the analytic toy model

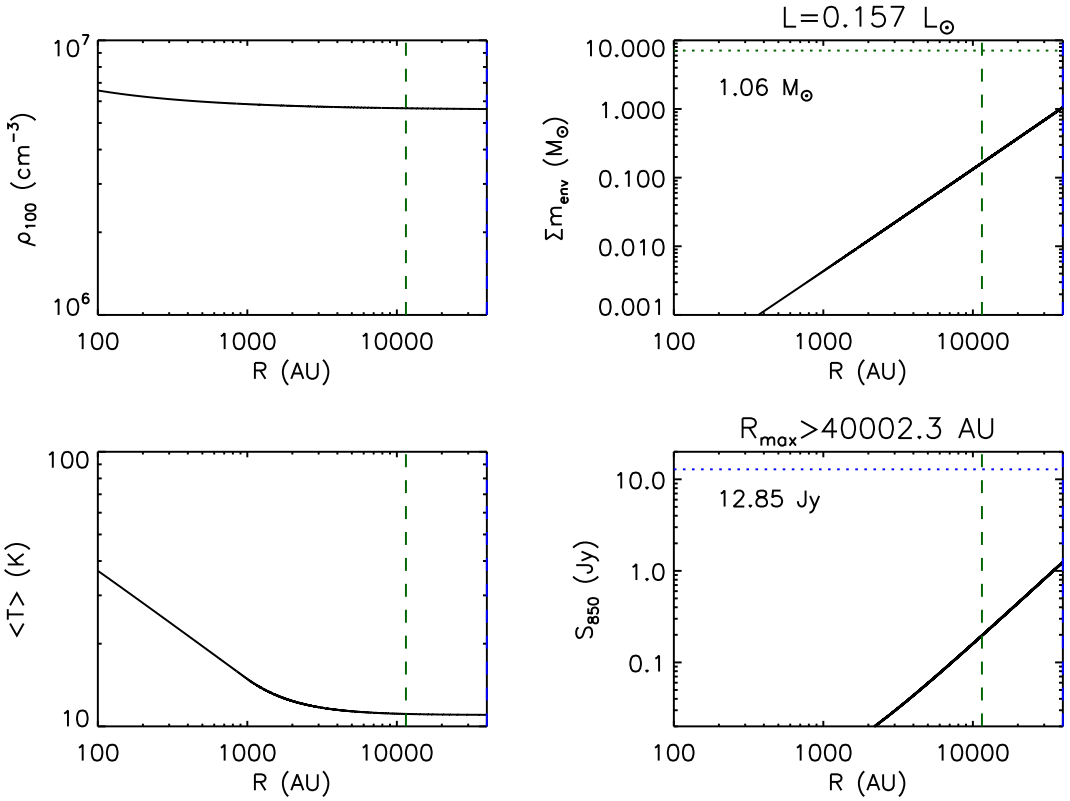

Figure 3.7: The result of fitting the 1D collapsed model to the embedded protostar NGC 1333-IRAS 4B. The set of plots are the same as in Figure 3.6.

is the assumption of good spectral coverage of the SED, especially in the FIR, which will influence how accurate the estimate of L_{tot} is. When this is the case, such as fitting to the 2D Robitaille et al. (2006) model grid and L1448-IRS 2, the simple toy model can predict the amount of 850 μm dust continuum flux rather well. It can now be transformed in a straightforward way to a quality cut to cull those models fit by the Robitaille et al. (2007) SED fitting tool that would not be able to match the observed amount of 850 μm flux.

3.3.3 Applying the 1D Model as a Quality Cut

As mentioned previously, the Robitaille et al. (2007) SED fitting tool can have trouble fitting the Robitaille et al. (2006) model grid to both MIR and sub-mm data simulta-

neously, especially for low luminosity sources. Simply using a χ^2 goodness-of-fit test would be able to only cull models that reproduce the observed 2MASS, IRAC, and MIPS fluxes relatively well, but would not be able to decide which models were also a good fit to the dust continuum flux. In order to incorporate the 850 μm fluxes and pick out the most likely physically motivated models, elements of the toy model can be re-worked into an effective quality cut.

For a given source, the Robitaille et al. (2007) SED fitting tool will return the (default setting) 10000 best fit models, with the source distance and extinction as free parameters, ranked by χ^2. Comparing equations 2.11 and 3.5, the product of ρ_o and R_{phot} is given by:

$$n_o = \rho_o R_{phot}^{3/2} = \frac{\dot{M}_{env}}{4\pi\sqrt{2GM_*}} \tag{3.12}$$

For each model fit to the source the values for $\dot{M}_{env}$ and M_* can be used to find n_o. Since the value for the cavity opening angle, θ_{cav}, can now take on a range of values, the envelope density must be modified for the removal of the mass. Assuming a conical shape for the outflow (this only introduces a slight difference in the mass calculation instead of assuming the cavity walls are curved as in the Robitaille et al. 2006 grid), the integral over the polar angle becomes $4\pi\cos(\theta_{cav})$, and the total mass in the model envelope becomes:

$$M_{env} = \frac{8\pi}{3}\cos(\theta_{cav}) n_o (\sqrt[3]{R_{env}^{max}} - \sqrt[3]{R_{env}^{min}}) \tag{3.13}$$

If R_{env}^{max} is taken to be the radius of the observed core at 250 pc, and R_{env}^{min} is the model inner envelope radius, then assuming a temperature of 11 K and a distance of 250 pc, Equation 3.8 reduces to:

$$S_{850} = \frac{M_{env}}{0.23(e^{17/11} - 1)}$$

Thus, the envelope density profile is extended to the radius of the observed dust core, and given a mean core temperature of 11 K (Rosolowsky et al. 2008), which allows the prediction of the flux the model would theoretically emit. The predicted flux can then be compared to the observed flux, and a given model can be accepted or rejected based on how well it fits.

When this quality cut is used in conjunction with a χ^2 cut, the 10000 best model fits to a given source can be culled to a much smaller number that satisfy *all* of the

available data.

The Quality Cuts

In order to apply the quality cut, we first reject all model fits to a source that cannot predict an amount of 850 μm flux within a factor of four of the observed value are rejected, regardless of their χ^2 value. The factor of four was chosen based on the three most significant uncertainties in the quality cut: the uncertainty in the assumed temperature, the uncertainty introduced by the large range in available source distances, and the uncertainty in the value of the opacity at 850 μm. As stated previously, using a temperature of 15 K over 11 K introduces a factor of 1.75 difference in the conversion from 850 μm flux to dust mass. Similarly, allowing the Robitaille et al. (2007) SED fitting tool to range from 200–300 pc instead of a much smaller range about 250 pc introduces a further factor of 2.25 uncertainty in the best fit distance. Finally, there is a factor of two uncertainty in the dust opacity at 850 μm (Ossenkopf and Henning 1994). Although the assumed dust temperature and distance are different, the same dust opacity is assumed both here and in (Kirk et al. 2006), removing the need to incorporate the associated uncertainty into the quality cut (although it still introduces an inherent uncertainty in the derived properties from the SED fitting, and so cannot be completely ignored). Thus, a factor of four difference between the predicted and observed fluxes is consistent with the assumed uncertainty in the method itself.

In order to further cull models with poor fits, a cut based on the χ^2 is performed:

$$\frac{\chi^2 - \chi^2_{best}}{\chi^2_{best}} < 3$$

In other words, only models with $\chi^2 < 4\chi^2_{best}$ are accepted. Note that here the χ^2_{best} refers to the model with the lowest χ^2 *after* the 850 μm flux quality cut has been applied (in other words, χ^2_{best} here may be greater than χ'^2_{best} from Equation 3.1). Since the quality cut essentially fits a given model to the 850 μm flux, the χ^2 value for that model should be the same as if the Robitaille et al. (2007) SED fitter were able to fit all the fluxes simultaneously. It has been verified that tightening the strengths of these quality cuts does not change the overall results of the thesis, merely the number of fits to each source.

Chapter 4

Results

4.1 Descriptions of the Plots

In order to study the culled sample of model fits to each embedded source satisfying the 850 μm flux and χ^2 criteria, these 'quality' fits were binned in parameter space, and the fraction of fits in each bin from each source was summed to generate an ensemble histogram. In other words, the value in a given bin in an ensemble plot therefore represents the *fraction* of fits to *all* of the sources *in that range*. The parameters used for the ensemble plots are given in table A.6, along with the Robitaille et al. (2006) range for those parameters, the range used for the histograms, and whether the parameter was binned linearly or logarithmically. The binning ranges for each parameter were chosen based on values that would be expected in a low to intermediate mass star forming region such as Perseus. These parameters were chosen because they were either directly connected to the ideas put forth in §3.2 as possible explanations for the reddening of the sources (outflow cavity opening angle, inner disk and envelope radius, inclination), or because they influence the observed YSO SED.

For those parameters which were binned logarithmically, the logarithmic width of the bin is given. There are three histograms for each parameter plot; the dotted green line is the distribution of models from the Robitaille et al. (2006) grid (the area under the curve is normalised to one), the red dashed line is the input distribution of all quality fits (those that survived the 850 μm flux cut and the χ^2_{best} cut) to the forty-eight embedded protostars, and the blue solid line is the distribution of the quality fits to the 'red' sources. The 'red' sources are defined as those that satisfied the [3.6]-

[4.5] and [8.0]-[24] colour criterion of Jørgensen et al. (2007), as opposed to embedded sources identified by the other two criteria. If any quality fits lay outside the binning range, they were summed together, and are represented by the thick vertical lines at the upper and lower bounds, in the same style and colour as the histogram to which it belongs.

This analysis was also applied to each individual source (in other words, binning the Robitaille et al. (2006) model grid fits that satisfy the quality cuts for each source individually). Most sources show distributions in parameter space consistent with the ensemble distributions, although there are some exceptions. For example, NGC 1333-SVS 13 has for most of its quality fits Robitaille et al. (2006) models with $L_{tot} \geq$ 10 $L_{\odot}$, and a peak at $\sim$ 30 $L_{\odot}$. The main focus of this thesis will be, however, on the distribution of all fits to the 48 deeply embedded protostars in Perseus that could be fit by the Robitaille et al. (2007) SED fitting tool. The analysis will then apply to the whole population, in a statistically significant manner; individual distributions will only be discussed as needed.

4.2 Total Luminosity

The histogram of L_{tot}, total luminosity, is shown in Figure 4.1. The model grid (green line) is evenly sampled within the histogram range, suggesting the quality fits to the luminosity are not biased due to the model grid. A two-sided Kolmogorov-Smirnov test was performed between the two quality fit distributions and the Robitaille et al. (2006) grid, with both distributions having a 0.02% chance of being randomly drawn from the grid distribution. Most of the fits in both the full distribution and the red source distribution have values of L_{tot} between 0.3 $L_{\odot}$ and 3 $L_{\odot}$. This range of luminosities is perhaps unsurprising, given the relatively low stellar masses observed in Perseus.

It is important to note whether the high total luminosities imply a significant contribution from accretion. A 0.5 $M_{\odot}$ Main-Sequence star (spectral type M0) has a stellar luminosity of 0.077 $L_{\odot}$, a radius of 0.63 $R_{\odot}$, and an effective temperature of 3840 K (Carroll and Ostlie 2006), but a similar mass Pre-Main-Sequence star can have a radius of 3 $R_{\odot}$ and a temperature of 3750 K in the model grid, yielding a stellar luminosity of 1.6 $L_{\odot}$ from the Stefan-Boltzmann law. On the other hand, for a protostar with mass 0.5 $M_{\odot}$, the model grid sampled radii between $\approx$ 0.8–6.6 $R_{\odot}$, and temperatures between $\approx$ 3680–3800 K. Since the protostar is expected to contract as

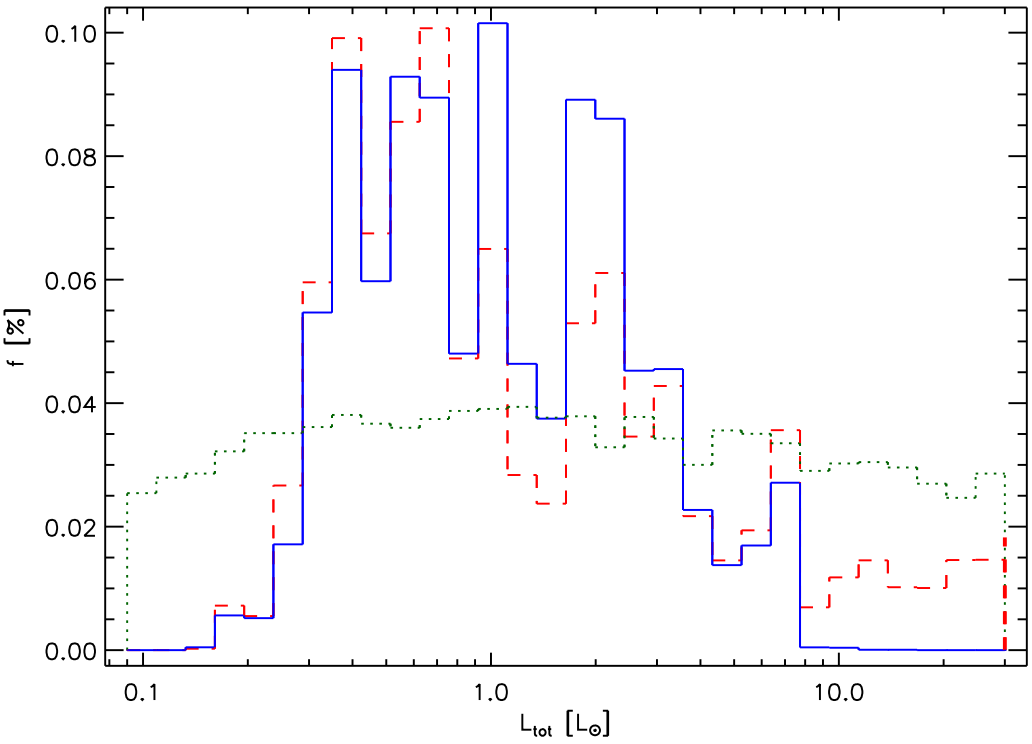

Figure 4.1: The histogram of L_{tot} for all fits that satisfied the 850 μm flux and χ^2_{best} criteria. The green dotted line is the normalised distribution (see text) of the Robitaille et al. (2006) model grid, the red dashed line is the distribution of all the quality fits for all the embedded sources, and the blue solid line is the distribution of the quality fits for only the red sources.

it ages, the youngest protostars will have the largest radii and coolest temperatures. In this case, a 0.5 $M_\odot$ protostar with a radius of 6.6 $R_\odot$ and a temperature of 3680 K will have a stellar luminosity of 7.2 $L_\odot$, which would be consistent with the histogram without the need for accretion to contribute.

4.3 Protostellar Mass

The distribution of protostellar masses is plotted in Figure 4.2, along with the IMFs given by Salpeter (1955) (dash-dot line), Miller and Scalo (1979) (triple-dot-dash line), and Kroupa (2001) (long-dash line). Both the full source distribution and the red source distribution resemble the stellar IMF ($\frac{d\xi(M_*)}{dM_*} \propto M_*^{-\alpha}$), despite the relatively flat

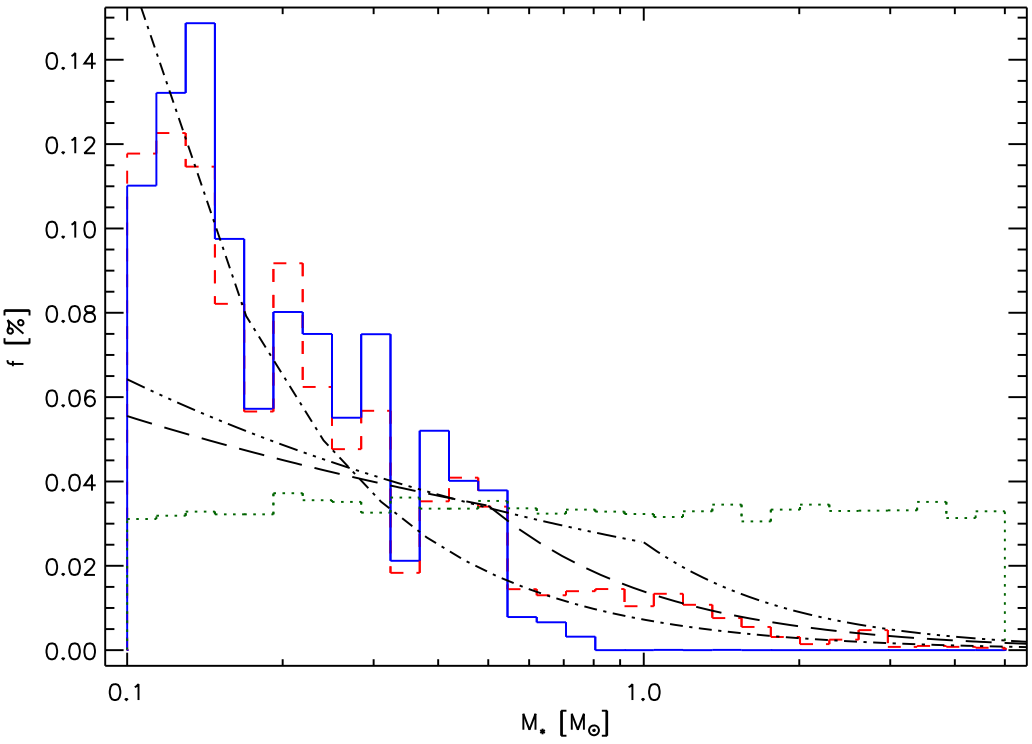

Figure 4.2: The histogram of M_* for all fits that satisfied the 850 μm flux and χ^2_{best} criteria. The Salpeter (1955) (dash-dot), Miller and Scalo (1979) (dash-triple-dot), and Kroupa (2001) (long-dash) IMFs have been plotted as a consistency check against the protostellar mass distributions.

sampling in this mass range for the Robitaille et al. (2006) model grid; the resulting KS tests reveal that both distributions have less than 0.01% probability that they could be randomly drawn from the Robitaille et al. (2006) grid. The resemblance of the M_* distribution to the IMFs suggests that these deeply embedded protostars are a homogenous sub-sample of the general YSO population in Perseus, with a distribution of masses consistent with what would be expected in a star forming region. In other words, fitting the Robitaille et al. (2006) model grid to the deeply embedded protostars in Perseus does not require a specific stellar mass, suggesting that these protostars are very likely in an early phase in the star formation process. As the Robitaille et al. (2006) model grid did not extend the protostellar masses lower than 0.1 $M_\odot$, there is no real way to hypothesize what the distribution would be in the brown dwarf mass regime.

The ratio of protostellar mass to the core mass from Kirk et al. (2006) is plotted

in Figure 4.3, to demonstrate that there is no strong correlation with the observed core mass, and hence the 850 μm flux, with protostellar mass from the quality fits. Both distributions are relatively flat in the 0.012–0.2 range, with a slight increase to ratios of 0.06-0.15 observed more strikingly in the distribution of all the sources. The core masses used are derived from Equation 3.8 using $\langle T \rangle$ of 11 K, so they are a factor of 1.75 larger than the core masses given in Kirk et al. (2006).

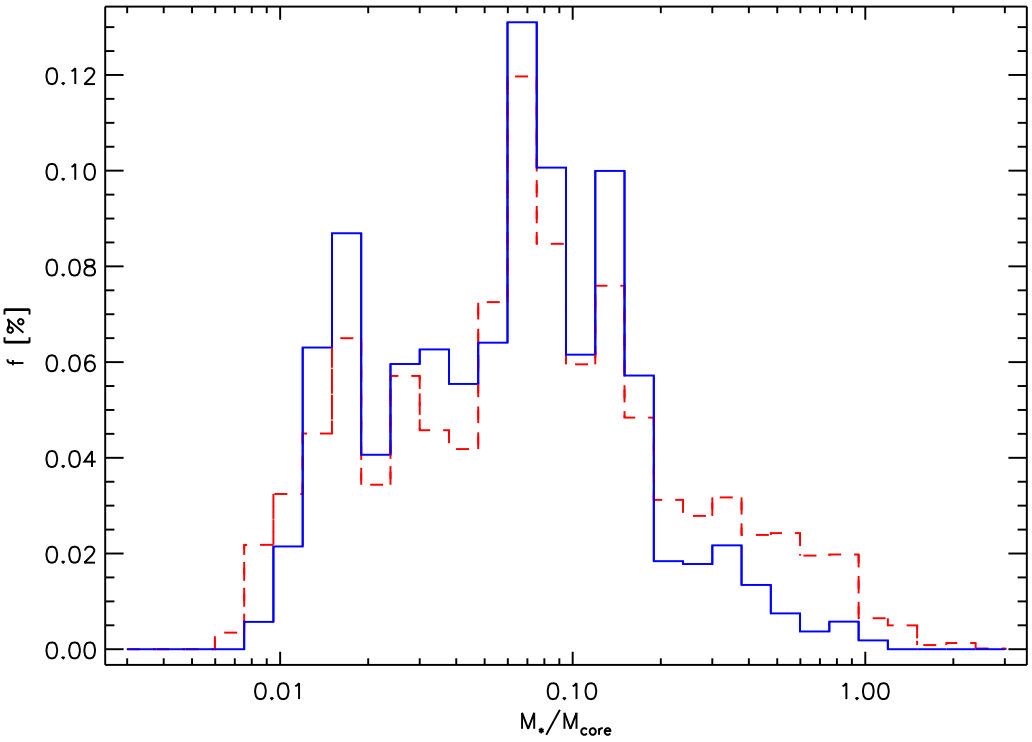

Figure 4.3: The distribution of the protostellar to core mass ratios for the quality fits to the deeply embedded protostars. The relatively flat distribution between 0.012 and 0.2 argues that the protostellar mass is not influenced by the observed core mass, and thus the 850 μm flux.

4.4 Disk Mass

The disk mass distributions look like they may be influenced by the Robitaille et al. (2006) model grid, but the steep drop at 1.2×10^{-5} $M_\odot$ and at 1.5×10^{-2} $M_\odot$ suggest otherwise. The KS test produced a 34% probability that the distribution for the full

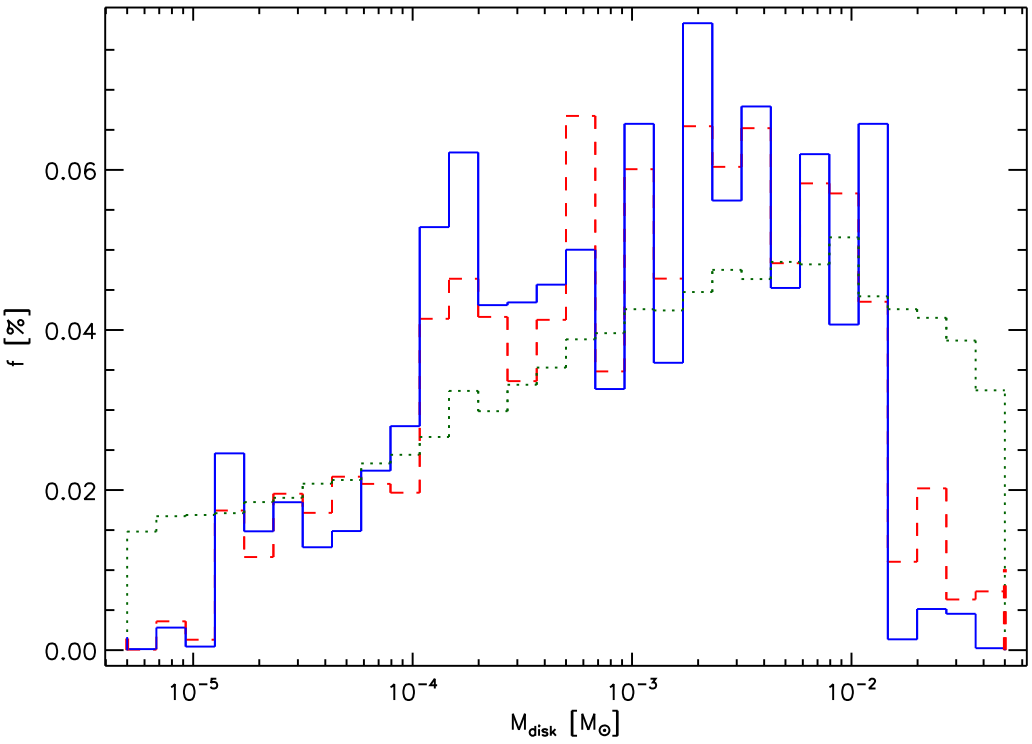

Figure 4.4: The distribution of disk masses in the quality fits. Both the distribution for all the sources and for only the red sources follow the same profile as the Robitaille et al. (2006) model grid, and span several orders of magnitude.

sources could be randomly sampled from the model grid distribution, though for just the red sources the probability dropped to 11%. The distribution looks to have a relatively broad and flat peak from 10^{-4}–10^{-2} $M_{\odot}$, consistent with observed estimates of disk masses in Class II protostars in both Ophiuchus and Perseus (Andrews and Williams 2005, 2007), but lacking in massive disks. The distribution does not seem to change very much (94% probability both distributions are the same) when only the red sources are binned, which indicates that the mass of the disk is not important in influencing the IRAC+MIPS colours. Furthermore, the presence of such a flat peak indicates that the value of M_{disk} cannot be constrained based on the available fluxes, or conversely the disk mass does not influence the SED considerably.

Jørgensen et al. (2009) estimated M_{disk} for four of the sources in the Perseus sample from PROSAC observations: L1448-C(N) (their L1448-mm), NGC 1333-IRAS 2A, NGC 1333-IRAS 4A (their NGC 1333-IRAS 4A-SE), and NGC 1333-IRAS 4B.

The derived masses for these four sources are 0.044 $M_\odot$, 0.056 $M_\odot$, 0.46 $M_\odot$, and 0.24 $M_\odot$ respectively. The observed masses for L1448-C(N) and for NGC 1333-IRAS 2A are consistent with the distribution of fits for the disk mass, but for NGC 1333-IRAS 4A and NGC 1333-IRAS 4B the masses derived from the PROSAC data are at the upper range of the distributions. As with the ensemble distribution of M_{disk}, the distribution of fits for these four sources showed a considerable range in possible values, which stands out especially from the L_{tot} and M_* distributions which span less than two orders of magnitude. This indicates that the model grid cannot provide good constraints on the disk masses for any of the sources, especially when coupled with the fact that there is no apparent change when only the red embedded sources are plotted.

Similar behaviour is evident in the other disk parameter distributions, with possible values spanning several orders of magnitude, and no significant difference between the distribution of all the embedded sources in Perseus and for just the red sources. The most likely explanation is that various combinations of these three parameters in the Robitaille et al. (2006) produce similar SEDs, and the available data does not provide enough information to break the degeneracies. Furthermore, the lack of massive disks is unsurprising given the way the Robitaille et al. (2006) model grid sampled M_{disk} and M_*. Within the range of 0.1–1 $M_\odot$ in protostellar mass, the Robitaille et al. (2006) model grid sampled up to $M_{disk} \approx 0.13\ M_*$, as shown in Figure 4.5. The points show the grid parameter space for M_* and M_{disk}, and the dashed line represents an upper limit of 13%.

4.5 Envelope Infall Rate

The envelope infall rate shows a flat peak from about 7–41$\times10^{-6}$ $M_\odot$ yr^{-1}, much larger than the typical estimate of 2$\times10^{-6}$ $M_\odot$ yr^{-1} for a 10 K singular isothermal sphere (Shu 1977). Since accretion from the envelope is not included as a source of radiation in the Whitney et al. (2003b) radiative transfer code, the $\dot{M}_{env}$ parameter in the Robitaille et al. (2006) grid is used to set the infalling envelope density (Equation 2.1). The relatively steep fall off towards 10^{-4} $M_\odot$ yr^{-1} and 10^{-6} $M_\odot$ yr^{-1} reflect this, as high accretion rates imply a lack of MIR flux escaping whereas low accretion rates would not produce such red IRAC+MIPS colours. The similarity between the distribution of $\dot{M}_{env}$ for the red sources and for the full list of embedded sources (KS probability of 54%) supports the argument that these sources are deeply embedded

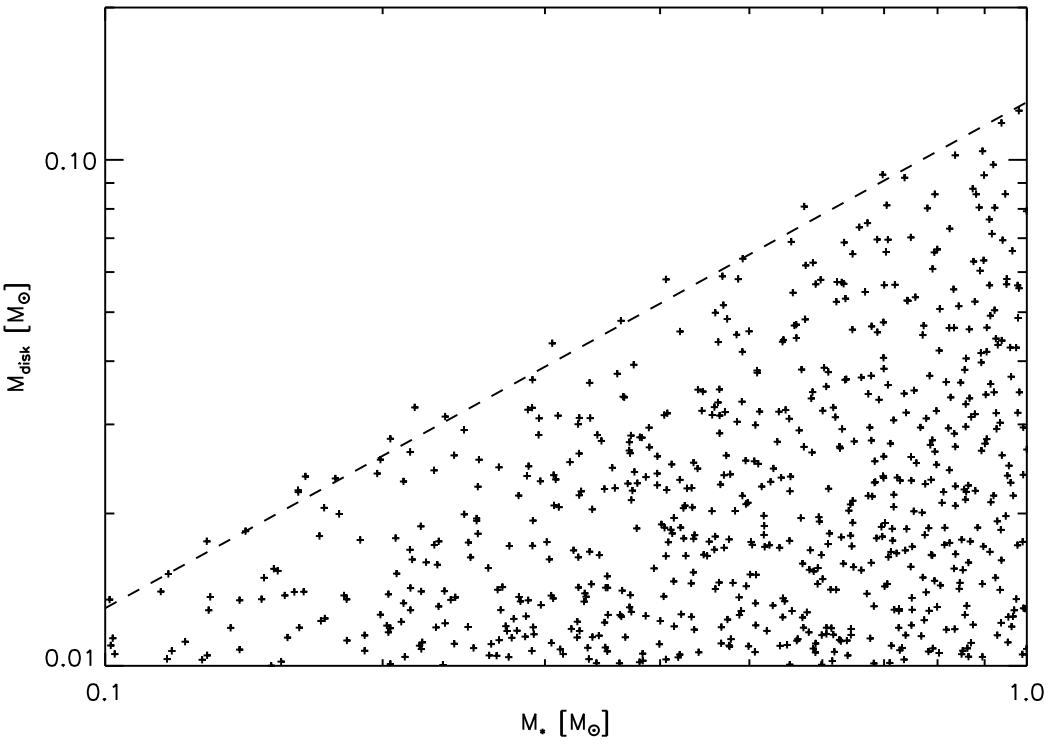

Figure 4.5: The Robitaille et al. (2006) model grid parameter space for M_{disk} and M_*. The dashed line represents $M_{disk} = 0.13\ M_*$, under which most of the M_{disk} values lie at a given value of M_*. The range in M_{disk} goes down to almost $10^{-10}\ M_\odot$.

within their natal cores, and that the criteria for selecting embedded protostars produces a homogenous population.

Since the envelope density model used in the Robitaille et al. (2006) grid is a perturbative solution to the collapse of a rotating singular isothermal sphere (Terebey et al. 1984; Shu 1977), $\dot{M}_{env}$ can be related to the isothermal temperature (T_{iso}) of the core (Shu 1977):

$$\begin{aligned} \dot{M}_{env} &\simeq 0.975\frac{c_s^3}{G} \\ c_s &= \sqrt{\frac{k_B T_{iso}}{\mu m_H}} \\ T_{iso} &\approx 5.1\mu\left(\frac{\dot{M}_{env}}{2\times 10^{-6}\ M_\odot\ yr^{-1}}\right)^{2/3}\ K \end{aligned}$$

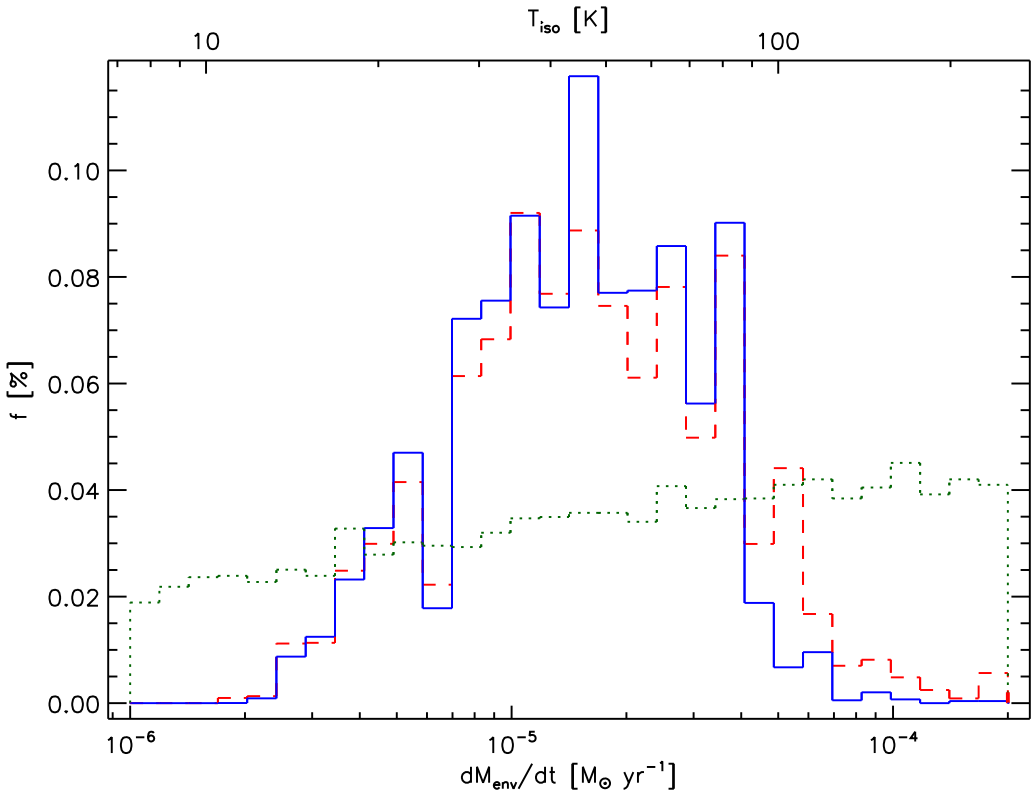

Figure 4.6: The distribution of envelope accretion rates in the quality fits. Most of the quality fits have high accretion rates, implying that the embedded sources in Perseus have dense cores.

where c_s is the isothermal sound speed. Using a mean molecular mass fraction of 2.3, the corresponding isothermal core temperature is given along the upper horizontal axis. The high accretion rates predict infall isothermal temperatures of 27–87 K, comparable to the range of envelope photosphere temperatures derived from fitting the simple 1D collapsed solution models to the Perseus data. The discrepancy between the observed core temperatures in Perseus (Johnstone et al. 2006; Rosolowsky et al. 2008) and the prediction of the singular isothermal sphere suggests that these cores cannot be supported only by thermal pressure. If only thermal pressure were required, then the infall rates would be around 2×10^{-6} $M_\odot$.

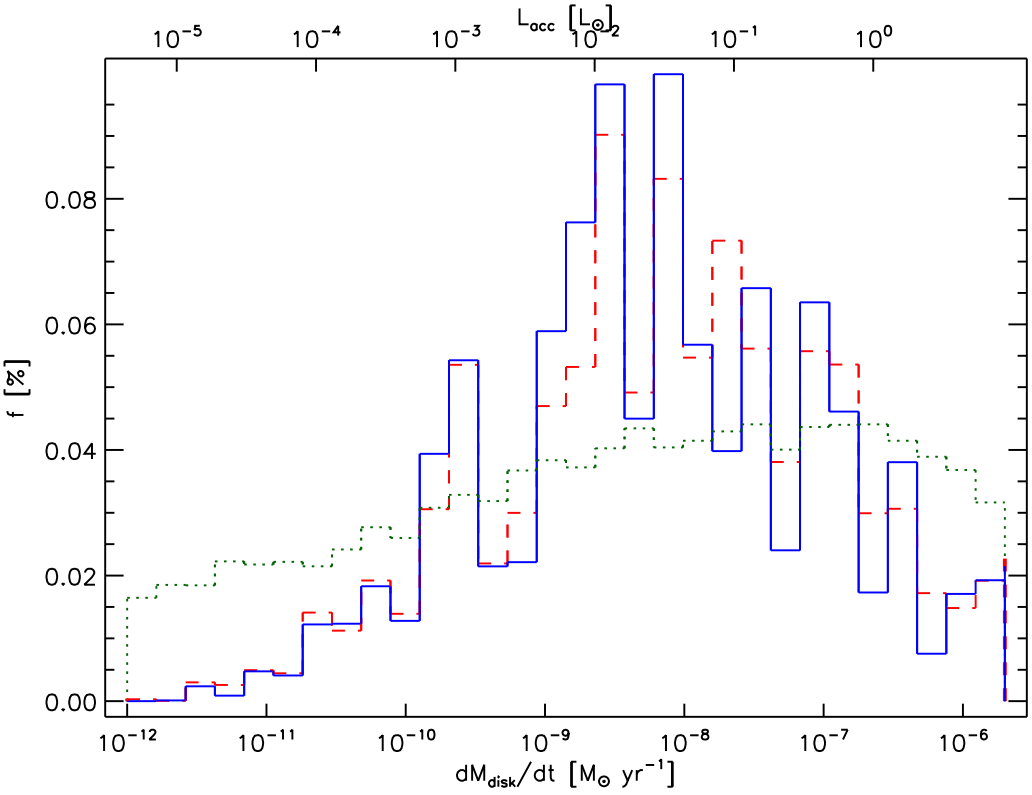

Figure 4.7: The distribution of disk accretion rates in the quality fits. Most of the quality fits show more than two orders of magnitude difference in the envelope and disk accretion rates.

4.6 Disk Accretion Rate

The disk accretion rate spans several orders of magnitude, suggesting these parameters are not well constrained by the source data. The distribution for only the red sources is very similar to the distribution for all the sources (KS probability of 94%), with both histograms peaking around 6×10^{-9} $M_\odot$ yr^{-1}. The extremely low values for $\dot{M}_{disk}$ implies that for most of the quality fits the luminosity is dominated by the protostellar luminosity. Using a typical radius and temperature for a 0.1 $M_\odot$ protostar in the Robitaille et al. (2006) grid, even with a disk accretion rate of 10^{-6} $M_\odot$ yr^{-1} the accretion luminosity is at most ≈ 0.002 $L_\odot$. To represent the contribution of accretion to L_{tot}, fiducial parameters for protostellar mass (0.5 $M_\odot$), radius (3 $R_\odot$), and temperature (3750 K) were used convert $\dot{M}_{disk}$ into L_{acc}. From Equation 2.14, the fiducial dust sublimation radius R_{sub} is approximately 6 R_*. For R_{disk}^{min}=R_{sub}, the resulting values for L_{acc} given by Equation 2.9 are given on the upper horizontal

axis of Figure 4.7.

A plot of the ratio of accretion luminosity (given by Equation 2.9) to the total luminosity, $\frac{L_{acc}}{L_{tot}}$, is shown in Figure 4.8. For most of the quality fits, the accretion luminosity provides a small fraction of the total luminosity, with L_{acc} in the range of 10^{-1}–10^{-3} L_{tot}. Only a few ($\approx 10\%$) of the quality fits have $L_{acc} > 0.1$ L_{tot}, and an even smaller fraction have the accretion luminosity dominating the stellar luminosity ($L_{acc} > 0.5$ L_{tot}). This implies either the protostellar distribution heavily favours large radii (a few $R_{\odot}$) or conversely young 'ages', or the disk accretion rates are low (c.f. Equation 2.9).

Comparing figures 4.6 and 4.7 shows a clear discrepancy between the values for

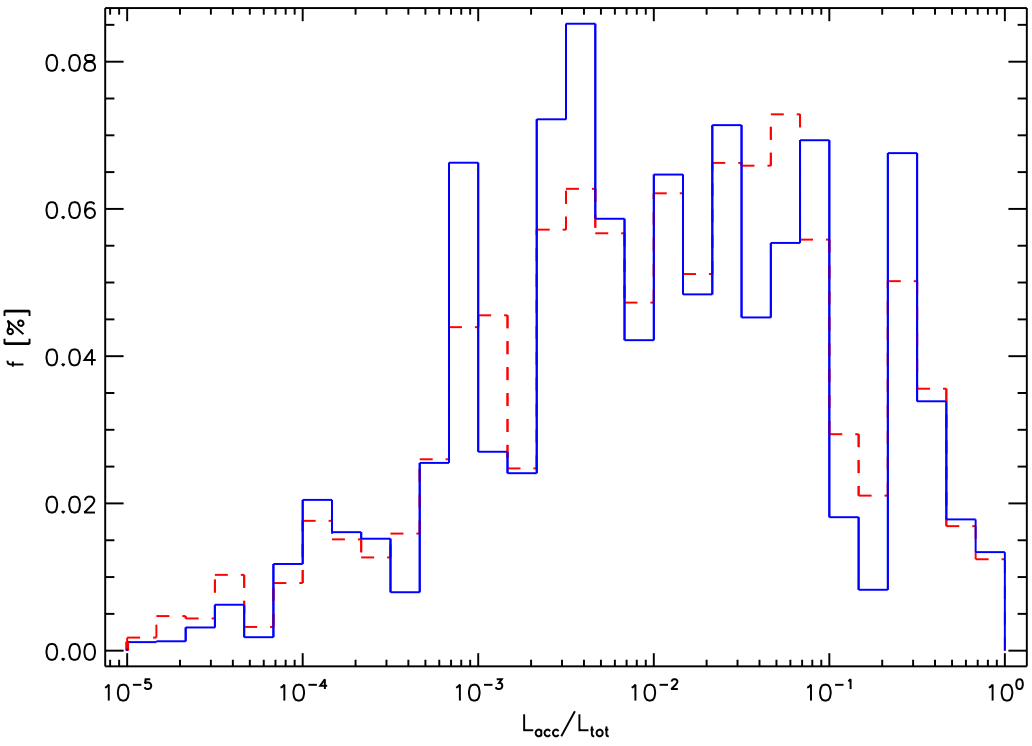

Figure 4.8: The ratio of accretion luminosity to total luminosity for the quality fits to the embedded sources in Perseus.

$\dot{M}_{env}$ and $\dot{M}_{disk}$, with most of the quality fits having two or three orders of magnitude lower disk accretion rates than envelope infall rates. The Robitaille et al. (2006) model grid sampled most of the parameters randomly, but subject to a pre-determined trend, usually with age or mass. For example, for a model with an age of 10^3 yr, θ_{cav}

was sampled randomly between 1° and 9°. Unfortunately, this means that there is no straightforward connection between the envelope and disk accretion rates. The envelope accretion rate was sampled as $\dot{M}_{env}/M_*$, and the disk accretion rate was sampled as α_{disk} and then computed using Equation 2.8. The model grid did allow for disk accretion rates that were as large (and larger) than the envelope accretion rate, but these models are extremely luminous. The fact that the fit distributions to the Perseus sources preferred envelope accretion rates 100–1000× larger than the disk accretion rate was not influenced by the way the grid sampled the parameter space, but by the requirement of low luminosities and dense envelopes.

The implication, as discussed in §2.2.3, is that the disk mass will continue to build up mass faster than it will lose the matter onto the protostar and will eventually become gravitationally unstable and collapse. From the simple back of the envelope calculations presented in §2.2.3, sustained values of $\dot{M}_{disk}$ two to three orders of magnitude lower than the envelope accretion rate will drive disk instabilities several times over the 0.5 Myr lifetime of the embedded phase of prostostellar evolution (Kenyon and Hartmann 1995; Evans et al. 2009). For example, Vorobyov and Basu (2006) found that for rotating, magnetized, and collapsing cores, the disk accretion rate spiked from 10^{-7} $M_\odot$ yr^{-1} to 10^{-4} $M_\odot$ yr^{-1} between 0.1–0.3 Myr after the onset of formation (their figure 2). This happened about 15 times, as the increased accretion rate lasted only about 100 yr. If a typical protostar experiences 10–15 such collapses through the 0.5 Myr embedded phase, then approximately 0.2–0.3% of all embedded protostars should be experiencing enhanced disk accretion rates assuming a constant star formation rate. Given the relatively small number of 49 embedded protostars in Perseus, it is thus not surprising that they all are observed to have generally low luminosities.

4.7 Disk and Envelope Inner Radius

The distribution of all the sources in Figure 4.9 looks qualitatively similar to the distribution built from just the red sources, with a KS probability of 94%. Only 50% of the quality fits to all of the embedded sources prefer $R_{disk}^{min} < 1.26$ R_{sub}. In the Robitaille et al. (2006) model grid, 10262 (51%) of the 20000 models have $R_{disk}^{min} < 1.26$ R_{sub}, of which 9520 (47%) have $R_{disk}^{min} = R_{sub}$, indicating that there may be some underlying bias towards models with no inner envelope holes. The rest of the fits are spread out over three orders of magnitude, with a wide peak from 8–63 R_{sub}, which

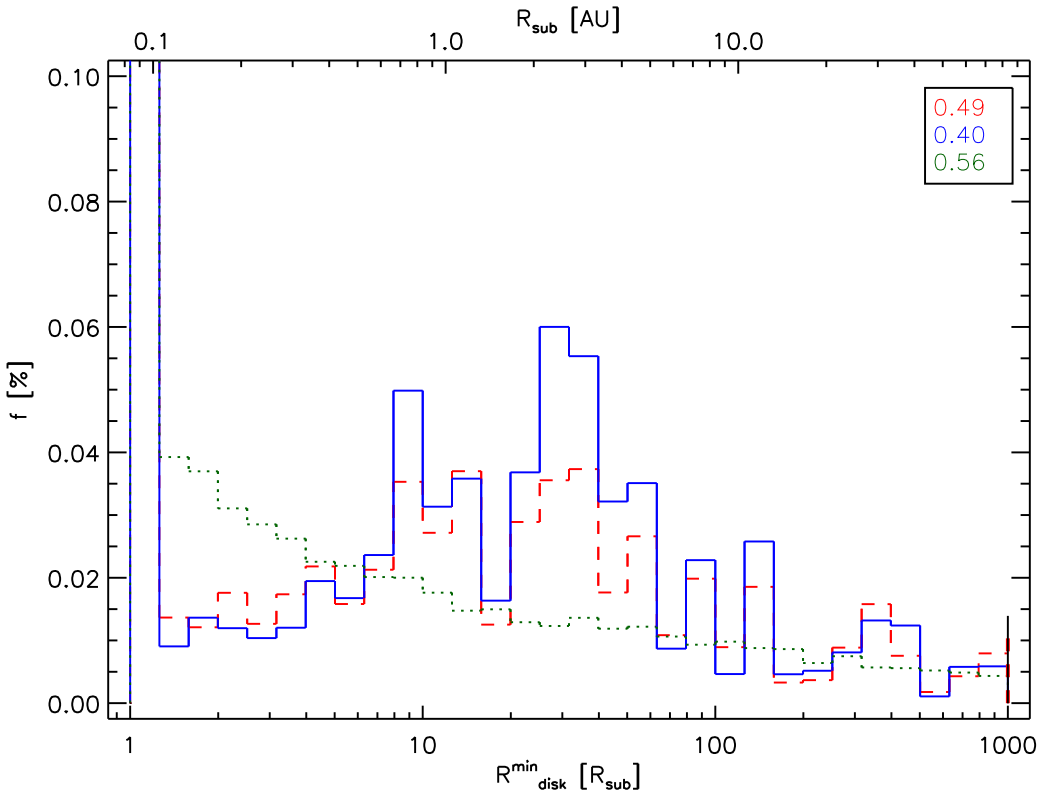

Figure 4.9: The distribution of quality fits for the disk and envelope inner radius. About 50% of the quality fits prefer $R_{disk}^{min} < 1.26\ R_{sub}$. Despite the peak at 8–63 R_{sub}, resulting inner envelope holes are only a few AU. In order to better show the distribution in R_{disk}^{min}, the upper range of the plot was forced to 0.1, and so the values for the peaks in the three distributions are given for reference.

translates into 0.67–5.3 AU using the same fiducial protostellar parameters as in §4.6. The number of quality fits for $R_{disk}^{min} > 1.26\ R_{sub}$ for the red source distribution increases to about 60%, implying that red IRAC+MIPS colours can definitely be produced by removing the inner portions of the envelope and disk.

Despite this, there is still not a significant bias towards quality fits with large inner envelope radii, as the distribution is dominated by the fits in the smallest bin ($R_{disk}^{min} \in [1.0,1.26]\ R_{sub}$). Since the Robitaille et al. (2006) model grid shows a similar behaviour, it is difficult to say with certainty whether the number of fits in this bin is purely the result of fitting the radiative transfer grid to the deeply embedded protostars in Perseus. Since the R_{disk}^{min} distribution in Figure 4.9 shows the broad peak from 8–63 R_{sub} which breaks from the Robitaille et al. (2006) model grid, it is unlikely that the quality fits in this range are biased. However, the majority of these fits with

$R_{disk}^{min} > R_{sub}$ do not provide a significant reduction in the optical depth through the envelope when considering the large envelope densities (§4.5).

4.8 Disk Outer Radius

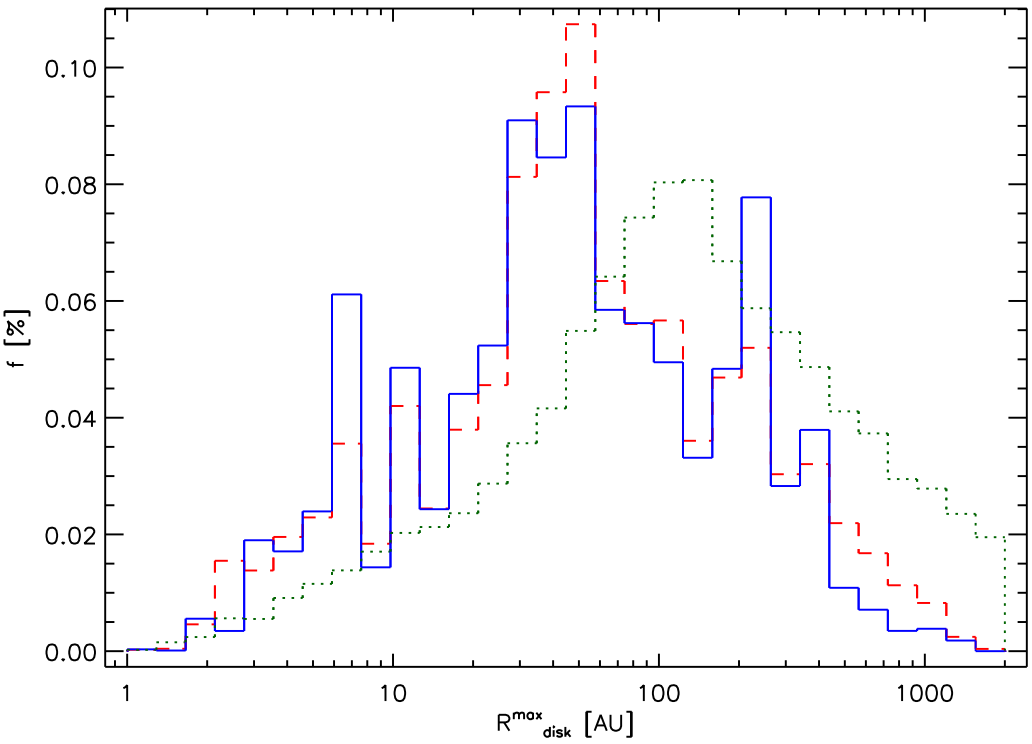

Figure 4.10: The distribution of quality fits to the disk outer radius. The majority of the disks extend from about 6–440 AU, with a peak around 40 AU.

The histograms of disk radii are quite similar between all three distributions, although the embedded protostars have peaks in R_{disk}^{max} clearly offset from the Robitaille et al. (2006) model grid. The overall width of all the histograms suggests that disks anywhere from about 6–440 AU will fit the observations, which again indicates the existence of a degeneracy in the disk parameters, specifically in $\dot{M}_{disk}$, M_{disk}, and R_{disk}^{max}, that the quality fits cannot break. The tendency for smaller disks, given the distribution of disk masses, indicates that emission from the disk itself cannot produce the red IRAC+MIPS colours (§2.2.3). Thus, there is a very small chance that these embedded protostars are in fact disk-only sources inclined upwards of 80° (edge-on).

4.9 Outflow Cavity Opening Angle

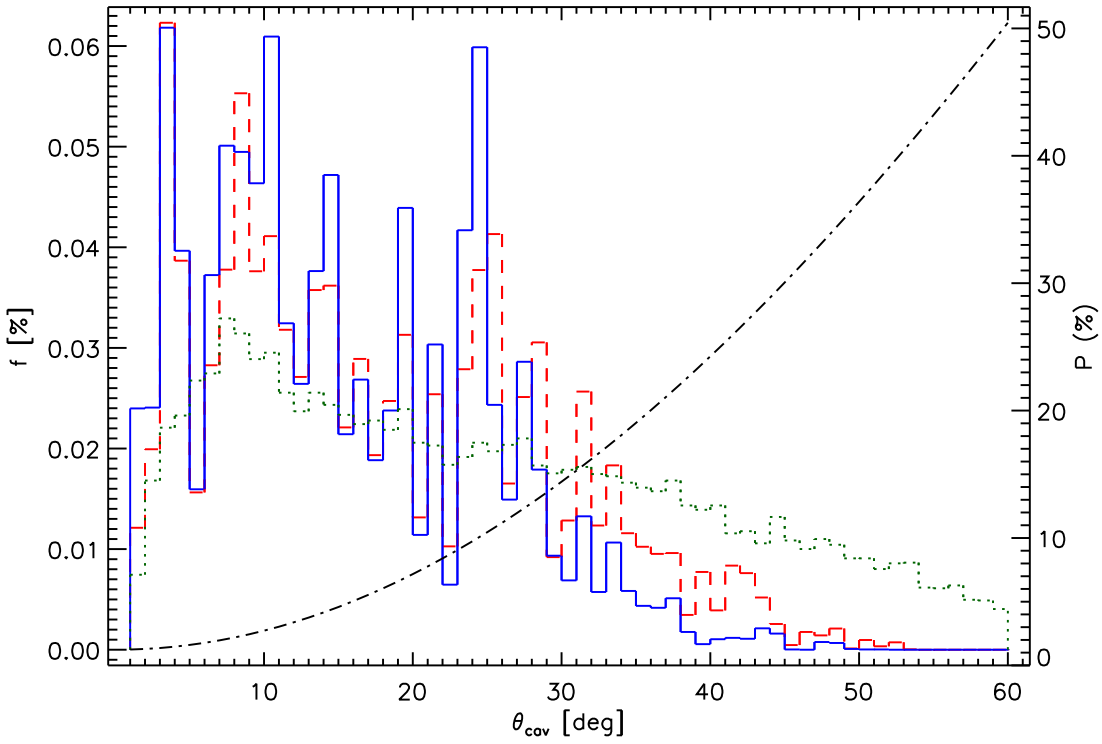

Figure 4.11: The distribution of outflow cavity opening angles for the quality fits. The distributions for the embedded sources in Perseus drop off substantially around 30° compared to the Robitaille et al. (2006) model grid. Given a random distribution of orientations, a model with an outflow cavity opening angle of 30° would have only a 13% chance of being observed through the outflow. The probability of observing through an outflow with a given cavity opening angle is shown as the dash-dot line.

The histograms for all the sources and for just the red sources are qualitatively the same, as shown in Figure 4.11, with a 34% probability they could be drawn from the same distribution. The quality fits do prefer smaller cavity opening angles to larger ones, as both histograms show significant drops around 30°, with only a very small number of quality fits with $\theta_{cav} \geq 40°$. Since the models bin the flux along the polar angle in equal bins of cosθ, the pole-on inclination at 18° (cosθ = 0.95) is the average of the fluxes from $\theta = 0°$ (cosθ=1) to $\theta \approx 25.8°$ (cosθ=0.9). This means that for most of the quality fits to the embedded protostars only the 18° inclination could possibly be considered as viewing *through* the outflow cavity. All other inclinations

of the YSO SED can be considered as viewing through the protostellar envelope.

Assuming the outflow cavities are azimuthally symmetric, it is possible to correlate the outflow opening angle to a probability that an observer would have a line of sight through the outflow given a random distribution of outflow orientations. Since the resolution of the IRAC and MIPS cameras are on the order of a few arcseconds, it is safe to assume that the observer can probe a YSO with an infinitely small beam. Furthermore, the orientation of the outflow cavities does not significantly influence the probability, since so long as a portion of the solid angle subtended by the outflow is directed towards the observer we can consider that the observer has a direct line of sight through the cavity. Although the intensity will depend on orientation, due to the area of the outflow opening subtending the observes plane of the sky as well as scattering off of the cavity walls, this is unimportant when considering the possibility of observing through the outflow. Since neither the orientation nor the observer's beam size have an influence, the probability of observing through the outflow is merely related to the solid angle subtended by the outflow.

For an outflow opening angle θ_{cav}, the solid angle of the outflow is given by:

$$\begin{aligned} \Omega_{cav} &= \int_0^{2\pi} d\phi \times 2 \int_0^{\theta_{cav}} \sin\theta d\theta \\ &= 4\pi(1 - \cos\theta_{cav}) \end{aligned}$$

assuming again that the outflow is azimuthally symmetric, and the factor of 2 comes from the fact that the outflows are assumed to be bipolar. As the probability of detecting the outflow is directly related to the solid angle that it subtends, given the above the probability may be written as:

$$P = \frac{\Omega_{cav}}{4\pi} = 1 - \cos\theta_{cav}$$

The dash-dot line in Figure 4.11 shows this probability as a function of cavity opening angle. Although the majority of the quality fits have an opening angle smaller than 30°, one can consider an extreme case of all the embedded protostars in Perseus having outflow opening angles of 30°. Given random orientations, at most 13% of these protostars would be observed through the outflow cavity; in other words, only 7 out of the 49 embedded protostars in Perseus should have outflows oriented towards the observer.

4.10 YSO Inclination Angle

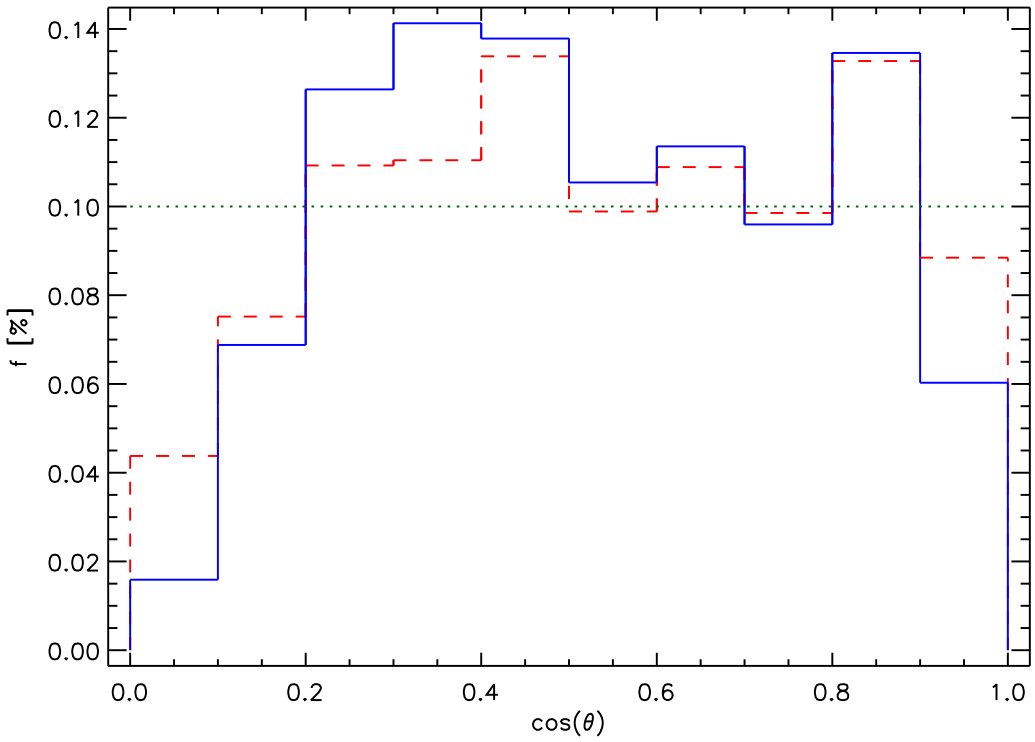

Figure 4.12: The distribution of inclination angles for the quality fits to the embedded protostars in Perseus. The green dotted line here represents the mean of all the inclination angles. Aside from a lack of models at edge-on inclinations (see the discussion in §4.2, the distribution of inclination angles is relatively flat.

It is immediately clear in 4.12 that there is no significant difference when the quality fits to the full embedded protostar list or to just the red sources is binned. The embedded sources clearly are not well fit with edge-on ($\cos\theta = 0$) models; flux at the IRAC and 2MASS wavelengths would be undetectable in edge-on sources due to the extreme optical depth through the envelope and the disk. Larger cavity opening angles and/or increased luminosity would be required to contribute a significant amount of scattered light into the edge-on inclinations at these shorter wavelengths. Both distributions seem to be relatively flat for $\cos(\theta)$ >0.2, or for inclinations less than 78°. This implies that for a given source embedded within its natal core, it is equally probable to fit it with a model that is inclined 10°as opposed to a model that is inclined 60°. The number of quality fits in the 18° bin (inclinations less than 26°)

actually *decreases* over fits at intermediate inclinations.

As the SEDs in the Robitaille et al. (2006) model grid were binned equally in the cosine of the polar angle, as in §4.9 the probability of that inclination to the observer is also equal between bins. The lack of edge-on models is not surprising, as given the distribution of luminosities in Figure 4.1 sources with disks seen edge on should be particularly hard to identify. The fact that the inclination angle is not constrained to any particular value supports the argument put forth in §4.9 that the embedded protostars identified by Robitaille et al. (2007) cannot all have their outflows oriented towards earth. If that were the case, the 18° bin would be heavily favoured over the other inclinations, which is clearly not seen in the quality fits. The red sources in Perseus actually have a lower fraction of quality fits in the 18° bin, implying that red IRAC+MIPS colours cannot only be created by observing through the low density outflow cavities.

Given that in Figures 3.1 and 3.5 significant variation is seen in the best fit models to those sources, L1448-IRS 2 and NGC 1333-IRAS 4B, it may be that a solid detection in the 2MASS wavelengths may help narrow down the scatter in either inclination or outflow cavity opening angle. Inspecting the individual embedded source distributions without 2MASS detections show that some of these sources the distribution in inclination angle is broad, whereas for other sources the distribution is noticeably peaked at a specific inclination. There is a trend for the inclinations to peak in the 76°, 70°, and 63° bins, although there are also a significant number of fits in the 81°, 57°, 49°, 41°, and 32° bins as well. For all of these sources, however, the outflow cavity opening angle distributions are consistent with that of the ensemble. All of this suggests that although the 2MASS data does help to narrow down the inclination, the ensemble distribution is not significantly affected if 2MASS data is unavailable.

The deficit of models in the 18° bin suggests that some of the embedded sources in Perseus do not like inclinations through the outflow. Of the 48 embedded protostars in Perseus that were fit to the Robitaille et al. (2006) model grid, only 5 sources have distributions in inclination that peak in the 18° bin: NGC 1333-SVS 13, NGC 1333-SVS 12, NGC 1333-IRAS 2B, 03293+31234, and 03278+30121. There is no visible correlation in IRAC+MIPS colours or 2MASS fluxes between these five sources. There are other sources with inclination distributions that peak in the 32° bin, which also have fits in the 18° bin. Thus, there does not seem to be a correlation between the dip at 18° in Figure 4.12 and any of the observable properties of the embedded

protostars. More likely the dip at 18° suggests that the density used by the Robitaille et al. (2006) model grid in the outflow cavities may be too low to produce the red colours seen in the embedded protostars; both NGC 1333-SVS 13 and NGC 1333-SVS 12 are two of the brightest sources and were not identified by their IRAC+MIPS colours (Jørgensen et al. 2007).

4.11 Best Fit Extinction

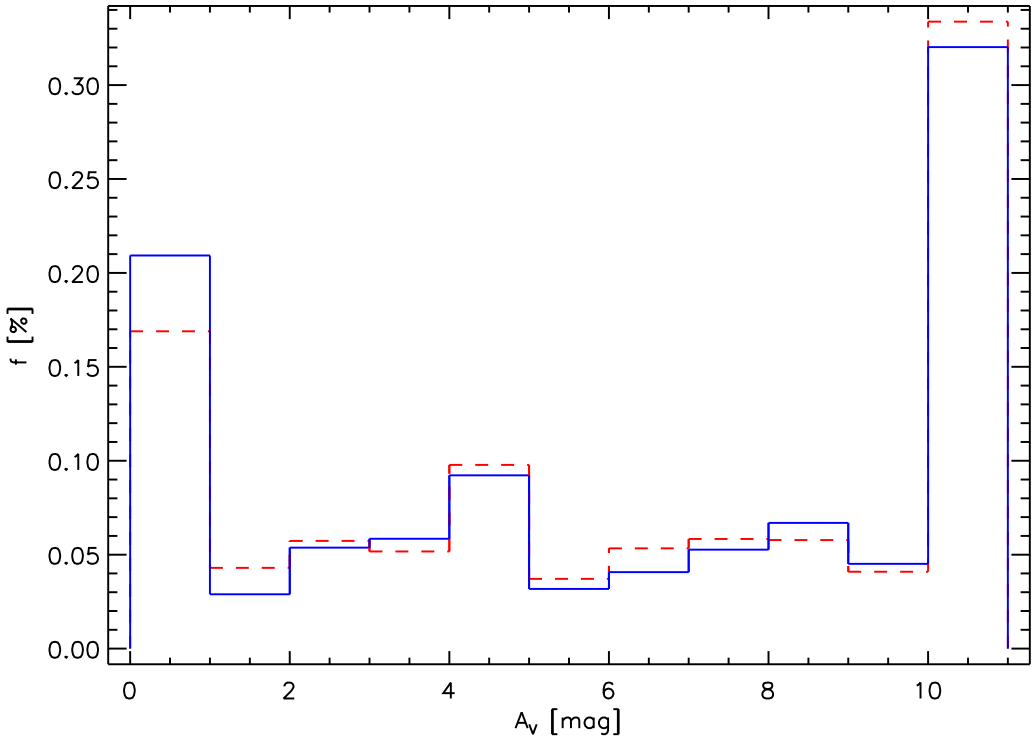

Figure 4.13: The distribution of best fit visual extinction for the quality fits to the embedded protostars. A clear preference of fits with $A_V = 10$ is observed, although this may be due bias from the Robitaille et al. (2007) SED fitting tool.

The distribution of the best fit visual extinction is given in Figure 4.13. Roughly a third of the quality fits favoured $A_V = 10$, indifferent of whether only the red sources were binned. Thus, only a small amount of extinction beyond that inherent to the dense core is required to produce the red IRAC+MIPS colours. The extinction law used by the Robitaille et al. (2006) would produce reddening values of $E_{[3.6]-[4.5]}$

= 0.14 and $E_{[8.0]-[24]} = 0.22$, not large enough to redden the IRAC+MIPS colours of a naked (Class II or III) protostar. Almost all of the embedded protostars run through the Robitaille et al. (2007) SED fitting tool had upwards of 60% of the fits returned with $A_V = 10$, producing a significant bias towards models with poor fits to the fluxes and high A_V. These poor fits (the χ^2 distribution quickly increases across several orders of magnitude) were usually models with blue IRAC+MIPS colours, which is apparent from Figure 4.13. Most of these blue models are star+disk systems with tenuous envelopes that theoretically would be unable to reproduce the observed 850 μm fluxes observed by Kirk et al. (2006). Thus, the quality cuts do a good job of removing such poorly fit models, and reducing the total number of fits with A_V = 10.

Chapter 5

Discussion

5.1 Kicking at the Darkness

The results given in §4 focused on individual parameters and the resulting distribution of quality fits to the embedded protostars in Perseus (Jørgensen et al. 2007). A number of trends were identified, and it is worthwhile to discuss how these results come together to yield a possible explanation for the prevalence of emission between 1–10 μm. The increased sensitivity and resolution of Spitzer in the near infrared over previous space observatories, such as the ISO and IRAS, gave the ability to detect these embedded sources for the first time. The presence of emission in the near- and mid-infrared from these sources is an altogether theoretical problem, as from simple arguments based on first principles deeply embedded protostars should not have emission at $\lambda \lesssim 10$ μm. Detectable emission at these wavelengths must be due to the presence of a more complicated distribution of dust and gas, as the optical depth through the dusty envelope must be lower than if it were spherical and non-rotating (e.g. Shu 1977). The Whitney et al. (2003b) radiative transfer code includes a number of features; infalling rotating envelope, accreting disk, bipolar outflow cavities, and possible large inner envelope radii, that move away from such an idealized picture as that of a singular isothermal sphere (Shu 1977). By fitting a subset of deeply embedded protostars in Perseus identified by Jørgensen et al. (2007), this thesis sought to determine which of these features was responsible for the detectable emission at 1–10 μm.

One possible explanation for the red colours seen in the embedded protostars in Perseus is that these sources may actually be dominated by their disks, and have very

tenuous envelopes. For example, evolved Class II systems will have dispersed most of their envelope through the outflow, accretion, and stellar winds, and yet the dusty disk will still produce significant emission in the infrared. However, most sources do have fluxes through 1–10 μm that rise considerably, suggesting the presence of dusty envelopes, and only a few models exhibit relatively flat SEDs through the FIR at 70 μm. The culprit for significant emission at 70 μm is warm dust at 30–70 K, significantly higher than the typical core temperatures observed in Perseus (e.g. Johnstone et al. 2006; Rosolowsky et al. 2008). The fact that the simple 1D toy model proposed in §3.3 fits almost all of the embedded protostars quite well implies significant dust and gas envelopes, with a density profile exponent close to $\alpha = 3/2$. Finally, the Robitaille et al. (2006) SED fitting tool, when combined with the 850 μm flux and χ^2_{best} quality criteria, predicts envelope infall rates of $\sim 10^{-5}$ M$_\odot$ yr^{-1} for most of the acceptable fits to the embedded protostars in Perseus. Since the envelope infall rate was used to set the envelope density for the Robitaille et al. (2006) model grid, this implies the existence of dense envelopes surrounding these protostars.

A second explanation for the 1–10 μm emission from these embedded protostars is that large holes have been bored in their inner envelopes (Jørgensen et al. 2008), through the formation of stellar or planetary companions (e.g. Artymowicz and Lubow 1994; Guilloteau et al. 1999; Mayama et al. 2010). Although the results of §4 cannot discredit this explanation as a plausible for some of the embedded protostars in Perseus, certainly not all of the red colours and 1–10 μm emission from the embedded protostars are due to inner envelope holes. Looking at Figure 4.9, it is apparent that only about 50% of the quality fits to the embedded sources prefer inner envelope and disk radii larger than 1.26 R$_{sub}$. Those fits were also distributed across three orders of magnitude, with a peak at around 30 R$_{sub}$, which converts to only a few AU given the most likely parameter values given by Figures 4.1 and 4.2. Inner holes of a few AU may allow 1–10 μm emission from the protostellar surface to escape the envelope if the density is low enough, but photons scattered from outflow cavity walls will also contribute and most likely dominate (see Figure 2.3, which has an inner envelope radius of 0.32 AU and shows photons scattered from cavity walls and emitted from the protostar).

A third possibility is that the outflow direction of these embedded protostars is oriented towards the observer. As with the inner hole mechanism, emission at 1–10 μm due to the line-of-sight being through the outflow cannot explain all of the deeply embedded protostars in Perseus. The majority of quality fits to the outflow cavity

opening angle (Figure 4.11) are below $\theta_{cav} \approx 30°$. Since the pole-on bin centered at 18° is the polar average of inclinations 0°–26°, a considerable amount of quality fits with pole-on inclinations would be required to corroborate the distribution of θ_{cav}. Clearly this is not the case, as shown in Figure 4.12, as the pole-on bin is rather evenly distributed with the intermediate inclination bins, and only the edge-on bin at 87° containing less fits.

Thus, it is photons scattering off of outflow cavity walls that produces the observed emission at 1–10 μm for most of the deeply embedded protostars in Perseus. Since scattered photons should be observable as soon as an outflow cavity is created, it follows that even the most deeply embedded protostars should be detectable in the MIR by an instrument with high enough sensitivity. The inclusion of scattered emission almost always improves the modeling of YSO images (e.g. Whitney et al. 2003b), and scattered emission nebulas are observed in many star forming regions.

The distribution of YSO inclinations for the quality fits is relatively flat between $\cos\theta = 0.2$–0.9, with a lower number of fits in the 18°, 81°, and 87° bins. Thus, the mechanism by which emission from the protostar can escape the envelope must not depend on inclination. In figures 2.7 and 2.3, the SEDs built from scattered photons are almost the same regardless of inclination, because photons need only scatter from enough distance away to bypass the densest portions of the envelope (Figure 2.4, and because scattering of dust particles should be roughly isotropic. Furthermore, the cavity opening angle distribution is relatively flat for $\theta_{cav} \lesssim 30°$, implying that quality fits to the sources only require a cavity, to produce enough scattered emission in the MIR. It could even be argued that the distribution of cavity opening angles is actually sloped downward with wider cavities, so smaller θ_{cav} are preferred. Since the inner envelope hole mechanism would not be biased towards any particular outflow cavity opening angle, and the line-of-sight through the outflow mechanism would prefer larger cavity opening angles to smaller ones, there should be no reason for the quality fits to prefer smaller outflow cavity opening angles. The results presented here suggest that radiative transfer modeling of embedded protostars should include narrow outflow cavities in order to properly model the scattered flux at 1–10 μm.

5.2 Further Results

5.2.1 The Embedded Protostar Next Door

The ensemble of quality fits to the deeply embedded sources in luminosity and protostellar mass are consistent with what would be expected in Perseus. The distribution of L_{tot} in Figure 4.1 suggests that the deeply embedded protostars in Perseus are not intrinsically bright, preferring luminosities between 0.3–3 $L_{\odot}$. These values are consistent with low mass protostars, as they are several times larger and a few hundred degrees cooler than their main sequence progeny. Although for a few of the quality fits the accretion luminosity dominated over the stellar luminosity, as shown in Figure 4.8, most of the fits required no boost from accretion, and hence low disk accretion rates (Figure 4.7). This is also supported by the quality fits to the protostellar mass. The distribution shown in Figure 4.2 is compliant with the initial mass functions of Salpeter (1955), Miller and Scalo (1979), and Kroupa (2001). Furthermore, the distribution of protostellar mass to core mass (Figure 4.3) is consistent with $\frac{M_*}{M_{core}} \sim 0.1$, which is to be expected if the protostar only accretes mass from its surrounding core in the deeply embedded stage. Thus, these embedded protostars are a representative sample of YSOs rather than a particular subset.

This does then beg the question of why some the deeply embedded sources exhibited extremely red [3.6]-[4.5] and [8.0]-[24] colours? Aside from subtle differences (for example, in Figure 4.1), the majority of the figures showed distributions for the quality fits to all sources consistent with the quality fits to only the red sources, both visually and by the KS test. One possible explanation is that the effects of scattering from cavity walls, viewing through the outflow cavities, and large inner envelope radii combine to produce a wide range of IRAC+MIPS colours. In other words, a representative sample of embedded sources will show a similar distribution in colour space. Another possible explanation is that the [3.6]-[4.5] colours are contaminated by shocked H_2 line emission, most likely produced along the outflow cavity walls. A number of quality fits were unable to fit the data at 4.5 μm as well as at 3.6 μm, 5.8 μm, and 8.0 μm. In Figure 5.1, the [3.6]-[4.5] colours are plotted against the [3.6]-[5.8] (calculated from the final data presented in Evans et al. 2009). Only two sources have [3.6]-[5.8] colours bluer than the [3.6]-[4.5] colour, suggesting that these sources are not intrinsically blue sources (i.e. Class II or Class III) sources coincident with shocked H_2 emission. The lack of polycyclic aromatic hydrocarbons (PAHS)

might also contribute to the red [8.0]-[24] colours in some of the sources, since PAHs exhibit prominent emission at 8.0 μm. The distribution of dust grain sizes might also influence the emission (e.g. Ossenkopf and Henning 1994) in the IRAC and MIPS bands. Further modeling is needed in order to differentiate between these scenarios.

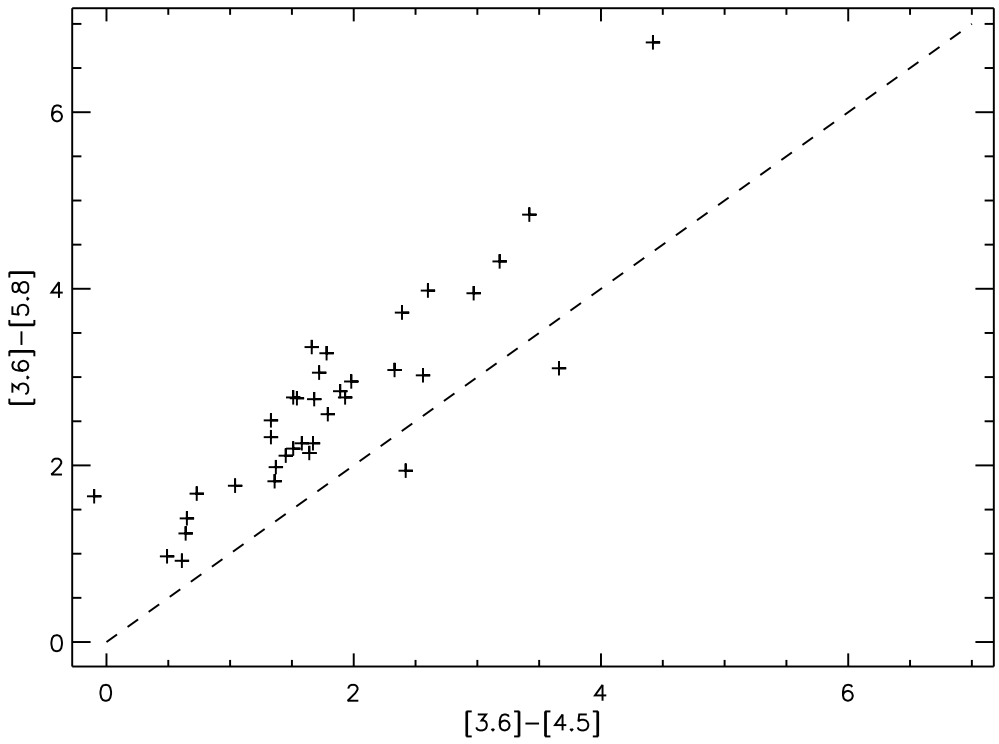

Figure 5.1: The [3.6]-[4.5] and [3.6]-[5.8] colours of the embedded protostars are plotted. Red [3.6]-[5.8] over [3.6]-[4.5] colours will lie above the one-to-one line, suggesting that shocks are not the primary cause for red [3.6]-[4.5] colours in the embedded protostars. Note that these colours were calculated from the fluxes taken from the data release of Evans et al. (2009) rather than the data release of Jørgensen et al. (2006).

5.2.2 Disk Parameters Unconstrained

The quality fits for the disk mass, radius, and accretion rate were all poorly constrained, as shown by the broad peaks and parameter ranges spanning several orders of magnitude in figures 4.4, 4.10, and 4.7. This could imply that the disks are not very important in the SEDs of these deeply embedded sources, or that combinations of these three parameters were degenerate. Another possibility is that the low mass

protostars required more massive disks than the Robitaille et al. (2006) model grid allowed. The disk masses resulting from the quality fits to four sources in Perseus, L1448-C(N), NGC 1333-IRAS 2A, NGC 1333-IRAS 4A, and NGC 1333-IRAS 4B, were generally found to be lower than observed (Jørgensen et al. 2009), especially for 4A and 4B. Furthermore, the Robitaille et al. (2006) model grid did not sample $M_{disk} \gtrsim 0.1\times$ $M_{\odot}$ for $M_{*} \lesssim 1$ $M_{\odot}$. Since the quality fits to each source could not then have matched the significant disk masses detected by Jørgensen et al. (2009), it is possible that the poor fits to $\dot{M}_{disk}$ and R_{disk}^{max} were a result.

5.2.3 Extremely High Envelope Mass Infall Rates

The high envelope infall rates resulting from the quality fits to the embedded Perseus sources are extremely surprising in the context of star formation. Since the conversion from $\dot{M}_{env}$ to T_{iso} comes from an isothermal sphere model (Shu 1977), there exists an inconsistency between the isothermal temperature and the observed core temperature. In the singular isothermal sphere model (Shu 1977) only the radiation pressure counteracts the gravitational pull, and for a temperature of 10 K the isothermal sphere collapses at a rate 2×10^{-6} $M_{\odot}$ yr^{-1}. The higher $\dot{M}_{env}$ implies singular isothermal sphere temperatures of 20–80 K, and that these collapsing dense cores may in fact not be isothermal. That is, they possess additional support mechanisms aside from thermal pressure to balance out the contraction due to gravity. This additional support may be in the form of magnetic fields or in turbulence, although recent work by Kirk et al. (2007) and Pineda et al. (2010) have shown that there may not be significant turbulence exhibited by most cores in Perseus.

These extremely high mass infall rates are orders of magnitude larger than the disk accretion rates, which will eventually drive the disk to instability (e.g. Shu et al. 1994; Vorobyov and Basu 2006). Sporadic or variable disk accretion has been suggested as the solution to the luminosity problem (e.g. Kenyon and Hartmann 1995; Vorobyov and Basu 2006; Evans et al. 2009; Dunham et al. 2010), and the results of this thesis support that conclusion. Where these works differ from the analysis presented in §4 is that the authors approached the idea of variable disk accretion as a possible explanation to the relatively low luminosities observed in nearby star forming regions. This thesis approached the problem from a completely different direction; a set of deeply embedded protostars in Perseus were studied in a statistical manner by fitting the observed fluxes to a grid of radiative transfer models (Robitaille et al. 2006). The

results of fitting to the radiative transfer grid *suggests* that these embedded sources are described by disk accretion rates about *three orders of magnitude* lower than the envelope mass infall rate. By not assuming that the low luminosities exhibited by these deeply embedded protostars are somehow peculiar, this thesis found that the disk accretion rates are *too low* when compared with the envelope infall rates. Thus, using either the approach of previous authors or the approach presented in this thesis, a connection between the low luminosities of deeply embedded protostars and low disk accretion rates is found.

Chapter 6

Conclusions

A statistically significant and unbiased population of deeply embedded protostars identified in Perseus (Jørgensen et al. 2007) have been studied by fitting a grid of radiative transfer models (Robitaille et al. 2006) and applying a quality cut based on the correlation between the envelope density and the observed core flux. The resulting quality fits to this population of sources have been studied by creating histograms of a number of different model parameters. A number of conclusions were reached regarding the sample:

- The quality fits for the total luminosity and protostellar mass are consistent with what one would expect for typical protostars in Perseus. The ratio of the predicted protostellar mass to the observed core mass is approximately 0.1, consistent with the idea that the protostellar mass is built from the core mass (and hence is lower in the embedded stages).

- There is no significant difference in any parameter when only the sources with extremely red [3.6]-[4.5] and [8.0]-[24] colours are studied.

- The disk parameters are not well constrained by the quality fits, which could be due to the fact that the Robitaille et al. (2006) model grid did not sample massive enough disks in the low-mass area.

- The disk accretion rate is about 100–1000 times lower than the envelope accretion rate, suggesting that the disk will build up mass until it collapses onto the protostar. Furthermore, there is no reason to believe this has not happened already for some of these deeply embedded objects.

- The high envelope mass infall rates require isothermal temperatures warmer than the ambient cloud and the observed Perseus core temperature. This implies that some source of external support, such as magnetic fields or turbulence, contribute to delaying collapse and is amenable to the high infall rates.

- The mechanism through which short mid-infrared wavelength photons escape the dense core has been studied. Although the presence of an inner envelope hole or the chance alignment of the outflow direction with the observers line of sight are both still viable options, neither are the primary recourse that can explain the sizeable sample in Perseus. Only about half of the quality fits to the observed Perseus sample required R_{disk}^{min} larger than the dust sublimation radius, the majority of outflow cavity opening angles were less than 30°, and all inclinations, except for the edge-on inclination, were more or less evenly distributed. These all lead to a situation were scattering of photons off of cavity walls provide a considerable amount of mid-infrared flux despite these protostars being deeply embedded within their natal envelopes.

- Caution must be taken with the model grid when fitting sub-mm fluxes of sources. Without near- or mid-infrared fluxes, the design of the grid may predispose fits with luminosities and envelope masses significantly higher than if the shorter wavelength data was available. Furthermore, the sub-mm opacity used by the models may not agree with the sub-mm opacity used by an observer, further complicating the analysis.

This thesis provides a wealth of avenues upon which to expand the analysis described in the previous chapters:

- Given that shocked H_2 emission may be contaminating the IRAC 4.5 μm band, the quality fits to a given source show evidence of being unable to simultaneously fit all four IRAC bands. The excess emission between the model YSO SED and the observed 4.5 μm flux is then a direct measurement of the energy deposited by the outflow as shocks along the outflow cavity walls. This excess emission can then be fit to radiative transfer models of line emission and shock heating. The excess emission may also be used to compare to the results of Arce et al. (2010), who described a number of outflow candidates in Perseus both qualitatively and quantitatively. The results of the outflow masses, momenta, and energy can be compared to the result from measuring the excess emission at 4.5 μm.

- A similar comparison with the results of Arce et al. (2010) could be done regarding the disk accretion rates shown in Figure 4.7. Since outflows are believed to be launched from the protostellar disk, the disk accretion rates given by the quality fits can be compared to the outflows associated with that source as a consistency check.

- Another possible small project would be to study the colours of the deeply embedded protostars in order to find any correlations between a given parameter and the redness of the IRAC+MIPS colours.

6.1 Future Work

With new instruments and observatories recently coming online, and future observatories about to become reality, there are a number of ways this project could benefit from access to these telescopes. The new SCUBA-2 instrument on the JCMT promises increased sensitivity over SCUBA, which would allow for an improved measurement of the core fluxes for each of the deeply embedded protostars in Perseus. The recent launch of the Herschel Space Observatory, with its two photometric instruments, the Photodetector Array Camera and Spectrometer, and the Spectral and Photometric Imaging Receiver, would be able to provide photometry from 60–500 μm, filling out the significant gap in the SEDs between the MIPS 70 μm and the SCUBA 850 μm fluxes. This would allow for a more accurate determination of the integrated luminosity for the 1D collapse model described in §3, as well as improving the resulting fits to the sources from the Robitaille et al. (2007) SED fitting tool. Furthermore it would allow for a more accurate determination of which type of opacity profile would be best suited to the dense cores observed in Perseus (Figure 3.2), since the most significant changes between the profiles, aside from the 3 μm ice band and the 10 μm silicate band, is in the far-infrared and submillimetre. Finally, ALMA will provide high resolution interferometric studies of each of the 49 deeply embedded sources. It will be able to probe the physical structure of each of the cores containing a deeply embedded protostar, in order to determine which cores have larger inner radii (e.g. Jørgensen et al. 2005).

Appendix A

Additional Information

Table A.1: Code parameters varied to create Robitaille et al. (2006) grid

Symbol	Description	Unit
	Stellar Parameters	
M_*	Protostellar Mass	$M_\odot$
R_*	Protostellar Radius	$R_\odot$
T_*	Protostellar Temperature	K
	Envelope Parameters	
$\dot{M}_{env}$	Envelope Accretion Rate	$M_\odot$ yr^{-1}
R_{env}^{max}	Envelope Outer Radius	AU
θ_{cav}	Cavity Opening Angle	$^\circ$
ρ_{cav}	Envelope Cavity Density	g cm^3
ρ_{amb}	Ambient Density	g cm^3
	Disk Parameters	
M_{disk}	Disk Mass (gas and dust)	$M_\odot$
α_{disk}	Disk Accretion Parameter	
R_{disk}^{max}	Disk Outer Radius	AU
R_{disk}^{min}	Disk Inner Radius	R_{sub}
z_{min}	Disk Scaleheight Factor	
β	Disk Flaring Power	

A.1 On Colours and Fluxes

The '[]' designation refers to the brightness of an object at a given wavelength in logarithmic units. In other words, if the flux (energy per unit time per unit area per unit wavelength) at a wavelength λ is denoted by F_λ, the brightness $[\lambda]$ is given by:

$$[\lambda] = -2.5 \log (F_\lambda) + C_{sys}$$

where C_{sys} is a constant used to scale the brightness to the photometric system in use. The colour of an object at any two wavelengths is given by $[\lambda_1]$-$[\lambda_2]$, where $\lambda_1 < \lambda_2$:

$$\begin{aligned} [\lambda_1] - [\lambda_2] &= -2.5 \log (F_{\lambda_1}) + C_{sys} - (-2.5 \log (F_{\lambda_2}) + C_{sys}) \\ &= 2.5 \log (\frac{F_{\lambda_2}}{F_{\lambda_1}}) \end{aligned}$$

When converting the IRAC and MIPS fluxes into the Vega-magnitude system, the IRAC absolute calibration fluxes from Reach et al. (2005) and the MIPS absolute calibration fluxes from Rieke et al. (2008) should be used. The absolute calibration flux is the total flux an object must have in order to yield a zeroth magnitude measurement in the Vega-magnitude system, and can be used instead of C_{sys} since:

$$[\lambda] = -2.5 \log (\frac{F_\lambda}{F_{\lambda_z}})$$

where F_{λ_z} is the absolute calibration flux at λ. Similarly:

$$\begin{aligned} [\lambda_1] - [\lambda_2] &= -2.5 \log (\frac{F_{\lambda_1}}{F_{\lambda_{z_1}}}) + 2.5 \log (\frac{F_{\lambda_2}}{F_{\lambda_{z_2}}}) \\ &= 2.5 \log (\frac{F_{\lambda_2} F_{\lambda_{z_1}}}{F_{\lambda_1} F_{\lambda_{z_2}}}) \end{aligned}$$

For each of the sources listed in table A.2, the YSO candidate list in Perseus (Jørgensen et al. 2006; Rebull et al. 2007; Evans et al. 2009) was searched for the closest match, using the IDL routine GCIRC. The 2MASS, IRAC, MIPS, and SCUBA fluxes are given in tables A.3, A.4, and A.5. Unlike Jørgensen et al. (2007), a quality cut based on signal to noise was not made, and so some of the sources have available fluxes in table A.4 and table A.5 but no [4.6]-[4.5] nor [8.0]-[24] colours in table A.2. The decision was made to only reject fluxes that were bandfilled; if a source was detected reliably in the other IRAC and MIPS bands, then an aperture was

drawn over the position and a flux measurement was taken. Since these fluxes can be unreliable (c.f. c2d product delivery document), and in most cases the bandfilled fluxes did not exhibit typical YSO characteristics, they were not used. Note that the source commonly associated with HH 211-FIR has only two available fluxes, and so could not be processed by the Robitaille et al. (2007) SED fitting tool.

The fluxes for the red sources found by Jørgensen et al. (2006) are slightly different than those given in tables A.4 and A.5 as the c2d data for all clouds was updated for the full delivery (Evans et al. 2009). In order to keep consistency with the analysis of Jørgensen et al. (2007), the colours given in table A.2 were not updated to reflect the new fluxes. For the most part, the fluxes did not change considerably, and a plot of the [3.6]-[4.5] and [8.0]-[24] colours have been plotted against their 'updated' values for comparison in Figure A.1. Only a few sources have significant changes, mostly in their [3.6]-[4.5] colours, as evidenced by the relatively small scatter about the one-to-one line. Sources with notable changes are 03285+31111 (from -0.4 to 1.4 in [3.6]-[4.5]), NGC 1333-IRAS 4C (from 3.1 to 0.5 in [3.6]-[4.5]), and 03439+32031 (from 1.2 to -0.1 in [3.6]-[4.5]). Both 03285+31111 and NGC 1333-IRAS 4C were identified as embedded sources because they lay within 15″ of the centre of a core at 850 μm. Only 03439+32031 would be removed from the embedded sources list if the new colour was adopted, as it was only identified because it satisfied the [3.6]-[4.5] and [8.0]-[24] criteria.

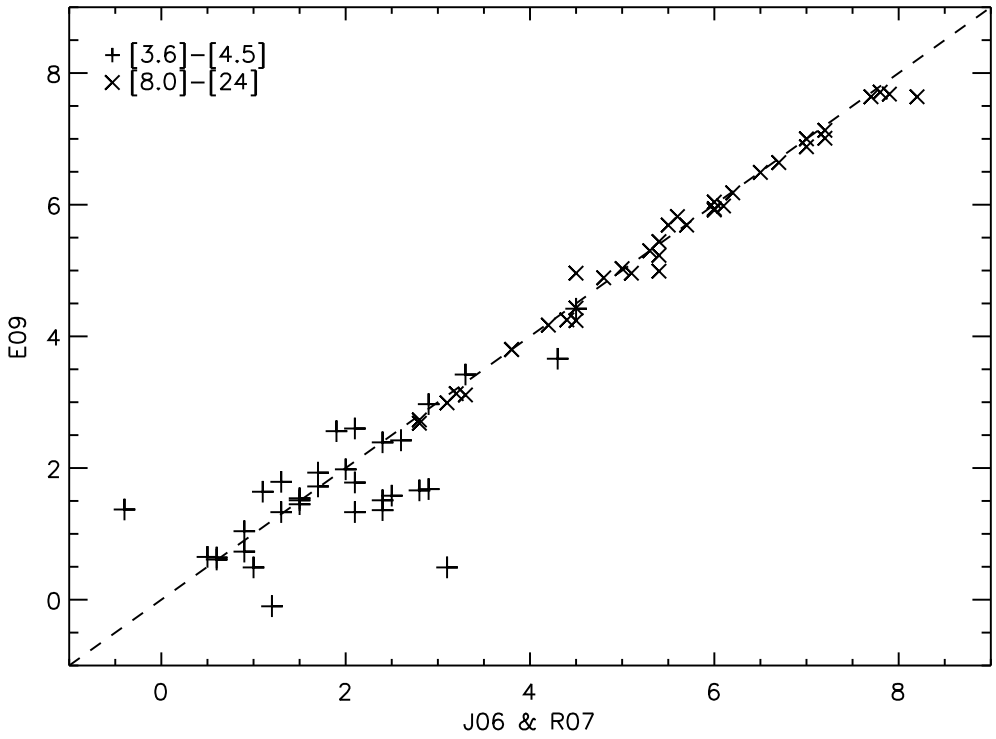

Figure A.1: Colours of the Perseus data from Jørgensen et al. (2006) and Rebull et al. (2007) against the colours from the Evans et al. (2009) updated data. To aid the eye, a one-to-one line has been drawn.

Table A.2: Deeply Embedded YSOs from Jørgensen et al. (2007)

Designation	RA (J2000.0)	Dec (J2000.0)	[3.6]-[4.5]	[8.0]-[24]
L1448-IRS 2[a]*	03 25 22.36	+30 45 13.6	2.9	6.5
L1448-N(A)[a]*	03 25 36.48	+30 45 23.2	2.8	6.0
L1448-C(N)[a]*	03 25 38.87	+30 44 06.0	1.7	7.1
IRAS 03235+3004[a]*	03 26 37.46	+30 15 28.2	2.4	6.2
L1455-FIR 2[a]	03 27 38.27	+30 13 58.5	0.6	3.8
L1455-IRS 1[a]*	03 27 39.11	+30 13 02.8	3.3	7.0
L1455-IRS 4[a]*	03 27 43.25	+30 12 28.9	2.1	6.1
03278+30121[b]	03 27 47.69	+30 12 04.4	0.9	2.8
03285+31111[b]	03 28 32.55	+31 11 04.8	-0.4	5.4
03286+31071[b]	03 28 34.53	+31 07 05.5	1.5	3.1
IRAS 03255+3103[a]	03 28 37.11	+31 13 28.3	2.8	...
HH 340[c]	03 28 39.11	+31 06 01.6	1.3	6.0
03287+31179[b]	03 28 40.62	+31 17 56.5	...	4.4
IRAS 03256+3055[a]	03 28 45.31	+31 05 41.9	2.4	7.2
NGC 1333-IRAS 2A[a]	03 28 55.59	+31 14 37.5	...	...
NGC 1333-IRAS 2B[a]	03 28 57.36	+31 14 15.9	2.1	5.0
03290+31218[b]	03 28 59.55	+31 21 46.7	0.6	2.8
03290+31120[b]	03 29 00.61	+31 12 00.4	...	...
NGC 1333-SVS12[c]	03 29 01.66	+31 20 28.5	...	...
NGC 1333-SVS13[a]	03 29 03.30	+31 15 55.5	...	...
HH 7-11 MMS6[a]	03 29 04.09	+31 14 46.6	1.5	6.7
NGC 1333-IRAS 4A[a]	03 29 10.53	+31 13 30.7	...	...
03292+31183[b]	03 29 10.72	+31 18 20.5	...	7.2
03292+31185[b]	03 29 11.29	+31 18 31.3	...	8.2
NGC 1333-IRAS 4B[a]	03 29 12.07	+31 13 01.8	4.3	5.4
NGC 1333-IRAS 4C[a]	03 29 13.62	+31 13 57.9	3.1	...
Per 4[c]	03 29 17.21	+31 27 46.2	1.1	7.8
HH 335[c]	03 29 18.25	+31 23 19.9	1.7	4.5
03293+31234[b]	03 29 18.73	+31 23 25.4	0.5	3.2
IRAS 03262+3123[a]	03 29 23.50	+31 33 29.4	...	7.0
IRAS 03267+3128[a]	03 29 51.89	+31 39 05.6	...	7.9
IRAS 03282+3035[a]*	03 31 21.01	+30 45 30.0	1.9	5.6
IRAS 03292+3039[a]*	03 32 18.03	+30 49 46.9	1.0	4.8
Per 9B[c]	03 33 13.81	+31 20 05.2	2.1	5.1
B1-SMM3[a]	03 33 14.41	+31 07 10.8	2.4	6.0
B1-d[a]	03 33 16.49	+31 06 52.3	...	...
B1-a[a]*	03 33 16.67	+31 07 55.1	2.9	5.3
B1-c[a]*	03 33 17.87	+31 09 31.8	4.5	4.5
B1-b[a]*	03 33 20.34	+31 07 21.4	2.0	4.2

HH 789[c]	03 33 27.31	+31 07 10.2	2.5	7.7
03438+32034[b]	03 43 50.99	+32 03 24.7	1.3	5.5
03439+32031[b]	03 43 51.03	+32 03 08.0	1.2	5.7
IC 348-MMS[a]	03 43 56.91	+32 03 04.2	...	...
HH 211-FIR[c]	03 43 57.32	+32 00 47.6	...	...
HH 211-a[d]	03 43 57.64	+32 00 44.8	...	...
HH 211-b[d]	03 43 59.41	+32 00 35.5	2.6	4.5
03440+32021[b]	03 44 02.40	+32 02 04.7	1.5	5.4
IRAS 03415+3152[a]	03 44 43.32	+32 01 31.6	0.9	3.8
B5-IRS 1[a]	03 47 41.61	+32 51 43.9	1.1	3.3

* *Sources originally identified by Jørgensen et al. (2006) based on IRAC+MIPS colours.*

[a] *Designation from SIMBAD database or commonly used identifier.*

[b] *No designation from SIMBAD, name from RA and DEC.*

[c] *Commonly associated with object.*

[d] *Both sources are commonly associated with HH 211.*

Table A.3: 2MASS (Skrutskie et al. 2006; Evans et al. 2009) data

Designation	flag	J (mJy)	H (mJy)	K_s (mJy)
L1448-IRS 2	0 0 0			
L1448-N(A)	0 0 0			
L1448-CN	0 0 0			
IRAS 03235+3004	1 1 1	0.18 ± 0.00	0.5 ± 0.00	1.19 ± 0.08
L1455-FIR 2	1 1 1	0.23 ± 0.05	7.99 ± 0.32	36.40 ± 0.84
L1455-IRS 1	0 0 0			
L1455-IRS 4	0 0 0			
03278+30121	1 1 1	58.60 ± 1.40	170.00 ± 5.02	267.00 ± 5.65
03285+31111	1 1 1	0.17 ± 0.00	0.69 ± 0.00	1.07 ± 0.11
03286+31071	0 0 0			
IRAS 03255+3103	1 1 1	0.58 ± 0.00	1.18 ± 0.14	10.1 ± 0.00
HH 340	0 0 0			
03287+31179	0 0 0			
IRAS 03256+3055	1 1 1	0.06 ± 0.00	0.46 ± 0.00	0.72 ± 0.1
NGC 1333-IRAS 2A	0 0 0			
NGC 1333-IRAS 2B	0 0 0			
03290+31218	1 1 1	14.40 ± 0.3	32.10 ± 0.71	50.5 ± 0.98
03290+31120	0 0 0			
NGC 1333-SVS 12	1 1 1	0.8 ± 0.00	2.86 ± 0.2	29.60 ± 1.01
NGC 1333-SVS 13	1 1 1	34.20 ± 0.76	141.00 ± 4.02	360.00 ± 6.63
HH 7-11 MMS6	0 0 0			
NGC 1333-IRAS 4A	0 0 0			
03292+31183	0 0 0			
03292+31185	0 0 0			
NGC 1333-IRAS 4B	0 0 0			
NGC 1333-IRAS 4C	0 0 0			
Per 4	0 0 0			
HH 335	0 0 0			
03293+31234	1 1 1	42.10 ± 0.93	54.90 ± 1.52	49.20 ± 1.00
IRAS 03262+3123	0 0 0			
IRAS 03267+3128	0 0 0			
IRAS 03282+3035	0 0 0			
IRAS 03292+3039	0 0 0			
Per 9B	0 0 0			
B1-SMM 3	0 0 0			
B1-d	0 0 0			
B1-a	1 1 1	0.09 ± 0.00	0.38 ± 0.00	1.38 ± 0.08
B1-c	0 0 0			
B1-b	0 0 0			

HH 789	0 0 0			
03438+32034	0 0 0			
03439+32031	0 0 0			
IC 348-MMS	0 0 0			
HH 211-FIR	0 0 0			
HH 211-a	1 1 1	0.16 ± 0.00	0.28 ± 0.00	0.51 ± 0.08
HH 211-b	1 1 1	0.31 ± 0.00	0.44 ± 0.08	2.64 ± 0.16
03440+32021	0 0 0			
IRAS 03415+3152	1 1 1	0.4 ± 0.00	3.64 ± 0.21	34.40 ± 0.73
B5-IRS 1	1 1 1	0.18 ± 0.04	2.46 ± 0.09	21.80 ± 0.4

Table A.4: IRAC (Jørgensen et al. 2006; Evans et al. 2009) data

Designation	flag	3.6 μm (mJy)	4.5 μm (mJy)	5.8 μm (mJy)	8.0 μm (mJy)
L1448-IRS 2	1 3 1 1	0.33 ± 0.04	3.28 ± 0.29	5.19 ± 0.36	10.9 ± 0.57
L1448-N(A)	0 3 1 1	0.71 ± 0.14	11.1 ± 0.74	44.5 ± 2.22	136 ± 7.1
L1448-C(N)	1 3 1 0	3.05 ± 0.23	11.5 ± 1.18	16 ± 1.18	20.4 ± 1.6
IRAS 03235+3004	1 3 1 1	3.62 ± 0.23	9.27 ± 0.46	11.1 ± 0.54	12 ± 0.56
L1455-FIR 2	1 3 1 1	62.5 ± 3.14	72 ± 3.65	79.1 ± 3.77	93.1 ± 4.63
L1455-IRS 1	1 3 1 1	0.58 ± 0.04	8.68 ± 0.69	20.4 ± 1.05	24.4 ± 1.17
L1455-IRS 4	1 3 1 1	0.77 ± 0.06	5.39 ± 0.37	12.2 ± 0.64	27.5 ± 1.32
03278+30121	1 3 1 1	408 ± 24.3	510 ± 31.2	786 ± 39	1270 ± 64.5
03285+31111	1 3 1 1	1.01 ± 0.07	2.28 ± 0.13	2.57 ± 0.13	4.01 ± 0.2
03286+31071	1 3 1 1	4.59 ± 0.22	11.8 ± 0.6	24.2 ± 1.13	34.4 ± 1.67
IRAS 03255+3103	1 3 1 1	30.1 ± 1.75	89.2 ± 5.47	267 ± 13.3	722 ± 41.3
HH 340	1 3 1 1	0.12 ± 0.01	0.27 ± 0.02	0.43 ± 0.03	0.94 ± 0.05
03287+31179	0 3 1 1	0.03 ± 0.01	0.18 ± 0.01	0.49 ± 0.04	0.93 ± 0.06
IRAS 03256+3055	1 3 1 1	1.22 ± 0.06	2.73 ± 0.13	2.67 ± 0.13	2.69 ± 0.13
NGC 1333-IRAS 2A	1 3 1 1	1.05 ± 0.07	12.6 ± 0.86	22.7 ± 1.42	30.6 ± 2.11
NGC 1333-IRAS 2B	1 3 1 1	31.6 ± 1.54	104 ± 5.82	262 ± 12.4	375 ± 22.8
03290+31218	1 3 1 1	71.7 ± 4.21	80.8 ± 4.01	68.8 ± 3.38	72.5 ± 3.61
03290+31120	0 3 1 1	0.01 ± 0.01	0.09 ± 0.01	0.11 ± 0.03	0.1 ± 0.04
NGC 1333-SVS 12	1 3 0 1	544 ± 37.1	1090 ± 77.2	1690 ± 211	3060 ± 189
NGC 1333-SVS 13	1 3 0 1	904 ± 57.2	359 ± 68.7	2750 ± 331	5690 ± 326
HH 7-11 MMS6	1 3 1 1	0.44 ± 0.03	1.08 ± 0.09	1.27 ± 0.08	1.43 ± 0.09
NGC 1333-IRAS 4A	0 3 1 0		0.08 ± 0.01	0.13 ± 0.03	.06
03292+31183	1 3 1 1	1.84 ± 0.15	6.69 ± 0.65	10.3 ± 0.83	10.9 ± 0.78
03292+31185	1 3 1 1	0.72 ± 0.07	3.94 ± 0.26	5 ± 0.33	4.13 ± 0.27
NGC 1333-IRAS 4B	1 3 1 1	0.68 ± 0.04	12.7 ± 0.68	4.86 ± 0.25	3.43 ± 0.21
NGC 1333-IRAS 4C	0 0 1 0	0.03 ± 0.01	0.03 ± 0.06	0.24 ± 0.04	0.25 ± 0.09
Per 4	1 3 1 1	0.42 ± 0.03	1.22 ± 0.1	1.24 ± 0.08	0.82 ± 0.1
HH 335	1 3 1 1	0.92 ± 0.05	2.85 ± 0.14	6.25 ± 0.3	10.7 ± 0.54
03293+31234	1 3 1 1	36 ± 2.16	41.9 ± 2.23	53.3 ± 2.53	92.9 ± 4.94
IRAS 03262+3123	1 3 1 1	0.76 ± 0.07	2.26 ± 0.13	2.47 ± 0.2	3.03 ± 0.15
IRAS 03267+3128	0 3 1 1	0 ± 0.01	0.02 ± 0	0.1 ± 0.03	0.37 ± 0.03
IRAS 03282+3035	1 3 1 1	0.13 ± 0.01	0.85 ± 0.05	0.83 ± 0.06	0.62 ± 0.05
IRAS 03292+3039	0 0 0 1	0.39 ± 0.08	0.42 ± 0.14	0.25 ± 0.14	1.29 ± 0.09
Per 9B	1 3 1 1	0.6 ± 0.03	1.3 ± 0.07	2.47 ± 0.13	5.45 ± 0.27
B1-SMM 3	1 3 1 1	0.16 ± 0.01	0.94 ± 0.05	2.05 ± 0.11	4.21 ± 0.2
B1-d	0 0 1 0	0.03 ± 0.01	0.26 ± 0.04	0.44 ± 0.05	0.17 ± 0.07
B1-a	1 3 1 1	16.4 ± 0.91	49.3 ± 2.5	84.5 ± 4	115 ± 5.43
B1-c	1 3 1 1	0.17 ± 0.01	6.4 ± 0.33	36.4 ± 1.79	102 ± 5.14
B1-b	1 3 1 1	4.19 ± 0.21	16.6 ± 0.8	25.9 ± 1.23	32.4 ± 1.54

HH 789	1 3 1 1	2.43 ± 0.12	6.68 ± 0.32	7.93 ± 0.38	12.4 ± 0.59
03438+32034	1 3 1 1	0.34 ± 0.02	1.14 ± 0.09	1.52 ± 0.14	2.58 ± 0.15
03439+32031	1 3 1 1	6.81 ± 0.47	3.99 ± 0.6	12.8 ± 0.67	2.15 ± 0.15
IC 348-MMS	0 0 1 0	0.05 ± 0.01	0.2 ± 0.06	0.52 ± 0.05	0.6 ± 0.12
HH 211-FIR	0 0 1 0	0.2 ± 0.04	0.41 ± 0.1	0.68 ± 0.08	0.46 ± 0.16
HH 211-a	0 0 1 1	0.25 ± 0.04	0.29 ± 0.08	0.39 ± 0.05	0.75 ± 0.11
HH 211-b	1 3 1 1	2.18 ± 0.12	12.9 ± 1.03	5.31 ± 0.28	4.04 ± 0.27
03440+32021	1 3 1 1	0.73 ± 0.04	1.93 ± 0.11	3.82 ± 0.19	6.41 ± 0.32
IRAS 03415+3152	1 3 1 1	181 ± 9.19	302 ± 17.6	378 ± 18.1	555 ± 27.7
B5-IRS 1	0 3 1 1	387 ± 27.6	809 ± 44.4	1380 ± 69	1740 ± 102

Table A.5: MIPS (Rebull et al. 2007; Evans et al. 2009) & SCUBA (Kirk et al. 2006; Ridge et al. 2006) data

Designation	flag	24 μm (mJy)	70 μm (mJy)	850 μm (mJy)
L1448-IRS 2	1 1 3	479 ± 44.5	12900 ± 1210	3880
L1448-N(A)	1 1 3	3940 ± 371	23700 ± 2220	17800
L1448-C(N)	1 1 3	1790 ± 167	31000 ± 2900	4280
IRAS 03235+3004	1 1 3	396 ± 36.7	4300 ± 406	340
L1455-FIR 2	1 1 3	343 ± 31.9	1120 ± 114	530
L1455-IRS 1	1 1 3	1710 ± 162	21400 ± 2060	1590
L1455-IRS 4	1 1 3	755 ± 70.5	7390 ± 688	2000
03278+30121	1 1 3	1670 ± 156	1810 ± 175	1910
03285+31111	1 1 3	55.3 ± 5.13	179 ± 19.5	1940
03286+31071	1 1 3	60.4 ± 5.59	159 ± 17.4	1650
IRAS 03255+3103	0 1 3	6860 ± 1150	53800 ± 5020	1940
HH 340	1 1 3	24.4 ± 2.27	94 ± 11.1	1650
03287+31179	1 0 3	5.23 ± 0.54		2270
IRAS 03256+3055	1 1 3	213 ± 19.9	1520 ± 150	1650
NGC 1333-IRAS 2A	0 1 3	-41.4 ± 116	139000 ± 12900	8030
NGC 1333-IRAS 2B	1 1 3	4300 ± 404	30000 ± 2780	8030
03290+31218	1 0 3	99.5 ± 9.28		4800
03290+31120	1 1 3	15.4 ± 1.44	1320 ± 127	250
NGC 1333-SVS 12	0 1 3	-275 ± 69	23400 ± 2210	10140
NGC 1333-SVS 13	0 1 3	-1130 ± 434	125000 ± 11600	12150
HH 7-11 MMS6	1 0 3	71.8 ± 6.68		4010
NGC 1333-IRAS 4A	1 1 3	32.2 ± 3.03	33400 ± 3130	17020
03292+31183	1 1 3	771 ± 72.2	20600 ± 1930	6830
03292+31185	1 0 3	522 ± 48.8		6830
NGC 1333-IRAS 4B	1 0 3	37.7 ± 3.57		12850
NGC 1333-IRAS 4C	1 1 3	28.4 ± 2.64	3910 ± 370	17020
Per 4	1 1 3	111 ± 10.3	1950 ± 218	930
HH 335	1 0 3	59.3 ± 6.06		1840
03293+31234	1 0 3	184 ± 17.2		1840
IRAS 03262+3123	1 1 3	191 ± 17.7	1150 ± 110	780
IRAS 03267+3128	1 1 3	48.9 ± 4.53	1990 ± 191	820
IRAS 03282+3035	1 1 3	14.7 ± 1.37	3880 ± 366	1820
IRAS 03292+3039	1 1 3	13 ± 1.22	1720 ± 161	8530
Per 9B	1 1 3	58.5 ± 5.44	55.5 ± 18.1	780
B1-SMM 3	1 1 3	111 ± 10.4	809 ± 83.5	9920
B1-d	1 1 3	19.5 ± 1.84	1820 ± 180	9920
B1-a	1 1 3	1690 ± 160	6450 ± 609	9920
B1-c	1 1 3	670 ± 63	11700 ± 1190	8780
B1-b	1 1 3	168 ± 15.7	350 ± 40	11650

HH 789	1 1 3	1570 ± 147	5410 ± 510	11650
03438+32034	1 0 3	54.1 ± 5.03		2920
03439+32031	1 1 3	45.4 ± 4.25	1960 ± 195	2920
IC 348-MMS	1 1 3	10.8 ± 1.04	3280 ± 314	4540
HH 211-FIR	1 0 3	2.2 ± 0.29		6270
HH 211-a	1 0 3	1.59 ± 0.25		6270
HH 211-b	1 1 3	43.2 ± 4.03	367 ± 45.9	6270
03440+32021	1 1 3	107 ± 10.4	847 ± 90.6	1880
IRAS 03415+3152	1 0 3	2040 ± 193		1510
B5-IRS 1	1 1 3	3400 ± 317	10800 ± 1070	1210

Table A.6: Histogram Range

Symbol	Unit	Model Range	Binned Range	log? lin?	Width
L_{tot}	$L_\odot$	0.016–7.44×10^5	0.09–30	logarithmic	0.084 (1.21×)
M_*	$M_\odot$	0.1–50	0.1–5	logarithmic	0.057 (1.14×)
M_{disk}	$M_\odot$	1.09×10^{-10}–3.27	5×10^{-6}–5×10^{-2}	logarithmic	0.133 (1.36×)
$\dot{M}_{env}$	$M_\odot$ yr^{-1}	3.58×10^{-10}–9.97×10^{-3}	10^{-6}–2×10^{-4}	logarithmic	0.077 (1.19×)
$\dot{M}_{disk}$	$M_\odot$ yr^{-1}	1.61×10^{-17}–2.83×10^{-3}	10^{-12}–2×10^{-6}	logarithmic	0.210 (1.62×)
R_{disk}^{min}	R_{sub}	1.0–9.08×10^3	1.0–10^3	logarithmic	0.100 (1.26×)
R_{disk}^{max}	AU	1.17–9780	1.0–2000	logarithmic	0.110 (1.29×)
θ_{cav}	°	1–60	1–60	linear	1
θ	$\cos(\theta)$	0–1	0–1	linear	0.1
A_V	mag	0–10	0–10	linear	1
$\frac{M_*}{M_{core}}$		3×10^{-3}–3		logarithmic	0.100 (1.26×)
$\frac{L_{acc}}{L_{tot}}$		10^{-5}–1		logarithmic	0.167 (1.47×)

Bibliography

Adams, F. C., Lada, C. J., and Shu, F. H.: 1987, *ApJ* **312**, 788

Adams, F. C. and Shu, F. H.: 1986, *ApJ* **308**, 836

Allen, L. E., Calvet, N., D'Alessio, P., Merin, B., Hartmann, L., Megeath, S. T., Gutermuth, R. A., Muzerolle, J., Pipher, J. L., Myers, P. C., and Fazio, G. G.: 2004, *ApJS* **154**, 363

Alves, J. F., Lada, C. J., and Lada, E. A.: 2001, *Nature* **409**, 159

Andre, P., Ward-Thompson, D., and Barsony, M.: 1993, *ApJ* **406**, 122

Andrews, S. M. and Williams, J. P.: 2005, *ApJ* **631**, 1134

Andrews, S. M. and Williams, J. P.: 2007, *ApJ* **671**, 1800

Arce, H. G., Borkin, M. A., Goodman, A. A., Pineda, J. E., and Halle, M. W.: 2010, *ApJ* **715**, 1170

Artymowicz, P. and Lubow, S. H.: 1994, *ApJ* **421**, 651

Aspin, C. and Sandell, G.: 2001, *MNRAS* **328**, 751

Bally, J., Reipurth, B., and Davis, C. J.: 2007, *Protostars and Planets V* pp 215–230

Bally, J., Walawender, J., Reipurth, B., and Megeath, S. T.: 2009, *AJ* **137**, 3843

Bernasconi, P. A. and Maeder, A.: 1996, *A&A* **307**, 829

Bjorkman, J. E.: 1997, in J. P. De Greve, R. Blomme, & H. Hensberge (ed.), *Stellar Atmospheres: Theory and Observations*, Vol. 497 of *Lecture Notes in Physics, Berlin Springer Verlag*, pp 239–+

Bontemps, S., Andre, P., Terebey, S., and Cabrit, S.: 1996, *A&A* **311**, 858

Calvet, N. and Gullbring, E.: 1998, *ApJ* **509**, 802

Carroll, B. W. and Ostlie, D. A.: 2006, *An introduction to modern astrophysics and cosmology*

Chen, H., Myers, P. C., Ladd, E. F., and Wood, D. O. S.: 1995, *ApJ* **445**, 377

Curtis, E. I., Richer, J. S., Swift, J. J., and Williams, J. P.: 2010, *ArXiv e-prints*

Davis, C. J., Chrysostomou, A., Hatchell, J., Wouterloot, J. G. A., Buckle, J. V., Nutter, D., Fich, M., Brunt, C., Butner, H., Cavanagh, B., Curtis, E. I., Duarte-Cabral, A., di Francesco, J., Etxaluze, M., Friberg, P., Friesen, R., Fuller, G. A., Graves, S., Greaves, J. S., Hogerheijde, M. R., Johnstone, D., Matthews, B., Matthews, H., Rawlings, J. M. C., Richer, J. S., Roberts, J., Sadavoy, S., Simpson, R. J., Tothill, N., Tsamis, Y., Viti, S., Ward-Thompson, D., White, G. J., and Yates, J.: 2010, *MNRAS* **405**, 759

Di Francesco, J., Evans, II, N. J., Caselli, P., Myers, P. C., Shirley, Y., Aikawa, Y., and Tafalla, M.: 2007, *Protostars and Planets V* pp 17–32

Dopita, M. A., Evans, I., and Schwartz, R. D.: 1982, *ApJ* **263**, L73

Dullemond, C. P., Dominik, C., and Natta, A.: 2001, *ApJ* **560**, 957

Dunham, M. M., Crapsi, A., Evans, II, N. J., Bourke, T. L., Huard, T. L., Myers, P. C., and Kauffmann, J.: 2008, *ApJS* **179**, 249

Dunham, M. M., Evans, N. J., Terebey, S., Dullemond, C. P., and Young, C. H.: 2010, *ApJ* **710**, 470

Durisen, R. H., Boss, A. P., Mayer, L., Nelson, A. F., Quinn, T., and Rice, W. K. M.: 2007, *Protostars and Planets V* pp 607–622

Elia, D., Schisano, E., Molinari, S., Robitaille, T., Anglés-Alcázar, D., Bally, J., Battersby, C., Benedettini, M., Billot, N., Calzoletti, L., di Giorgio, A. M., Faustini, F., Li, J. Z., Martin, P., Morgan, L., Motte, F., Mottram, J. C., Natoli, P., Olmi, L., Paladini, R., Piacentini, F., Pestalozzi, M., Pezzuto, S., Polychroni, D., Smith, M. D., Strafella, F., Stringfellow, G. S., Testi, L., Thompson, M. A., Traficante, A., and Veneziani, M.: 2010, *A&A* **518**, L97+

Enoch, M. L., Evans, N. J., Sargent, A. I., and Glenn, J.: 2009, *ApJ* **692**, 973

Evans, N. J., Dunham, M. M., Jørgensen, J. K., Enoch, M. L., Merín, B., van Dishoeck, E. F., Alcalá, J. M., Myers, P. C., Stapelfeldt, K. R., Huard, T. L., Allen, L. E., Harvey, P. M., van Kempen, T., Blake, G. A., Koerner, D. W., Mundy, L. G., Padgett, D. L., and Sargent, A. I.: 2009, *ApJS* **181**, 321

Evans, II, N. J., Allen, L. E., Blake, G. A., Boogert, A. C. A., Bourke, T., Harvey, P. M., Kessler, J. E., Koerner, D. W., Lee, C. W., Mundy, L. G., Myers, P. C., Padgett, D. L., Pontoppidan, K., Sargent, A. I., Stapelfeldt, K. R., van Dishoeck, E. F., Young, C. H., and Young, K. E.: 2003, *PASP* **115**, 965

Flaccomio, E., Micela, G., Favata, F., and Alencar, S. P. H.: 2010, *A&A* **516**, L8+

Forbrich, J., Tappe, A., Robitaille, T., Muench, A. A., Teixeira, P. S., Lada, E. A., Stolte, A., and Lada, C. J.: 2010, *ApJ* **716**, 1453

Friesen, R. K., Di Francesco, J., Shimajiri, Y., and Takakuwa, S.: 2010, *ApJ* **708**, 1002

Friesen, R. K., Di Francesco, J., Shirley, Y. L., and Myers, P. C.: 2009, *ApJ* **697**, 1457

Greissl, J., Meyer, M. R., Wilking, B. A., Fanetti, T., Schneider, G., Greene, T. P., and Young, E.: 2007, *AJ* **133**, 1321

Guilloteau, S., Dutrey, A., and Simon, M.: 1999, *A&A* **348**, 570

Gutermuth, R. A., Megeath, S. T., Muzerolle, J., Allen, L. E., Pipher, J. L., Myers, P. C., and Fazio, G. G.: 2004, *ApJS* **154**, 374

Hartmann, L.: 1998, *Accretion Processes in Star Formation*, Cambridge University Press

Hatchell, J. and Fuller, G. A.: 2008, *A&A* **482**, 855

Hatchell, J., Fuller, G. A., Richer, J. S., Harries, T. J., and Ladd, E. F.: 2007, *A&A* **468**, 1009

Hatchell, J., Richer, J. S., Fuller, G. A., Qualtrough, C. J., Ladd, E. F., and Chandler, C. J.: 2005, *A&A* **440**, 151

Herbig, G. H. and Jones, B. F.: 1983, *AJ* **88**, 1040

Hildebrand, R. H.: 1983, *QJRAS* **24**, 267

Johnstone, D., Fich, M., Mitchell, G. F., and Moriarty-Schieven, G.: 2001, *ApJ* **559**, 307

Johnstone, D., Matthews, H., and Mitchell, G. F.: 2006, *ApJ* **639**, 259

Johnstone, D., Wilson, C. D., Moriarty-Schieven, G., Joncas, G., Smith, G., Gregersen, E., and Fich, M.: 2000, *ApJ* **545**, 327

Jørgensen, J. K., Harvey, P. M., Evans, II, N. J., Huard, T. L., Allen, L. E., Porras, A., Blake, G. A., Bourke, T. L., Chapman, N., Cieza, L., Koerner, D. W., Lai, S.-P., Mundy, L. G., Myers, P. C., Padgett, D. L., Rebull, L., Sargent, A. I., Spiesman, W., Stapelfeldt, K. R., van Dishoeck, E. F., Wahhaj, Z., and Young, K. E.: 2006, *ApJ* **645**, 1246

Jørgensen, J. K., Johnstone, D., Kirk, H., and Myers, P. C.: 2007, *ApJ* **656**, 293

Jørgensen, J. K., Johnstone, D., Kirk, H., Myers, P. C., Allen, L. E., and Shirley, Y. L.: 2008, *ApJ* **683**, 822

Jørgensen, J. K., Lahuis, F., Schöier, F. L., van Dishoeck, E. F., Blake, G. A., Boogert, A. C. A., Dullemond, C. P., Evans, II, N. J., Kessler- Silacci, J. E., and Pontoppidan, K. M.: 2005, *ApJ* **631**, L77

Jørgensen, J. K., van Dishoeck, E. F., Visser, R., Bourke, T. L., Wilner, D. J., Lommen, D., Hogerheijde, M. R., and Myers, P. C.: 2009, *A&A* **507**, 861

Kenyon, S. J. and Hartmann, L.: 1995, *ApJS* **101**, 117

Kenyon, S. J., Hartmann, L. W., Strom, K. M., and Strom, S. E.: 1990, *AJ* **99**, 869

Kirk, H., Johnstone, D., and Basu, S.: 2009, *ApJ* **699**, 1433

Kirk, H., Johnstone, D., and Di Francesco, J.: 2006, *ApJ* **646**, 1009

Kirk, H., Johnstone, D., and Tafalla, M.: 2007, *ApJ* **668**, 1042

Kroupa, P.: 2001, *MNRAS* **322**, 231

Krumholz, M. R., McKee, C. F., and Tumlinson, J.: 2008, *ApJ* **689**, 865

Lada, C. J.: 1987, in M. Peimbert & J. Jugaku (ed.), *Star Forming Regions*, Vol. 115 of *IAU Symposium*, pp 1–17

Lada, C. J. and Lada, E. A.: 2003, *ARA&A* **41**, 57

Lada, C. J. and Wilking, B. A.: 1984, *ApJ* **287**, 610

Larson, R. B.: 1981, *MNRAS* **194**, 809

Lombardi, M. and Alves, J.: 2001, *A&A* **377**, 1023

Luhman, K. L., Whitney, B. A., Meade, M. R., Babler, B. L., Indebetouw, R., Bracker, S., and Churchwell, E. B.: 2006, *ApJ* **647**, 1180

Lynden-Bell, D. and Pringle, J. E.: 1974, *MNRAS* **168**, 603

Mayama, S., Tamura, M., Hanawa, T., Matsumoto, T., Ishii, M., Pyo, T., Suto, H., Naoi, T., Kudo, T., Hashimoto, J., Nishiyama, S., Kuzuhara, M., and Hayashi, M.: 2010, *Science* **327**, 306

McCabe, C., Duchêne, G., and Ghez, A. M.: 2003, *ApJ* **588**, L113

Megeath, S. T., Allen, L. E., Gutermuth, R. A., Pipher, J. L., Myers, P. C., Calvet, N., Hartmann, L., Muzerolle, J., and Fazio, G. G.: 2004, *ApJS* **154**, 367

Millan-Gabet, R., Malbet, F., Akeson, R., Leinert, C., Monnier, J., and Waters, R.: 2007, *Protostars and Planets V* pp 539–554

Miller, G. E. and Scalo, J. M.: 1979, *ApJS* **41**, 513

Moriarty-Schieven, G. H., Wannier, P. G., Mangum, J. G., Tamura, M., and Olmsted, V. K.: 1995, *ApJ* **455**, 190

Mouschovias, T. C. and Spitzer, Jr., L.: 1976, *ApJ* **210**, 326

Muzerolle, J., Megeath, S. T., Gutermuth, R. A., Allen, L. E., Pipher, J. L., Hartmann, L., Gordon, K. D., Padgett, D. L., Noriega-Crespo, A., Myers, P. C., Fazio, G. G., Rieke, G. H., Young, E. T., Morrison, J. E., Hines, D. C., Su, K. Y. L., Engelbracht, C. W., and Misselt, K. A.: 2004, *ApJS* **154**, 379

Najita, J.: 2004, in D. Johnstone, F. C. Adams, D. N. C. Lin, D. A. Neufeeld, & E. C. Ostriker (ed.), *Star Formation in the Interstellar Medium: In Honor of David Hollenbach*, Vol. 323 of *Astronomical Society of the Pacific Conference Series*, pp 271–+

Najita, J. R., Tiede, G. P., and Carr, J. S.: 2000, *ApJ* **541**, 977

Nutter, D., Kirk, J. M., Stamatellos, D., and Ward-Thompson, D.: 2008, *MNRAS* **384**, 755

Ossenkopf, V. and Henning, T.: 1994, *A&A* **291**, 943

Padgett, D. L., Rebull, L. M., Stapelfeldt, K. R., Chapman, N. L., Lai, S., Mundy, L. G., Evans, II, N. J., Brooke, T. Y., Cieza, L. A., Spiesman, W. J., Noriega-Crespo, A., McCabe, C., Allen, L. E., Blake, G. A., Harvey, P. M., Huard, T. L., Jørgensen, J. K., Koerner, D. W., Myers, P. C., Sargent, A. I., Teuben, P., van Dishoeck, E. F., Wahhaj, Z., and Young, K. E.: 2008, *ApJ* **672**, 1013

Peneva, S. P., Semkov, E. H., Munari, U., and Birkle, K.: 2010, *A&A* **515**, A24+

Pineda, J. E., Goodman, A. A., Arce, H. G., Caselli, P., Foster, J. B., Myers, P. C., and Rosolowsky, E. W.: 2010, *ApJ* **712**, L116

Pon, A., Plume, R., Friesen, R. K., Di Francesco, J., Matthews, B., and Bergin, E. A.: 2009, *ApJ* **698**, 1914

Pringle, J. E.: 1981, *ARA&A* **19**, 137

Pudritz, R. E., Ouyed, R., Fendt, C., and Brandenburg, A.: 2007, *Protostars and Planets V* pp 277–294

Ray, T., Dougados, C., Bacciotti, F., Eislöffel, J., and Chrysostomou, A.: 2007, *Protostars and Planets V* pp 231–244

Reach, W. T., Megeath, S. T., Cohen, M., Hora, J., Carey, S., Surace, J., Willner, S. P., Barmby, P., Wilson, G., Glaccum, W., Lowrance, P., Marengo, M., and Fazio, G. G.: 2005, *PASP* **117**, 978

Rebull, L. M., Stapelfeldt, K. R., Evans, II, N. J., Jørgensen, J. K., Harvey, P. M., Brooke, T. Y., Bourke, T. L., Padgett, D. L., Chapman, N. L., Lai, S.-P., Spiesman,

W. J., Noriega-Crespo, A., Merín, B., Huard, T., Allen, L. E., Blake, G. A., Jarrett, T., Koerner, D. W., Mundy, L. G., Myers, P. C., Sargent, A. I., van Dishoeck, E. F., Wahhaj, Z., and Young, K. E.: 2007, *ApJS* **171**, 447

Reipurth, B., Hartmann, L., Kenyon, S. J., Smette, A., and Bouchet, P.: 2002, *AJ* **124**, 2194

Riaz, B., Martín, E. L., Bouy, H., and Tata, R.: 2009, *ApJ* **700**, 1541

Ridge, N. A., Di Francesco, J., Kirk, H., Li, D., Goodman, A. A., Alves, J. F., Arce, H. G., Borkin, M. A., Caselli, P., Foster, J. B., Heyer, M. H., Johnstone, D., Kosslyn, D. A., Lombardi, M., Pineda, J. E., Schnee, S. L., and Tafalla, M.: 2006, *AJ* **131**, 2921

Rieke, G. H., Blaylock, M., Decin, L., Engelbracht, C., Ogle, P., Avrett, E., Carpenter, J., Cutri, R. M., Armus, L., Gordon, K., Gray, R. O., Hinz, J., Su, K., and Willmer, C. N. A.: 2008, *AJ* **135**, 2245

Robitaille, T. P., Whitney, B. A., Indebetouw, R., and Wood, K.: 2007, *ApJS* **169**, 328

Robitaille, T. P., Whitney, B. A., Indebetouw, R., Wood, K., and Denzmore, P.: 2006, *ApJS* **167**, 256

Rosolowsky, E. W., Pineda, J. E., Foster, J. B., Borkin, M. A., Kauffmann, J., Caselli, P., Myers, P. C., and Goodman, A. A.: 2008, *ApJS* **175**, 509

Sadavoy, S. I., Di Francesco, J., Bontemps, S., Megeath, S. T., Rebull, L. M., Allgaier, E., Carey, S., Gutermuth, R., Hora, J., Huard, T., McCabe, C., Muzerolle, J., Noriega-Crespo, A., Padgett, D., and Terebey, S.: 2010, *ApJ* **710**, 1247

Salpeter, E. E.: 1955, *ApJ* **121**, 161

Schnee, S., Enoch, M., Johnstone, D., Culverhouse, T., Leitch, E., Marrone, D. P., and Sargent, A.: 2010, *ApJ* **718**, 306

Sewiło, M., Indebetouw, R., Carlson, L. R., Whitney, B. A., Chen, C., Meixner, M., Robitaille, T., van Loon, J. T., Oliveira, J. M., Churchwell, E., Simon, J. D., Hony, S., Panuzzo, P., Sauvage, M., Roman-Duval, J., Gordon, K., Engelbracht, C., Misselt, K., Okumura, K., Beck, T., Hora, J., and Woods, P. M.: 2010, *A&A* **518**, L73+

Shakura, N. I. and Sunyaev, R. A.: 1973, *A&A* **24**, 337

Shang, H., Li, Z., and Hirano, N.: 2007, *Protostars and Planets V* pp 261–276

Shu, F., Najita, J., Ostriker, E., Wilkin, F., Ruden, S., and Lizano, S.: 1994, *ApJ* **429**, 781

Shu, F. H.: 1977, *ApJ* **214**, 488

Shu, F. H., Tremaine, S., Adams, F. C., and Ruden, S. P.: 1990, *ApJ* **358**, 495

Siess, L., Dufour, E., and Forestini, M.: 2000, *A&A* **358**, 593

Simpson, R. J., Nutter, D., and Ward-Thompson, D.: 2008, *MNRAS* **391**, 205

Skrutskie, M. F., Cutri, R. M., Stiening, R., Weinberg, M. D., Schneider, S., Carpenter, J. M., Beichman, C., Capps, R., Chester, T., Elias, J., Huchra, J., Liebert, J., Lonsdale, C., Monet, D. G., Price, S., Seitzer, P., Jarrett, T., Kirkpatrick, J. D., Gizis, J. E., Howard, E., Evans, T., Fowler, J., Fullmer, L., Hurt, R., Light, R., Kopan, E. L., Marsh, K. A., McCallon, H. L., Tam, R., Van Dyk, S., and Wheelock, S.: 2006, *AJ* **131**, 1163

Smith, N., Bally, J., and Walborn, N. R.: 2010, *MNRAS* **405**, 1153

Sun, K., Kramer, C., Ossenkopf, V., Bensch, F., Stutzki, J., and Miller, M.: 2006, *A&A* **451**, 539

Terebey, S., Shu, F. H., and Cassen, P.: 1984, *ApJ* **286**, 529

Ulrich, R. K.: 1976, *ApJ* **210**, 377

Ungerechts, H. and Thaddeus, P.: 1987, *ApJS* **63**, 645

Černis, K.: 1990, *Ap&SS* **166**, 315

Černis, K. and Straižys, V.: 2003, *Baltic Astronomy* **12**, 301

Vorobyov, E. I. and Basu, S.: 2005a, *MNRAS* **360**, 675

Vorobyov, E. I. and Basu, S.: 2005b, *ApJ* **633**, L137

Vorobyov, E. I. and Basu, S.: 2006, *ApJ* **650**, 956

Ward-Thompson, D., Di Francesco, J., Hatchell, J., Hogerheijde, M. R., Nutter, D., Bastien, P., Basu, S., Bonnell, I., Bowey, J., Brunt, C., Buckle, J., Butner, H., Cavanagh, B., Chrysostomou, A., Curtis, E., Davis, C. J., Dent, W. R. F., van Dishoeck, E., Edmunds, M. G., Fich, M., Fiege, J., Fissel, L., Friberg, P., Friesen, R., Frieswijk, W., Fuller, G. A., Gosling, A., Graves, S., Greaves, J. S., Helmich, F., Hills, R. E., Holland, W. S., Houde, M., Jayawardhana, R., Johnstone, D., Joncas, G., Kirk, H., Kirk, J. M., Knee, L. B. G., Matthews, B., Matthews, H., Matzner, C., Moriarty-Schieven, G. H., Naylor, D., Padman, R., Plume, R., Rawlings, J. M. C., Redman, R. O., Reid, M., Richer, J. S., Shipman, R., Simpson, R. J., Spaans, M., Stamatellos, D., Tsamis, Y. G., Viti, S., Weferling, B., White, G. J., Whitworth, A. P., Wouterloot, J., Yates, J., and Zhu, M.: 2007, *PASP* **119**, 855

White, R. J., Greene, T. P., Doppmann, G. W., Covey, K. R., and Hillenbrand, L. A.: 2007, *Protostars and Planets V* pp 117–132

Whitney, B. A., Indebetouw, R., Bjorkman, J. E., and Wood, K.: 2004, *ApJ* **617**, 1177

Whitney, B. A., Wood, K., Bjorkman, J. E., and Cohen, M.: 2003a, *ApJ* **598**, 1079

Whitney, B. A., Wood, K., Bjorkman, J. E., and Wolff, M. J.: 2003b, *ApJ* **591**, 1049

Williams, J. P., de Geus, E. J., and Blitz, L.: 1994, *ApJ* **428**, 693

Wyatt, M. C.: 2008, *ARA&A* **46**, 339

Zavagno, A., Anderson, L. D., Russeil, D., Morgan, L., Stringfellow, G. S., Deharveng, L., Rodón, J. A., Robitaille, T. P., Mottram, J. C., Schuller, F., Testi, L., Billot, N., Molinari, S., di Gorgio, A., Kirk, J. M., Brunt, C., Ward-Thompson, D., Traficante, A., Veneziani, M., Faustini, F., and Calzoletti, L.: 2010, *A&A* **518**, L101+

Zhou, S.: 1995, *ApJ* **442**, 685